CrossMark

A Close-in Puffy Neptune with Hidden Friends: The Enigma of TOI 620

Michael A. Reefe[1] , Rafael Luque[2] , Eric Gaidos[3] , Corey Beard[4] , Peter P. Plavchan[1] , Marion Cointepas[5,6] ,
Bryson L. Cale[7,8] , Enric Palle[9] , Hannu Parviainen[10,11] , Dax L. Feliz[12] , Jason Eastman[13] , Keivan Stassun[12] ,
Jonathan Gagné[14] , Jon M. Jenkins[15] , Patricia T. Boyd[16] , Richard C. Kidwell[17] , Scott McDermott[18] , Karen A. Collins[13] ,
William Fong[19] , Natalia Guerrero[19,20] , Jose-Manuel Almenara-Villa[5] , Jacob Bean[21] , Charles A. Beichman[22] ,
John Berberian[1,23] , Allyson Bieryla[13] , Xavier Bonfils[5] , François Bouchy[6] , Madison Brady[21] , Edward M. Bryant[24,25] ,
Luca Cacciapuoti[16,26] , Caleb I. Cañas[27,28,51] , David R. Ciardi[22] , Kevin I. Collins[1] , Ian J. M. Crossfield[29] ,
Courtney D. Dressing[30] , Philipp Eigmüller[31] , Mohammed El Mufti[1] , Emma Esparza-Borges[10,11] , Akihiko Fukui[32,33] ,
Peter Gao[34] , Claire Geneser[35] , Crystal L. Gnilka[15] , Erica Gonzales[36] , Arvind F. Gupta[27,28] , Sam Halverson[37] ,
Fred Hearty[38] , Steve B. Howell[15] , Jonathan Irwin[13] , Shubham Kanodia[38] , David Kasper[21] , Takanori Kodama[32] ,
Veselin Kostov[16] , David W. Latham[13] , Monika Lendl[6] , Andrea Lin[38] , John H. Livingston[39] , Jack Lubin[4] ,
Suvrath Mahadevan[38] , Rachel Matson[40] , Elisabeth Matthews[6] , Felipe Murgas[5,10,11] , Norio Narita[32,33,41] ,
Patrick Newman[1] , Joe Ninan[38] , Ares Osborn[24,25] , Samuel N. Quinn[13] , Paul Robertson[4] , Arpita Roy[17] ,
Joshua Schlieder[16] , Christian Schwab[42] , Andreas Seifahrt[21] , Gareth D. Smith[43] , Ahmad Sohani[35] ,
Guðmundur Stefánsson[44] , Daniel Stevens[38] , Julian Stürmer[45] , Angelle Tanner[35] , Ryan Terrien[46] , Johanna Teske[34] ,
David Vermilion[1,16] , Sharon X. Wang[47] , Justin Wittrock[1] , Jason T. Wright[27,28,48] , Mathias Zechmeister[49] , and
Farzaneh Zohrabi[50]

[1] Department of Physics and Astronomy, George Mason University, 4400 University Drive, Fairfax, VA 22030, USA; mreefe@gmu.edu
[2] Instituto de Astrofísica de Andalucía (IAA-CSIC), Glorieta de la Astronomía s/n, E-18008 Granada, Spain
[3] Department of Earth Sciences, University of Hawai'i at Mänoa, Honolulu, HI 96822, USA
[4] Department of Physics and Astronomy, University of California, Irvine, Irvine, CA 92697, USA
[5] University of Grenoble Alpes, CNRS, IPAG, F-38000 Grenoble, France
[6] Observatoire de Genève, Département d'Astronomie, Université de Genève, Chemin Pegasi 51b, 1290 Versoix, Switzerland
[7] NASA JPL, 4800 Oak Grove Drive, Pasadena, CA 91109, USA
[8] IPAC, 770 South Wilson Avenue, Pasadena, CA 91125, USA
[9] Instituto de Astrofísica de Canarias, C. Vía Láctea, s/n, E-38205, Spain
[10] Instituto de Astrofísica de Canarias (IAC), E-38200 La Laguna, Tenerife, Spain
[11] Dept. Astrofísica, Universidad de La Laguna (ULL), E-38206 La Laguna, Tenerife, Spain
[12] Department of Physics and Astronomy, Vanderbilt University, 2201 West End Avenue, Nashville, TN 37235, USA
[13] Center for Astrophysics, Harvard & Smithsonian, 60 Garden Street, Cambridge, MA 02138, USA
[14] Université de Montréal, 2900 Edouard Montpetit Boulevard, Montreal, Quebec, H3T 1J4, Canada
[15] NASA Ames Research Center, Moffett Field, CA 94035, USA
[16] NASA Goddard Space Flight Center, 8800 Greenbelt Road, Greenbelt, MD 20771, USA
[17] Space Telescope Science Institute, 3700 San Martin Drive, Baltimore, MD 21218, USA
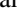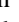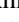[18] Proto-Logic LLC, 1718 Euclid Street NW, Washington, DC 20009, USA
[19] Kavli Institute for Astrophysics and Space Research, Massachusetts Institute of Technology, 77 Massachusetts Avenue, Cambridge, MA 02139, USA
[20] Department of Astronomy, University of Florida, Gainesville, FL 32611, USA
[21] Department of Astronomy & Astrophysics, University of Chicago, 5640 South Ellis Avenue, Chicago, IL 60637, USA
[22] NASA Exoplanet Science Institute, Caltech/IPAC, Mail Code 100-22, 1200 E. California Boulevard, Pasadena, CA 91125, USA
[23] Woodson High School, 9525 Main Street, Fairfax, VA 22031, USA
[24] Dept. of Physics, University of Warwick, Gibbet Hill Road, Coventry, CV4 7AL, UK
[25] Centre for Exoplanets and Habitability, University of Warwick, Coventry, CV4 7AL, UK
[26] University of Naples Federico II, Corso Umberto I, 40, I-80138 Napoli NA, Italy
[27] Department of Astronomy & Astrophysics, 525 Davey Laboratory, The Pennsylvania State University, University Park, PA 16802, USA
[28] Center for Exoplanets and Habitable Worlds, 525 Davey Laboratory, The Pennsylvania State University, University Park, PA 16802, USA
[29] University of Kansas, 1450 Jayhawk Boulevard, Lawrence, KS 66045, USA
[30] Astronomy Department, University of California, Berkeley, CA 94720, USA
[31] Institute of Planetary Research, German Aerospace Center, Rutherfordstrasse 2, D-12489, Berlin, Germany
[32] Komaba Institute for Science, The University of Tokyo, 3-8-1 Komaba, Meguro, Tokyo 153-8902, Japan
[33] Instituto de Astrofísica de Canarias (IAC), E-38205 La Laguna, Tenerife, Spain
[34] Earth and Planets Laboratory, Carnegie Institution for Science, 5241 Broad Branch Road NW, Washington, DC 20015, USA
[35] Department of Physics and Astronomy, Mississippi State University, 75 B.S. Hood Road, Mississippi State, MS 39762, USA
[36] Department of Astronomy and Astrophysics, University of California, Santa Cruz, 1156 High Street, Santa Cruz, CA 95064, USA
[37] Department of Physics, Mathematics, and Astronomy, California Institute of Technology, 1200 E California Boulevard, Pasadena, CA 91125, USA
[38] Department of Astronomy and Astrophysics, Pennsylvania State University, State College, PA 16801, USA
[39] Department of Astronomy, Graduate School of Science, The University of Tokyo, 7-3-1 Hongo, Bunkyo-ku, Tokyo 113-0033, Japan
[40] United States Naval Observatory, 3450 Massachusetts Avenue NW, Washington, DC 20392, USA
[41] Astrobiology Center, 2-21-1 Osawa, Mitaka, Tokyo 181-8588, Japan
[42] Department of Physics and Astronomy, University of Macquarie, Sydney, Australia
[43] Astrophysics Group, Cavendish Laboratory, J.J. Thomson Avenue, Cambridge, CB3 0HE, UK
[44] Princeton University, Department of Astrophysical Sciences, 4 Ivy Lane, Princeton, NJ 08540, USA
[45] Landessternwarte, Zentrum für Astronomie der Universität Heidelberg, Königstuhl 12, D-69117 Heidelberg, Germany
[46] Department of Physics and Astronomy, Carleton College, Sayles Hill Campus Center, North College Street, Northfield, MN 55057, USA
[47] Department of Astronomy, Tsinghua University, Beijing 100084, People's Republic of China

[48] Penn State Extraterrestrial Intelligence Center, 525 Davey Laboratory, The Pennsylvania State University, University Park, PA 16802, USA
[49] Institut für Astrophysik, Georg-August-Universität, Friedrich- Hund-Platz 1, D-37077 Göttingen, Germany
[50] Department of Physics and Astronomy, Louisiana State University, 202 Nicholson Hall, Baton Rouge, LA 70803, USA

Abstract

We present the validation of a transiting low-density exoplanet orbiting the M2.5 dwarf TOI 620 discovered by the NASA Transiting Exoplanet Survey Satellite (TESS) mission. We utilize photometric data from both TESS and ground-based follow-up observations to validate the ephemerides of the 5.09 day transiting signal and vet false-positive scenarios. High-contrast imaging data are used to resolve the stellar host and exclude stellar companions at separations $\gtrsim 0\farcs 2$. We obtain follow-up spectroscopy and corresponding precise radial velocities (RVs) with multiple precision radial velocity (PRV) spectrographs to confirm the planetary nature of the transiting exoplanet. We calculate a 5σ upper limit of $M_P < 7.1\ M_\oplus$ and $\rho_P < 0.74\ \mathrm{g\,cm^{-3}}$, and we identify a nontransiting 17.7 day candidate. We also find evidence for a substellar ($1–20\ M_J$) companion with a projected separation $\lesssim 20$ au from a combined analysis of Gaia, adaptive optics imaging, and RVs. With the discovery of this outer companion, we carry out a detailed exploration of the possibilities that TOI 620 b might instead be a circum-secondary planet or a pair of eclipsing binary stars orbiting the host in a hierarchical triple system. We find, under scrutiny, that we can exclude both of these scenarios from the multiwavelength transit photometry, thus validating TOI 620 b as a low-density exoplanet transiting the central star in this system. The low density of TOI 620 b makes it one of the most amenable exoplanets for atmospheric characterization, such as with the James Webb Space Telescope and Ariel, validated or confirmed by the TESS mission to date.

Unified Astronomy Thesaurus concepts: Near infrared astronomy (1093); Optical astronomy (1776); Radial velocity (1332); Transit photometry (1709); Astronomy data analysis (1858)

1. Introduction

The most successful method for discovering planets around other stars (exoplanets) is the photometric transit method, which measures the periodic dip in brightness from a star that is observed as a planet passes in front of it. The orbital period and the size of the planet relative to the star can be readily derived from such observations (Seager & Mallen-Ornelas 2003). After its launch in 2009, the Kepler mission (Borucki et al. 2011; Howard et al. 2012) accelerated the discovery of Neptune- and terrestrial-sized transiting exoplanets, while the Transiting Exoplanet Survey Satellite (TESS; Ricker et al. 2015), launched in 2018, has identified over 4000 candidate exoplanets orbiting relatively nearby, bright host stars suitable for further characterization. However, the candidates discovered by the TESS mission need further supporting observations, such as archival photometry, ground-based light curves, high-contrast imaging, and reconnaissance spectroscopy, to validate and confirm that they are not false positives. Out of these 4000 candidates, 161 have been validated and/or confirmed to date. Due to the relatively large TESS pixels spanning $22''$ on the sky, fainter visual eclipsing binaries can blend with the nearby bright target stars and produce false positives (barring instrumental artifacts). This is an important consideration, particularly when only a single transiting planet is found in the TESS 27 day time baseline of sector observations, at lower ecliptic latitudes, and away from the ecliptic poles (Lissauer et al. 2012; Vanderburg et al. 2019; Rodríguez Martínez et al. 2020; Hobson et al. 2021; Addison et al. 2021; Osborn et al. 2021; Dreizler et al. 2020;

Brahm et al. 2020; Nowak et al. 2020; Teske et al. 2020; Sha et al. 2021; Gan et al. 2021; Bluhm et al. 2020).

Complementary to exoplanet transit observations are radial velocity (RV) signals which undergo periodic variations from the stellar reflex motions of orbiting exoplanets, thereby inferring planet masses modulo an unknown inclination (Mayor & Queloz 1995; Fischer et al. 2016). We can leverage the strengths of both the RV and transit methods to provide independent confirmations on quantities that can be measured with both methods (such as the orbital period and ephemerides), constrain the orbital inclination, and determine mean densities. Among sub-Jovian planets, mean density informs us about interior composition and the presence or absence of a thick atmosphere of H and He (e.g., Southworth 2010; Marcy et al. 2014; Rogers 2015; Fulton et al. 2017; Bitsch et al. 2019; Zeng et al. 2019).

Direct exploration of exoplanet compositions and atmospheres can exploit differential observations during primary transits of the planet in front of the host star (i.e., spectroscopy of an atmosphere in transmission) or secondary eclipse of the planet by the star (i.e., spectroscopy of an atmosphere in emission; e.g., Line et al. 2013, 2013; Kreidberg et al. 2015; Sing et al. 2016; Deming et al. 2013; Greene et al. 2015). Although some limited observations can be done from the ground (e.g., Nortmann et al. 2018; Allart et al. 2018), due to interference from Earth's atmosphere, most of these have been obtained by space telescopes such as the Hubble Space Telescope (HST; Ehrenreich et al. 2015). The launch of the James Webb Space Telescope (JWST; Beichman & Greene 2018) and Ariel (Tinetti et al. 2016) will usher in a new era of spectral resolution, precision, and stability at the infrared wavelengths where many important atmospheric molecules have absorption features.

Even with such advances in instrumentation, these demanding observations require planets transiting nearby bright but comparatively small stars for which the expected signal-to-noise ratio (S/N) will be highest. The primary mission of TESS is to identify such systems: their suitability for transit and secondary eclipse spectroscopy can be quantified by two metrics related to the S/N (Kempton et al. 2018). In addition,

---

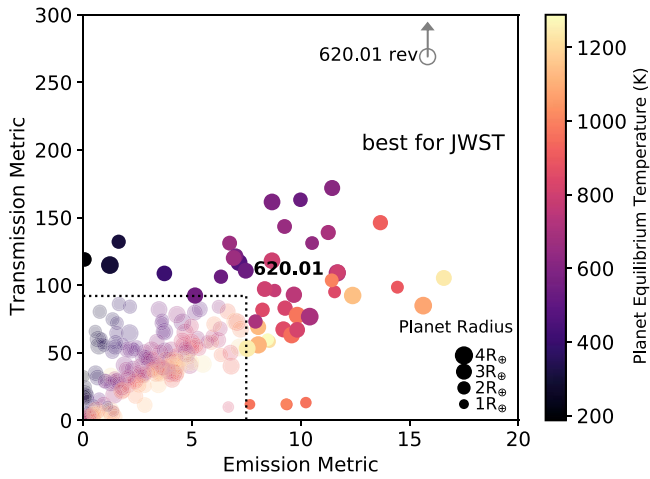[51] NASA Earth and Space Science Fellow.

Figure 1. Kempton et al. (2018) metrics of signal-to-noise (S/N) for hypothetical observations of exoplanet atmospheres in transmission (during primary transit) and emission (during secondary eclipse) for a subset of TESS candidate or confirmed planets (TOIs) detected as of the end of 2021 September (NASA Exoplanet Archive, IPAC 2013; Akeson et al. 2013). Only planets smaller than Neptune, with $T_{eq} < 1300$ K, and that are predicted to impart a Doppler RV signal $K > 3$ m s^{-1} are shown. Planet masses are estimated from the Chen & Kipping (2016) mass–radius relation and are thus only preliminary. The points' sizes are scaled with planet radius and the colors are keyed to T_{eq}. Increased metric means higher S/N, and the dashed lines indicate the boundary above and to the right of which systems are suitable for JWST observations (Kempton et al. 2018). Candidate planet TOI 620.01 is presented by its Exoplanet Archive–based value (filled point), and by a value/lower limit based on revised star and planet properties presented in this work (open gray point and arrow).

observations and models point to the planetary equilibrium temperature, T_{eq}, as a fundamental parameter in understanding exoplanet atmospheres: at $T_{eq} > 2000$ K, atmospheres approach thermodynamic equilibrium, there are few or no condensates, and the observable role of photochemistry is minimal; below $T_{eq} < 1300$ K, disequilibrium can readily occur, condensation and photochemistry can be important, and these atmospheres can be complex. The coolest of the cool ($T_{eq} \lesssim 500$ K) are those of interest to searches for biosignatures. Finally, interpretation of observations requires an estimate of a planet's gravity and hence its mass (Batalha et al. 2019; Madhusudhan 2019; Rogers & Seager 2010).

Figure 1 shows preliminary estimates for these two indices from Kempton et al. (2018), the transmission and emission spectroscopy metrics (TSM, ESM), for all TESS candidate planets (TESS Objects of Interest, or TOIs), as of the end of 2021 September, that have radii less than that of Neptune, and are predicted to impart Doppler RV signals with semiamplitudes $K > 3$ m s^{-1}, as a criterion for mass determination. Objects outside the dashed zone are considered suitable targets for transit and/or secondary eclipse observations by the JWST. Thus far, out of the thousands of TESS exoplanet candidates, less than 50 objects satisfy all these criteria, and thus these are some of the most important targets for validation and characterization. Many of these are M-dwarf systems where the small radius and low luminosity of the star mean relatively high transit S/N and low T_{eq}.

One such system, TOI 620.01, is a candidate transiting sub-Neptune-sized planet on a 5.09 day orbit around a nearby (33 pc), bright ($T = 10$ mag) early M-type dwarf (Table 1). We describe a multimethod, multiwavelength, multiinstrument, and multiteam campaign to validate and characterize the planet and its host star, identify or rule out additional

Table 1
Stellar Parameters of TOI 620

Parameter	Value	Reference
	Identifiers	
TIC	296739893	S19
TOI	620	G21
G	161-32	G71
NLTT	21863	L79
Gaia DR2 & EDR3	5738284016370287616	G18
2MASS	J09284158-1209551	S06
	Coordinates & Velocities	
α	09:48:41.59	S19
δ	-12:09:55.75	S19
Distance (pc)	33.055 ± 0.058	G18
Parallax (ϖ) (mas)	30.283 ± 0.061	G18, L18
$\mu_\alpha \cos \delta$ (mas yr^{-1})	35.87 ± 0.11	G18
μ_δ (mas yr^{-1})	-389.854 ± 0.082	G18
X (pc)	-12.521 ± 0.012	this work
Y (pc)	-26.597 ± 0.026	this work
Z (pc)	15.025 ± 0.015	this work
U (km s^{-1})	37.22 ± 0.20	this work
V (km s^{-1})	-40.13 ± 0.42	this work
W (km s^{-1})	-28.14 ± 0.24	this work
	Physical Properties	
Spectral type	M2.5V	S05
$v \sin i$ (km s^{-1})	< 3	this work
P_{rot} (days)	8.99	this work
	(see Table 4)	
	Magnitudes	
B (APASS)	13.58 ± 0.24	H18
V (APASS)	12.265 ± 0.019	H18
g' (APASS)	12.946 ± 0.031	H18
r' (APASS)	11.678 ± 0.018	H18
i' (APASS)	10.667 ± 0.051	H18
z' (APASS)	10.064 ± 0.079	H18
Gaia G	11.3104 ± 0.0013	G18
Gaia B_P	12.4955 ± 0.0022	G18
Gaia R_P	10.2525 ± 0.0013	G18
J (2MASS)	8.837 ± 0.030	S06
H (2MASS)	8.201 ± 0.053	S06
K (2MASS)	7.954 ± 0.027	S06
WISE 3.4 μm	7.839 ± 0.024	W10
WISE 4.6 μm	7.809 ± 0.019	W10
WISE 12 μm	7.733 ± 0.020	W10
WISE 22 μm	7.51 ± 0.14	W10

Note. The physical properties and distance are derived from an EXOFASTv2 fit, detailed in Section 4.2. References: G18: Gaia Collaboration et al. (2018); G21: Guerrero et al. (2021); H18: Henden et al. (2018); S19: Stassun et al. (2019); S06: Skrutskie et al. (2006); S05: Scholz et al. (2005); W10: Wright et al. (2010); L18: Lindegren et al. (2018); G71: Giclas et al. (1971); L79: Luyten (1979).

companions, and assess the suitability and value of the system for future atmospheric investigation by the JWST and other observatories.

This paper is organized as follows. In Section 2, we present our baseline of 2 yr of RV observations using the near-infrared (NIR) iSHELL spectrograph (Cale et al. 2019), along with a single season of RV data from the Calar Alto high-Resolution search for M dwarfs with Exo-earths with Near-infrared and optical Echelle Spectrographs (CARMENES), the M dwarf Advanced Radial velocity Observer Of Neighboring eXoplanets (MAROON-X), and the NN-explore Exoplanet Investigations

Table 2
Summary of All Transit, High-contrast Imaging, and RV Observations Used in this Work

Instrument/Facility	$N_{transits}$	Filter	Plate Scale	Precision
TESS	8	TESS	$22'' \, px^{-1}$	1×10^{-3}
NGTS/Paranal	2	NGTS	$5'' \, px^{-1}$	1×10^{-2}
CTIO 1 m/LCO	1	z'	$0.''389 \, px^{-1}$	8×10^{-4}
TMMT/LCO	1	I	$1.''19 \, px^{-1}$	2×10^{-3}
MuSCAT2/TCS	4	g', i', r', z'	$0.''44 \, px^{-1}$	2×10^{-3}
KeplerCam/FLWO	1	B	$0.''672 \, px^{-1}$	2×10^{-3}
LCRO/LCO	1	i'	$0.''773 \, px^{-1}$	4×10^{-3}
ExTrA/La Silla	4	ExTrA	$0.''870 \, px^{-1}$	2×10^{-3}

Instrument/Facility	UT Observation Dates	Wavelength	Separation Range
Zorro/Gemini South	2020-03-16	562 nm, 832 nm	$0.''02$–$1.''2$
NIRC2/Keck II	2019-05-12	Brγ	$0.''02$–$4''$
NIRI/Gemini North	2019-05-23	Brγ	$0.''02$–$7''$
NESSI/WIYN	2019-11-09	562 nm, 832 nm	$0.''04$–$1.''2$
ShaneAO/Lick	2021-02-26, 2021-02-27	K_s, J	$0.''6$–$7''$

Instrument/Facility	λ (Å)	$\lambda/\Delta\lambda$ ($\times 10^3$)	N_{nights}	N_{used}	σ_{RV} (m s^{-1})	Pipeline
iSHELL/IRTF	10,600–53,000	85	34	31	5.3	pychell (Cale et al. 2019)
CARMENES-Vis/Calar Alto	5200–9600	94.6	7	6	1.7	serval (Zechmeister et al. 2018)
CARMENES-NIR/Calar Alto	9600–17100	80.4	7	7	7.2	serval (Zechmeister et al. 2018)
MAROON-X blue/Gemini North	5000–6780	85	8	8	2.3	serval (Zechmeister et al. 2018)
MAROON-X red/Gemini North	6540–9200	85	8	8	1.9	serval (Zechmeister et al. 2018)
NEID/WIYN	4580–8920	120	8	8	1.1	serval (Zechmeister et al. 2018)
TRES/Tillinghast	3850–9096	44	2	2	⋯	⋯

Note. In the transit column headings, $N_{transits}$ denotes the number of transits observed by that instrument and Precision denotes the order of magnitude of the normalized flux error for each instrument. In the RV column headings, N_{nights} and N_{used} refer to the number of nights gathered and the number used, respectively. The median intrinsic error bars σ_{RV} are calculated using only the nights used.

with Doppler spectroscopy (NEID). We supplement the TESS light curve with ground-based multiwavelength follow-up observations from the Next Generation Transit Survey (NGTS), the Las Cumbres Observatory (LCO), the Multicolor Simultaneous Camera for studying Atmospheres of Transiting exoplanets 2 (MuSCAT2), the Three-hundred MilliMeter Telescope (TMMT), the Exoplanets in Transit and their Atmospheres (ExTrA) facility, and KeplerCam, and reconnaissance spectroscopy from the Tillinghast Reflector Echelle Spectrograph (TRES). Section 3 overviews the analysis and results of fitting of the host-star properties, including multiplicity and age. We present analysis and results of the light-curve transit fitting in Section 4 and RV fitting in Section 5. In Section 6 we discuss the implications of our modeling, analyzing the effects of stellar activity and possible additional RV signals, and perform injection and recovery tests. In Section 7 we summarize our findings. Finally, in the Appendices, we present more detailed explorations of alternative circum-secondary and hierarchical eclipsing binary (HEB) scenario analyses that are motivated by the Gaia reduced unit weighted error (RUWE) statistic, linear RV trend, and iSHELL SB2 analysis presented in the paper.

2. Observations

In this section, we present an overview of all observational data used in our analysis. All photometric light-curve data is presented in Section 2.1, all high-contrast imaging observations are in Section 2.2, and all RV observations are detailed in Section 2.3. A description of reconnaissance spectroscopy is

also presented in Section 2.4. A summary of all space and ground-based transit data, high-contrast imaging data, and spectroscopic RV data is shown in Table 2. For more detailed information on the specific transit times or individual RV measurements, refer to Appendices B and C.

2.1. Time-series Photometry

2.1.1. Transiting Exoplanet Survey Satellite Photometry

TOI 620 (TIC 296739893; G 161-32; Gaia EDR3 5738284016370287616) was observed first in TESS Sector 8 from UT 2019 February 2 to 2019 February 27, then in Sector 35 during the TESS extended mission from UT 2021 February 9 to 2021 March 6. The star is located at a distance of 33.06 pc and is relatively bright (e.g., $V = 12.265$, $J = 8.837$) making it an ideal candidate for study by TESS.

The data collection pipeline developed by the TESS Science Processing Operations Center (SPOC; Jenkins et al. 2016) extracted the photometry for this target and performed a search for transiting planets using a wavelet-based matched filter (Jenkins 2002; Jenkins et al. 2010, 2020) on 29 March 2019, detecting a strong transit signal. The data were fitted with a limb-darkened transit model (Li et al. 2019) and subjected to a suite of diagnostic tests (Twicken et al. 2018) to distinguish between false positives and a planetary signal. The signature passed all the data validation tests, including the difference image centroiding test, which localized the source of the transits to within $4.''2980 \pm 2.''6862$ of the target star. A search
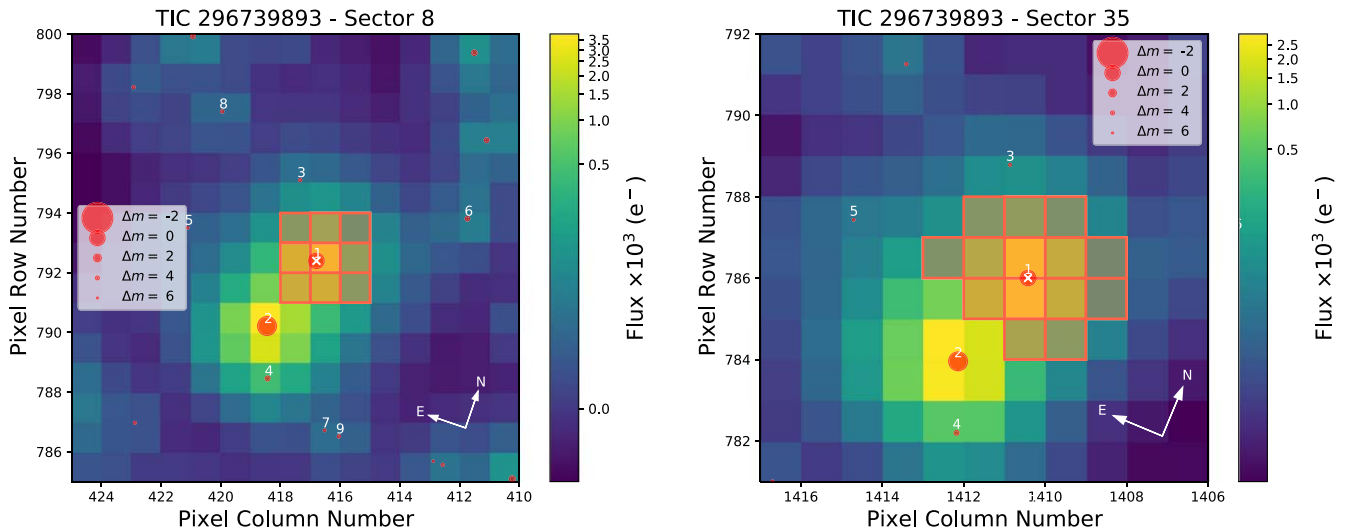
Figure 2. TESS target pixel file (TPF) data from Sector 8 (left) and Sector 35 (right) for TOI 620, created with `tpfplotter` (Aller et al. 2020). The pixels shown outlined in orange were the ones used to extract the light curve, while point sources from the Gaia DR2 catalog are labeled in red, with sizes in accordance to their relative magnitude from the target star.

for additional planetary transit signatures failed to identify any. The TESS Science Office reviewed the vetting results and issued an alert for TOI 620.01 on 13 April 2019 (Guerrero et al. 2021), which hereafter we also refer to as TOI 620 b. In Figure 2, we show the TESS target pixel files (TPFs) around the target star in Sectors 8 and 35, where orange outlines show the aperture pixels used to extract the TESS light curve. A slightly brighter visual companion is located $55''$ to the south-southeast, which does contribute (less than a few percent) to the TESS aperture for TOI 620; thus, in the validation presented in this work, we do exclude this companion as the source of the transit and photometric variations. We specifically analyzed the detrended presearch data conditioning simple aperture photometry (PDC-SAP) light curve (Smith et al. 2012; Stumpe et al. 2012, 2014) obtained from the Mikulski Archive for Space Telescopes (MAST).[52] We normalize the light curves for each sector to unity.

2.1.2. Next Generation Transit Survey/Paranal

TOI 620 was observed by the NGTS (Wheatley et al. 2018) on the nights of 2019 April 20 and 2019 June 10. The NGTS photometric facility consists of 12 0.2 m diameter robotic telescopes, located at the ESO's Paranal Observatory, Chile. On the night of 2019 April 20, TOI 620 was observed using a single NGTS telescope and on 2019 June 10 two telescopes were used in the simultaneous multitelescope observing mode to independently observe TOI 620 (see Bryant et al. 2020). For both nights, TOI 620 was observed using the custom NGTS filter (520–890 nm) and an exposure time of 10 s. Across the two nights, a total of 2675 images were taken. The NGTS data were reduced using a custom aperture photometry pipeline, which performs source extraction and photometry using the SEP Python library (Bertin & Arnouts 1996; Barbary 2016) and is detailed in Bryant et al. (2020). The pipeline uses Gaia Data Release 2 (DR2; Gaia Collaboration et al. 2016, 2018) to automatically identify comparison stars which are similar in brightness, color, and CCD position to TOI 620.

2.1.3. Cerro Tololo Inter-American Observatory 1 m/LCO

The Las Cumbres Observatory at Cerro Tololo Inter-American Observatory in Chile (LCO-CTIO; Brown et al. 2013) observed TOI 620 on the same night, UT 2019 April 20, as NGTS using the 1 meter telescope, in the Sloan Digital Sky Survey (SDSS) z' filter. The plate scale is $0''389$, giving a full FOV of $26'5 \times 26'5$. Exposure times were 30 s, and the sizes chosen for the aperture and sky annuli were 15 pixels ($5''835$), 30 pixels ($11''67$), and 45 pixels ($17''505$), respectively. The ingress was missed, but a full egress was captured. Data was reduced using an AstroImageJ (AIJ; Collins et al. 2017) pipeline.

2.1.4. Multicolor Simultaneous Camera for studying Atmospheres of Transiting exoplanets 2/TCS

The MuSCAT2 camera at the Telescopio Carlos Sánchez in the Teide Observatory, Spain (Narita et al. 2015, 2018), has observed TOI 620 in its four simultaneous bands (g', i', r', and z') on four separate nights. Different aperture sizes were used on each night, ranging from $7''83$–$13''92$, with inner and outer sky annuli being an additional $10''$ and $18''7$ out from the target aperture. Partial transits covering a full ingress and partial egress were observed on the nights of UT 2020 January 16, 2020 March 2, 2020 April 16, and 2021 January 7. On the final night, January 7, the g' band was unavailable for observations, so this night used only the other three filters. The data were reduced using a custom Python pipeline developed specifically for MuSCAT2 (Narita et al. 2018).

2.1.5. KeplerCam/FLWO

TOI 620 was also observed by the KeplerCam (Szentgyorgyi et al. 2005) on UT 2020 January 26 in the B filter. KeplerCam is a $4\,K \times 4\,K$ Fairchild detector on the 1.2 m telescope at the Fred Lawrence Whipple Observatory (FLWO) atop Mt. Hopkins (Arizona, USA). The detector has a pixel scale of $0''672\,\mathrm{pixel}^{-1}$ resulting in a field of view of $23'1 \times 23'1$. A full transit was observed using 60 s observations with $\sim 1''9$ FWHM and a $3''4$ circular aperture.

2.1.6. Three-hundred MilliMeter Telescope/LCO

We observed a transit of TOI 620 b on UT 2019 April 26 using the TMMT (Monson et al. 2017) at Las Campanas Observatory in Chile. TMMT is a $f/7.8$ FRC300 telescope from Takahashi on a German equatorial AP1600 GTO mount with an Apogee Alta U42-D09 CCD Camera, FLI Atlas focuser, and Centerline filter wheel.

Observations were performed using the Bessell I filter with exposure times of 70 s. TMMT has a gain of 1.35e/ADU and a plate scale of $1''19\,\mathrm{pixel}^{-1}$ for a field of view of $40'8$. The target rose from an air mass of 1.06 at the start of the observations to a minimum air mass of 1.04 and then set to an air mass of 1.68 at the end of the observations. In addition to the standard bias, dark, and flat corrections, a fringe subtraction was also performed for the TMMT I-band images.

We reduced this data using AIJ. The final light curve utilized a photometric aperture of 9 pixels ($5''97$), and inner and outer sky annuli of 15 pixels ($23''9$) and 25 pixels ($35''8$), respectively.

2.1.7. Las Campanas Remote Observatory/LCO

We also observed an ingress of TOI 620 b on UT 2020 November 27 using the 305mm Las Campanas Remote Observatory (LCRO) telescope at the Las Campanas Observatory in Chile. The LCRO telescope is an $f/8$ Maksutov–Cassegrain from Astro-Physics on a German Equatorial AP1600 GTO mount with an FLI Proline 16803 CCD Camera, FLI Atlas focuser and Centerline filter wheel.

Observations were performed using the SDSS i' filter with exposure times of 120 s. In this mode, LCRO has a gain of 1.52e/ADU and a plate scale of $0''773\,\mathrm{pixel}^{-1}$ for a field of view of $52'0$. The target rose from an air mass of 3.6 at the start of observations, to 1.07 at the end.

We also reduced this data with AIJ, in the same fashion as the TMMT transit. For the final reduction, we selected a photometric aperture of 13 pixels ($10''0$) with an inner sky annulus of 15 pixels ($11''6$) and outer sky annulus of 20 pixels ($15''5$).

2.1.8. Exoplanets in Transit and their Atmospheres/La Silla

The ExTrA facility (Bonfils et al. 2015) is composed of an NIR (0.85 to 1.55 μm) multiobject spectrograph fed by three 60 cm telescopes located at La Silla observatory. We observed five full transits of TOI 620 b on UTC 2021 March 3, 2021 April 13 (with two telescopes), 2021 April 18, and 2021 June 3. We observed with one or two telescopes using the fibers with $8''$ apertures. We used the low-resolution mode of the spectrograph ($R\sim 20$) and 60 s exposures for all nights. At the focal plane of each telescope, five fiber positioners are used to pick the light from the target and four comparison stars. As comparison stars, we also observed Two Micron All Sky Survey (2MASS) J09265392-1229161, 2MASS J09275007-1222230, 2MASS J09270219-1156332, and 2MASS J09261086-1200503, with J-magnitude (Skrutskie et al. 2006) and T_{eff} (Gaia Collaboration et al. 2018), similar to TOI 620. The resulting ExTrA data were analyzed using custom data-reduction software.

2.2. High-contrast Imaging

2.2.1. Zorro/Gemini South

TOI 620 was observed on 2020 March 16 UT using the Zorro speckle instrument on Gemini South[53] in Chile. Zorro provides simultaneous speckle imaging in two bands (562 nm and 832 nm) with output data products including a reconstructed image and robust contrast limits on companion detections (e.g., Howell et al. 2016). Five sets of 1000×0.06 sec exposures were collected and subjected to Fourier analysis in our standard reduction pipeline (see Howell et al. 2011).

2.2.2. NIRI/Gemini North

We collected observations of TOI 620 with the NIRI adaptive optics (AO) imager (Hodapp et al. 2003) at the Gemini North facility in Maunakea, Hawaii, USA on 2019 May 23. We collected nine frames, with individual exposure times of 1.8 s, in the Brγ filter, and dithered the telescope by $\sim3''3$ between each frame in a grid pattern. A sky background was removed by median-combining the individual science frames, thereby removing the signal from the star and any companions, and we also collected flat frames. For each image we first removed bad pixels, flat-fielded, and subtracted the sky background. We then aligned the frames to the position of the star in each image, and coadded the sequence.

2.2.3. NIRC2/Keck II

NIRC2 is designed for the Keck AO system in Maunakea, Hawaii, USA, as a NIR imager. Observations of TOI 620 were performed with this instrument on UT 2019 May 12 so as to further constrain the parameter space of possible companions in the TOI 620 system, as part of the standard process for doing so (Ciardi et al. 2015; Schlieder et al. 2021). A three-point dither pattern is commonly used with NIRC2 to avoid using the noisier lower-left detector quadrant. Observations were made in the Brγ filter.

2.2.4. NN-Explore Exoplanet Stellar Speckle Imager/WIYN

We observed TOI 620 with the NN-Explore Exoplanet Stellar Speckle Imager (NESSI; Scott et al. 2018) on the WIYN 3.5 m telescope at Kitt Peak National Observatory, Arizona, USA on 2019 November 9. Sequences of 40 ms, diffraction-limited exposures were collected in the instrument's blue and red channels (with 562 nm and 832 nm filters, respectively). The data were reduced following Howell et al. (2011).

2.2.5. ShaneAO/Lick

We obtained high-contrast AO images of TOI 620 from the 3 m Shane Telescope at Lick Observatory, California, USA on the successive nights of 2021 Feb 26 and 27. The AO imaging was carried out in the K_s and J bandpasses using the ShARCS camera (Srinath et al. 2014). We observed both bandpasses with a five-point dither pattern (see, e.g., Furlan et al. 2017), imaging the star at four quadrants of the detector as well as the center. We used custom Python software to perform standard image processing, including flat-fielding, sky subtraction, and subpixel image alignment.

---

[53] https://www.gemini.edu/sciops/instruments/alopeke-zorro/

2.3. Radial Velocities

In this section we present the RV data collected for TOI 620 from four different precision radial velocity (PRV) spectrographs spanning the visible through NIR wavelengths. Taken in isolation, each spectrograph did not obtain a substantial number of RV epochs (with the exception of the lower-precision iSHELL). However, collectively the RVs are sufficient in number (Plavchan et al. 2015) to permit a robust search for TOI 620 b.

2.3.1. iSHELL/IRTF

We have gathered a total of 379 observations of TOI 620 over 34 nights using the iSHELL instrument at NASA IRTF in Maunakea, Hawaii, USA from UT 2020 January 26 to UT 2021 June 4. iSHELL observes in a range of wavelengths around 2350 nm. Exposure times were 300 s, and were repeated anywhere from nine to 17 times consecutively per night to obtain a S/N of 87–155 per spectral pixel. A methane isotopologue ($^{13}CH_4$) gas cell is used to provide a common optical path wavelength reference and to constrain the variable line spread function (LSF) of the spectrograph (Anglada-Escudé et al. 2012; Plavchan et al. 2013a). Raw iSHELL data are processed in pychell with updated methods to those described in Cale et al. (2019). For a detailed description of these updated methods, refer to Appendix A.

2.3.2. Calar Alto high-Resolution search for M dwarfs with Exo-earths with Near-infrared and optical Echelle Spectrographs/Calar Alto

The CARMENES instrument, located at the Calar Alto Observatory in Spain (Quirrenbach et al. 2018), consists of visual and NIR arms covering a wavelength range of 520–960 nm and 960–1710 nm, respectively. We obtained seven measurements with exposure times of ∼1800 s of TOI 620 from UT 2021 February 3 to 2021 March 28 in both the visual and NIR arms, but we were not able to use the first visual arm measurement from UT 2021 February 3 due to drift in the Fabry–Pérot wavelength-calibration device. The CARMENES RVs were processed using the SERVAL pipeline (Zechmeister et al. 2018).

2.3.3. M dwarf Advanced Radial velocity Observer Of Neighboring eXoplanets/Gemini North

The MAROON-X instrument (Seifahrt et al. 2018) is mounted at the Gemini North facility at Maunakea, Hawaii, USA, and, like CARMENES, it consists of two arms of differing wavelength ranges. The blue arm covers 500–678 nm, while the red arm covers 654–920 nm, both with a resolving power of $R \approx 85,000$. We observed TOI 620 with this instrument from UT 2021 February 24 to 2021 June 3, gathering a total of eight measurements in both arms, with exposure times of 300 s. The RVs are processed using a dedicated version of the SERVAL pipeline.

In the middle of the time span that RVs were collected with the MAROON-X instrument, the observatory cooling system failed, causing a significant state change in the instrument's calibration, affecting the absolute RV offsets. To correct for the relative errors introduced by this state change, we applied offset terms for each time range between the dates on which the instrument was affected. This occurred once between 2021 February 24 and April 17, and once between 2021 April 30 and May 7. These offsets are applied in addition to the standard γ offsets applied to each instrument in the main Markov Chain Monte Carlo (MCMC) analysis presented later herein. We subtracted a random sample from a normal distribution with a prior center and standard deviation summarized in the Appendix for each time span. The values of the offsets and errors were estimated using data from stars of a similar type that were observed during the same observation runs.

2.3.4. NN-explore Exoplanet Investigations with Doppler spectroscopy/WIYN

We obtained precise broadband-optical, fiber-fed RVs of TOI 620 using the newly commissioned NEID spectrometer (Schwab et al. 2016) on the 3.5 m WIYN Telescope at Kitt Peak National Observatory, Arizona, USA. All NEID nights on WIYN are queue scheduled, and we obtained eight queue-scheduled observations of TOI 620 between January and May of 2021.

Each NEID observation consisted of 2×900 s exposures in the instrument's high-resolution (HR) mode, which yields a resolving power of $R \sim 120,000$. The exposures were taken without a simultaneous source on the calibration fiber in order to avoid cross contamination with the relatively faint target. The exposures have a median S/N of 11.8 per one-dimensional extracted pixel evaluated at $\lambda = 550$ nm.

Basic data reduction and spectral extraction were performed by the automated NEID data pipeline. The barycentric corrections were performed using the algorithms from Wright & Eastman (2014) implemented in barycorrpy (Kanodia & Wright 2018). We extracted precise RVs from the extracted spectra using a modified version of the SERVAL pipeline (Zechmeister et al. 2018), which we describe further in a forthcoming publication (Stefansson et al. 2021, in preparation). SERVAL uses the template-matching technique (Anglada-Escudé & Butler 2012), which is particularly effective for cool stars. For the RV reduction, we used NEID order indices 40 to 104, spanning wavelengths from 4580 Å to 8920 Å. We note that the SERVAL RVs are consistent with the RVs computed by the automated pipeline, which uses the cross-correlation function mask technique, but yields significantly higher RV precision for M-dwarf stars as it is capable of using a higher fraction of the RV information content inherent in M-dwarf spectra.

2.4. Recon Spectroscopy: The Tillinghast Reflector Echelle Spectrograph

The TRES (Fűrész 2008; Szentgyorgyi et al. 2005) obtained two reconnaissance spectra of TOI 620 on UT 2019 April 22 and 2019 April 25, covering a wavelength range of 385–909.6 nm. Spectra were processed using methods outlined in Buchhave et al. (2010) and Quinn et al. (2014), with the exception of the cross-correlation template, for which the high-S/N median observed spectrum is used instead. The extracted spectra are available at the NASA Exoplanet Archive EXO-FOP data repository (IPAC 2015; Akeson et al. 2013).

3. System Characterization

In this section we examine the properties of the TOI 620 stellar system itself and model the luminous bodies of the system under various assumptions. In Section 3.1 we present

Table 3
Prior Probability Distributions for our EXOFASTv2 MCMC Simulations

Parameter (units)	Initial Value (P_0)	Priors	Prior Citation
A_V (mag)	0	$\mathcal{U}(P_0, 0.12)$	S11
ϖ (mas)	30.283	$\mathcal{N}(P_0, 0.061)$	G18
[Fe/H]	0	$\mathcal{N}(0, 1)$	This work
Gaia G	11.31	$\mathcal{N}(P_0, 0.02)$	G18
Gaia B_P	12.50	$\mathcal{N}(P_0, 0.02)$	G18
Gaia R_P	10.25	$\mathcal{N}(P_0, 0.02)$	G18
J 2MASS	8.837	$\mathcal{N}(P_0, 0.010)$	S06
H 2MASS	8.201	$\mathcal{N}(P_0, 0.053)$	S06
K 2MASS	7.954	$\mathcal{N}(P_0, 0.027)$	S06
WISE1	7.839	$\mathcal{N}(P_0, 0.030)$	W10
WISE2	7.809	$\mathcal{N}(P_0, 0.030)$	W10
WISE3	7.733	$\mathcal{N}(P_0, 0.030)$	W10
WISE4	7.51	$\mathcal{N}(P_0, 0.14)$	W10

Note. $\mathcal{N}(\mu, \sigma)$ signifies a Gaussian prior with mean μ and standard deviation σ. $\mathcal{U}(\ell, r)$ signifies a uniform prior with left bound ℓ and right bound r. A_V is the extinction in the V band, and ϖ is the parallax. Parameters that are not included here, including stellar M_*, R_*, and T_{eff}, were not constrained by any priors, and were given an initial MCMC starting value of Sun-like to assess the robustness of the MCMC posterior convergence on an M-dwarf host star. References: S11: Schlafly & Finkbeiner (2011); G18: Gaia Collaboration et al. (2018); S06: Skrutskie et al. (2006); W10: Wright et al. (2010).

analysis of the reconnaissance spectroscopy measurements of TOI 620 from TRES. Then, in Section 3.2 we model the TOI 620 star, under the assumption that it is a single star, using Mesa Isochrones and Stellar Tracks (MIST) isochrones and a spectral energy distribution (SED). In Section 3.5 we present the results of analyses of the high-contrast imaging data, followed by historical imaging data in Section 3.6. Then, in Section 3.7 we explore the possibility of stellar multiplicity, and Section 3.8 presents a two-star model of the iSHELL spectra.

3.1. Tillinghast Reflector Echelle Spectrograph Spectroscopy Results

From examining the TRES spectra's NIR TiO lines, we find absolute velocities of 6.25 and 6.23 km s^{-1}. The corresponding absolute velocities from the Mg b-containing order are 6.48 and 6.17 km s^{-1}, both with errors of $\sim$0.25 km s^{-1}, meaning we see no significant RV variation between the quadratures of TOI 620 b's orbit (assuming it to be circular). The best fit is achieved with no rotational broadening, so we can confidently place an upper limit on the rotational velocity of $v \sin i <$ 3 km s^{-1}. Estimates for the stellar parameters of TOI 620 can be made from the TRES observations, where we obtain T_{eff} $\sim$3750–4000 K, $\log g_* \sim 4.0$, and $[m/H] \sim 0$. However, since the TRES modeling pipeline uses ATLAS model atmospheres, which are known to not provide accurate stellar spectra for $T_{eff} < 4500$ K, and TOI 620 is an M dwarf with a T_{eff} in this range, the results for these stellar parameters are approximate. Looking at the TRES activity spectroscopic features, we do not find any significant emission in Hα. We do identify line core flux emission in the sodium doublet, but these are relatively narrow emission features and associated with telluric contamination. We also do not identify any lithium absorption consistent with ages of <50 Myr.
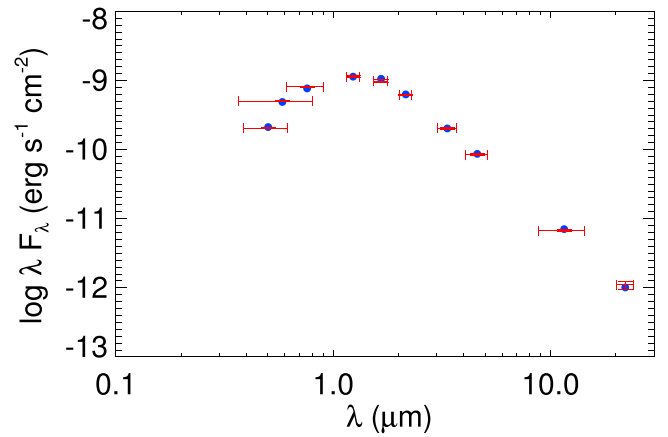

Figure 3. Spectral energy distribution fit of flux as a function of wavelength for TOI 620. Blue points are the best-fit values, and red points are the corresponding model values and errors.

3.2. Fitting Bulk Stellar Properties

We next look at all of our stellar magnitudes and parallax data to more accurately determine the characteristics of the host star, such as effective temperature, gravity, metallicity, etc. We perform a joint ameba fit followed by an MCMC simulation, fitting both stellar properties and planet properties from the transit data of TOI 620 b assuming a single-planet, single-star scenario simultaneously with EXOFASTv2 (Eastman et al. 2013, 2019). Details on the single-planet transit analysis are in the next Section 4, but here we present the results of the stellar modeling. We start the MCMC with as few assumptions as possible–namely, we place no priors on the spectral type, and we employ parallel tempering with eight parallel threads, following Eastman et al. (2019). We place priors on V-band extinction, parallax (corrected as prescribed by Lindegren et al. 2018), and metallicity summarized in Table 3. We simultaneously fit with MIST (Dotter 2016; Choi et al. 2016; Paxton et al. 2011, 2013, 2015) and an SED function. For the SED, we include magnitudes from Gaia DR2, 2MASS, and the Wide-field Infrared Survey Explorer (WISE), which are both precise and span a large wavelength range for broadband M-dwarf SED characterization (Mann et al. 2015). The results of our stellar MCMC modeling are shown in Figure 3 and Table 4.

3.3. Stellar Rotation

Stellar rotation can manifest itself as periodic variation in a light curve (due to spots) or in time series of an activity indicator (due to active regions) or by rotational broadening of lines in a stellar spectrum. Lomb–Scargle (LS) periodograms (Lomb 1976; Scargle 1982) of the TESS Sector 8 and 35 light curves (Figure 4) contain significant peaks at 4.45 days and 8.93 days, respectively. These signals could in principle come from the primary star at one-half and one times the stellar rotation period, respectively (e.g., Reinhold & Reiners 2013). These photometric variations could also originate from an unrelated neighboring star that contributes signal within the photometry aperture; or they could be artifacts, which we now address. The two nearest resolved stars in the Gaia EDR3 catalog are TIC 296739889 (9″2) and TIC 296739884 (34″3), which have estimated T-mag contrasts of 7.0 and 6.8, respectively. The amplitude of the detected periodic signals ($\sim 10^{-3}$; Figure 4) is comparable to

Table 4
Stellar Parameters: Median Values and 68% Confidence Interval for TOI 620

Parameter	Units	Values
Stellar Parameters:		
M_*…	Mass ($M_\odot$)…	$0.577^{+0.024}_{-0.023}$
R_*…	Radius ($R_\odot$)…	0.550 ± 0.017
L_*…	Luminosity ($L_\odot$)…	0.0515 ± 0.0015
F_{Bol}…	Bolometric flux (cgs)…	$1.511^{+0.045}_{-0.044} \times 10^{-9}$
ρ_*…	Density (cgs)…	$4.89^{+0.41}_{-0.39}$
$\log g$…	Surface gravity (cgs)…	$4.718^{+0.024}_{-0.025}$
T_{eff}…	Effective temperature (K)…	3708^{+57}_{-56}
[Fe/H]…	Metallicity (dex)…	$0.35^{+0.11}_{-0.12}$
$[Fe/H]_0$…	Initial metallicity[a]…	$0.31^{+0.10}_{-0.11}$
Age…	Age (Gyr)…	$7.2^{+4.6}_{-4.7}$
EEP…	Equal evolutionary phase[b]…	312^{+14}_{-31}
A_V…	V-band extinction (mag)…	$0.048^{+0.043}_{-0.034}$
σ_{SED}…	SED photometry error scaling…	$1.73^{+0.63}_{-0.40}$
ϖ…	Parallax (mas)…	30.283 ± 0.061
d…	Distance (pc)…	$33.022^{+0.067}_{-0.066}$

Note. Created using EXOFASTv2, commit number 7971a947. See Table 3 in Eastman et al. (2019) for a detailed description of all parameters.
[a] The metallicity of the star at birth.
[b] Corresponds to static points in a star's evolutionary history. See Section 2 in Dotter (2016).

their brightness, making them implausible sources. The third-nearest star, TIC 296739875, is comparable in brightness to TOI 620 ($T = 10.12$), and is the aforementioned (Section 2.1) companion $55''$ to the south-southeast; the light curve of the latter undoubtedly includes scattered light from the former. However, light curves constructed from aperture photometry performed on this star for either sector do not contain a 4.45 or 8.93 day signal (nor any 5.09 day eclipsing signal). The sinusoidal periodic signals are not recovered from the uncorrected simple aperture photometry of TOI 620 b, raising the possibility that they are a processing product. But such signals do not systematically appear in the light curves of all 19 other stars with 2 minute cadence photometry falling within 1° of TOI 620 b, ruling out a common processing origin.

Ground-based light curves of TOI 620 from transient and transit searches do not have sufficient photometric precision to detect the ~0.2% quasi-sinusoidal photometric variations seen in the TESS light curve (Section 6.1.2). Time series of the activity indicators (Hα, Na D, and CRX) extracted from the CARMENES, MAROON-X, and NEID spectra do not contain significant periodicity.

An analysis of the TiO lines in the TRES spectra described in Section 3.1 limits the rotational broadening $v \sin i$ to <3 km s^{-1}. With the assumption that the rotation axis is close to the plane of the sky (which holds if the orbit of the transiting planet is aligned with the stellar rotation), this is marginally consistent with a rotation period of 8.93 days but not 4.45 days. The signal could conceivably arise from an unresolved low-luminosity companion suggested by the Gaia astrometric error (see Section 3.7); both ultracool dwarfs and white dwarfs typically rotate much faster than ~9 days (Scholz et al. 2018; Kawaler 2015). On the other hand, late-type ($>$M4) field M dwarfs exhibit a wide range of rotation periods of ~0.1–100 days (Newton et al. 2016). The most harmonious explanation is that the 8.9 day signal is either the rotation period of TOI
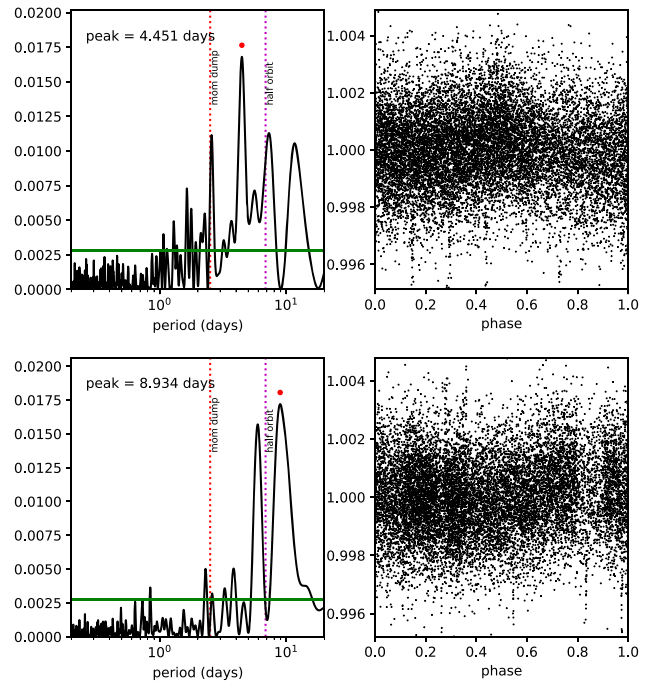

Figure 4. Lomb–Scargle periodograms (left panels) of TESS Sectors 8 (top) and 35 (bottom) photometry, showing peaks corresponding to plausible stellar rotation at 4.45 and 8.93 days, respectively. The horizontal green line is the power corresponding to a false alarm probability of 0.1%, and the vertical dotted lines mark the half-orbit and thruster firing (momentum dump) intervals of TESS where systematics are expected. The normalized light curves phased using these peak periods are shown in the right panels.

620, and that this reflects the influence of an (undetected) companion, or that it is the rotation of a late-type M-dwarf companion itself.

3.4. Stellar Activity and Age

Our stellar age posterior from EXOFASTv2, while appearing to imply an older star at $7.2^{+4.6}_{-4.7}$ Gyr, is not constraining, nor does it take into account the stellar rotation period analysis from the previous section. Since the star is on the main sequence, the broadband magnitudes, parallax, and galactic extinction values alone are not enough for us to provide a constrained age estimate. A rotation period of 8.93 days is intermediate between the T_{eff} rotation sequences of *single* M dwarfs in the 120 Myr old Pleiades and 670 Myr old Praesepe clusters (see Figure 7 in Curtis et al. 2020). Thus the TOI 620 system could be a mere few hundred million years old. However, binary stars tend to be more rapidly rotating than their single counterparts (e.g., Stauffer et al. 2018; Simonian et al. 2019) due to tides (for systems with separations $\ll 1$ au) or the rapid dissipation of primordial disks that would otherwise be a sink for angular momentum (for systems with separations $\lesssim 100$ au). Importantly, we find no corroborating evidence for a young age: an exhaustive comparison of the *UVW* space motions of the star with that of nearby open moving groups and clusters reveals no matches (Gagné & Faherty 2018; J. Gagné, private communication), nor are the values $(+8.5, +13.4, +6.5)$ km s^{-1} close to the local standard of rest (e.g, $(-8.6, -4.8, -7.3)$ km s^{-1}; Ding et al. 2019). The star shows no emission in Hα (Gaidos et al. 2014) nor is there emission in the core of the Na I D lines (Section 3.1). The star was not detected by ROSAT in 0.1–2.4 keV X-rays (Second
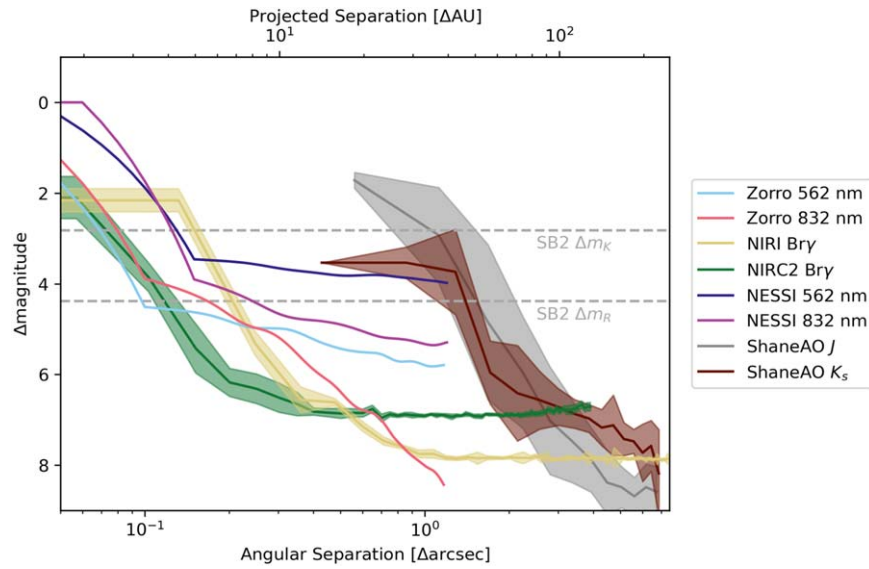
Figure 5. Plots of angular separation vs. the change in magnitude, Δm, from each of our high-contrast imaging observations. The width of the NIRI, NIRC2, and ShaneAO curves indicates the range of uncertainty for each curve. The 5σ sensitivity curves for NIRI and NIRC2 achieve excellent sensitivity to resolve stellar companions, and do not identify any such companions in the field of view.
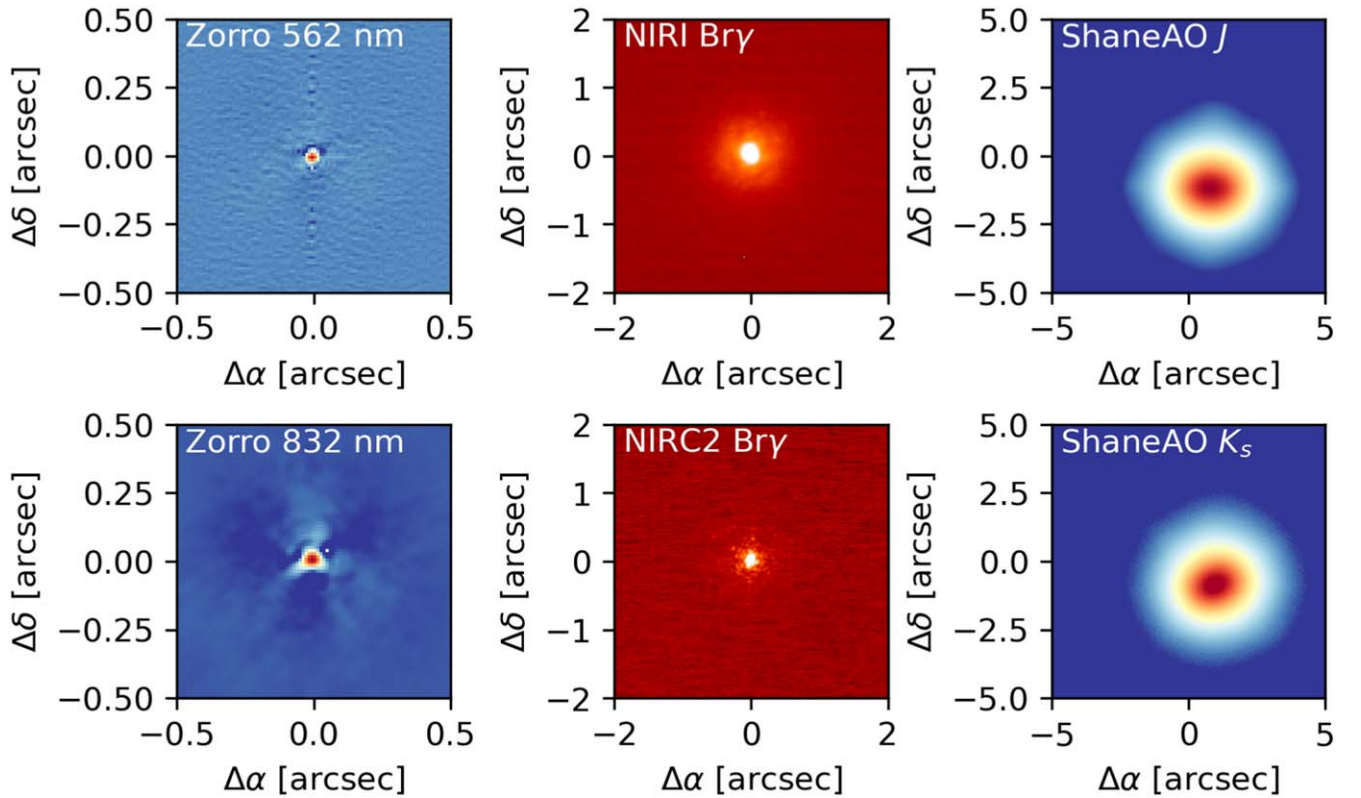

Figure 6. Reconstructed images from Zorro (top left: 562 nm, bottom left: 832 nm), NIRI (top middle), NIRC2 (bottom middle), and ShaneAO (top right: J, bottom right: K_s) which appear single to the limit of each instrument's resolution.

ROSAT All-sky Survey Source Catalog, Boller et al. 2016), the Galaxy Evolution Explorer in the far-UV (FUV; 1340–1806 Å) or near-UV (NUV; 1693–3006 Å) passbands, nor by APASS in the Sloan u' (3000–4000 Å) passband, as might be expected for a nearby rapidly rotating, magnetically active star with a bright chromosphere. The relatively short rotation period can then be interpreted as the result of potential binary interactions, or potentially the nature of an unseen companion, rather than youth of TOI 620 itself.

3.5. High-contrast Imaging

High-contrast imaging observations are key in allowing us to constrain the properties of the host star, particularly in studying whether or not there are any bound companion stars within $\sim0\rlap{.}{''}2$–$5''$ projected separation of the primary star.

Figure 5 shows the final contrast curves and Figure 6 shows the images for all of our high-contrast imaging observations included in this work, with each instrument and filter labeled

appropriately. For the Zorro 562 nm and 832 nm data, we find that TOI 620 is a single star with no companion brighter than 4.5 magnitudes at the diffraction limit (20 mas) and no companion brighter than 8.5 magnitudes at $1\rlap{.}''2$. At the distance of TOI 620 ($d = 33$ pc) these angular limits correspond to spatial limits of 0.7 to 40 au.

In the NIRC2 analysis, we searched for companions visually, and did not detect point sources anywhere in the field of view, which extends to $\sim 4''$ from the host star in all directions. To test the sensitivity of our observations, we injected fake companions throughout the image, and tested the flux at which these companions could be redetected at 5σ. We averaged the sensitivity over position angle to create the NIRC2 sensitivity curve included in Figure 5. We achieved excellent sensitivity to stellar companions even with this very short observing sequence, due to the good weather conditions and the brightness of the host star. Our NIRC2 observations are sensitive to companions 6.2 mag fainter than the host beyond 200 mas, and are sensitive to companions 6.8 mag fainter than the host in the background-limited regime, beyond $0\rlap{.}''5$.

Analysis of the NIRI contrast curve was performed in a similar fashion to the NIRC2 analysis described above. Analyzing the NESSI data, we detect no companions down to a magnitude difference $\Delta m \approx 4$ at $0\rlap{.}''2$ and $\Delta m \approx 5$ at $1''$. For the ShaneAO data, we computed the variance in flux in a series of concentric annuli centered on the target star in the combined image. The resulting 5σ contrast curves are shown in Figure 5.

3.6. Background Stars from Historical Imaging

TOI 620 is classified as a high-proper-motion star, with a $|\mu_\delta| > 350$ mas yr^{-1}. This means we can look back at historical images of the night sky around the TOI 620 system and see how the star has moved, so we can see whether there are any background stars that TOI 620 has approached and thus would have its light diluted with at the current epoch. A historical image of the TOI 620 system from the Digitized Sky Survey (DSS), in 1954, is shown in Figure 7, which shows that there are no background stars at the current coordinates of TOI 620, with the closest source being TIC 296739889 at $9\rlap{.}''2$, as mentioned in Section 3.4. There are also no Gaia EDR3 sources within $3°$ that have common proper motions to TOI 620, indicating that it does not have a wide binary companion down to the sensitivity of Gaia.

3.7. An Unresolved Companion?

Neither our AO imaging nor spectroscopy contain unambiguous evidence for a (sub)stellar companion; nevertheless, Gaia astrometry points to the existence of such an object. The reduced unit weighted error (RUWE), a measure of the goodness of fit of the astrometry to a single-star solution corrected for chromatic effects, is 1.395. RUWE values approaching 1.4 (where the average deviation squared is twice the error squared) have been empirically found to be highly correlated with stellar multiplicity (Belokurov et al. 2020, Kraus et al., in preparation). TOI 620 is free of the effects (extreme color or high variability) that might make such a RUWE value suspect, although some anomalous RUWE values can be due to instrumental effects. Instead, the astrometric error could also be produced by (i) the presence
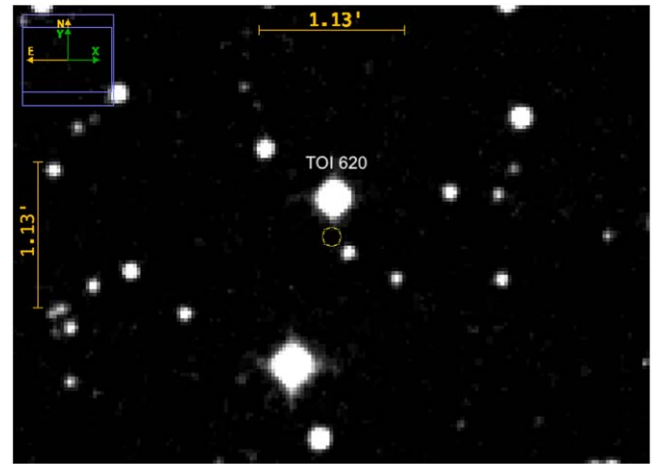

Figure 7. A historical Digitized Sky Survey (DSS) image of the TOI 620 system in 1954, in the DSS red band, where the current location of TOI 620 is circled in yellow. The diameter of the circle is $\approx 11''$, or $\sim$half the size of a TESS pixel. It is visibly clear that no stars would be in the background of TOI 620's current position. The star to the lower right of its current position is the aforementioned TIC 296739889 at a separation of $9\rlap{.}''2$, with a T-mag contrast of 7. Its close separation indicates its light would be blended with TOI 620's in the TESS aperture.

of a second unresolved source causing a shift in the apparent photocenter location along the Gaia scan track that depends on the angle between the binary axis and the scan direction (i.e., Ziegler et al. 2019); and/or (ii) motion of the system photocenter on the sky due to orbital motion. The former effect requires that the companion be luminous but does not require orbital motion, and will increase with angular separation up to a point ($\gtrsim 0\rlap{.}''7$) where the binary is resolved by Gaia. The latter effect also increases with angular separation but requires significant orbital motion (which decreases with semimajor axis) and will be most prominent at intermediate separations.

There will be a limited range of scenarios (i.e., companion mass or luminosity and semimajor axis or separation) that can produce the astrometric error but are compatible with our AO and RV observations (e.g., Wood et al. 2021). We performed Monte Carlo simulations combined with analytical predictions of Gaia astrometric deviation (Gaidos et al., in preparation). For the asymmetry effect we assumed that the 43 scans used in EDR3 for TOI 620.01 were distributed uniformly with angle on the sky, and axisymmetric Gaussian point-spread functions (PSFs) with a FWHM of $0\rlap{.}''1074$ (Rowell et al. 2021). Gaia is assumed to resolve sources with separations greater than $0.7 + 0.15\Delta G$ arcsec (Brandeker & Cataldi 2019). Figure 8 shows the mean photocenter deviation in milliarcseconds as a function of ρ and ΔG. The mean centroid error we approximate as $0.53\sigma_\varpi \sqrt{N}$, where σ_ϖ is the error in parallax and N is the number of scans used in the astrometric fit (Belokurov et al. 2020). For TOI 620 b the mean centroid error is 0.297 mas, and the region of parameter space where the expected deviation exceeds this value (and hence RUWE is $\gtrsim 1.4$) is shaded in red. The 5σ contrast ratio detection limits for our NIRC2 and NIRI AO imaging, converted from ΔK (or Br γ) to ΔG using absolute photometry of a set of M dwarfs (Mann et al. 2015, 2019), are also plotted. Most of the region that would explain a high RUWE in this manner is ruled out by these data. (The remaining sliver at small separation is also ruled out by our RV measurements; see below.) Thus, apparent photocenter
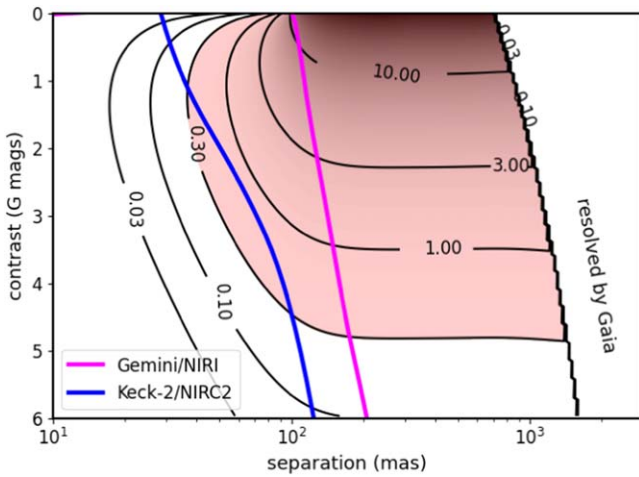
Figure 8. rms Gaia photocenter shift, in units of milliarcseconds, expected for an unresolved binary with a given separation and Gaia contrast ratio that produce an asymmetric point-spread function. The per-observation centroid measurement error for TOI 620 is 0.3 mas and the photocenter rms would exceed this (and RUWE would be $\gtrsim 1.4$) in the red shaded region. The blue and magenta curves are the 5σ detection contrast ratio limits on any companion from our Keck II/NIRC2 and Gemini-N/NIRI AO imaging.

motion due to an asymmetric PSF is unlikely to explain the high RUWE value.

This leaves actual photocenter shift due to Keplerian orbital motion (in a binary system) as the explanation for the high RUWE. We again calculated the permitted range of parameters for this scenario, assuming a "subthermal" eccentricity distribution (uniform with the square root of the eccentricity), and a log-normal distribution of semimajor axis with a mean of log 5.3 au and a standard deviation of 0.87 dex (Duchêne & Kraus 2013). This is based on the observed distribution of stellar companions, but the distribution of giant planets also has a peak between 1 and 10 au (Nielsen et al. 2019; Fernandes et al. 2019; Meyer et al. 2018). We used isotropic distributions for inclination, mean anomaly, and argument of periapsis, and two mass distributions: a "brown-dwarf-rich" uniform distribution and a "brown-dwarf-poor" log-normal, the latter centered at 1 M_J with a standard deviation of 0.6 dex to reflect the mass distribution of giant planets found in RV surveys of exoplanets (Malhotra 2015) and an apparent "desert" in brown dwarfs close to stars, especially low-mass stars such as TOI 620 (Nielsen et al. 2019). We required that the mean rms photocenter motion equal or exceed centroid error, we imposed constraints from our AO imaging, and required the absolute radial acceleration to be <0.089 m s^{-1} day^{-1} (96% upper limit; Section 5.1).

The ranges of mass and semimajor axis that are permitted by these constraints occupy a narrow band running from a fractional mass of Jupiter at a few astronomical units to tens of Jupiter masses at 30 au; Figure 9 shows the results for the uniform and log-normal mass priors (left and right, respectively). A range of scenarios is clearly possible but either a Jupiter-mass companion at ~3 au, or an ultracool dwarf at 20–30 au are favored. More massive companions are permitted, but only under the unlikely scenario where the projected separation is much less than the true orbital separation, which we explore in the next section.

3.8. Spectroscopic Binary Analysis & Results

We next explore the possibility that TOI 620 possesses a low-mass spectroscopic stellar companion hidden at a small projected separation, much smaller than the true orbital separation, a relatively low-probability occurrence. TOI 620 shows no evidence for an equal-mass SB2 binary in any of our spectroscopic data, and our broadband SED analysis shows no indication for an overluminosity as is common for binaries; this limits any stellar companions to TOI 620 to mid- and late-M dwarfs with an unequal mass ratio (much lower than the primary mass).

The most favorable flux contrast ratio for a hypothetical mid- to late-M dwarf companion would be in the NIR. Consequently, we model our 10-times-iterated iSHELL stellar template (see Appendix A on how this iterated stellar template is generated) with a two-component spectroscopic binary model consisting of two BT-Settl models generated from the Spanish Virtual Observatory (SVO) website[54] (e.g., Kanodia et al. 2020), with an arbitrary RV offset between them. Our iSHELL stellar template is effectively an iterated and empirically deconvolved cumulative high S/N (>500) spectrum of our target star, comprised of a summation of all of the iSHELL observations in the stellar rest frame, after modeling out tellurics, the gas cell absorption, the blaze function, and other instrumental effects that are incoherent in the stellar rest frame when sampled across many solar system barycenter velocities. The iSHELL observations themselves cover a time baseline of <2 yr, shorter than putative orbital periods of any potential stellar companions (Section 5). As such, time-averaging of relative RV shifts between the stars is not an issue.

We correct the SVO wavelengths (which have a resolution of 10^{-3} Å) for the index of refraction of the atmosphere ($n_{\rm air} = 1.000293$) and use a piecewise cubic Hermite interpolating polynomial to interpolate the data with scipy. We assume the rotational velocities of each star are small enough to have minimal Doppler broadening effects and do not fit for them. We fit the temperature of each star and the RV of each star (for a total of four free parameters), and we use the tables from Pecaut & Mamajek (2013) to determine the difference in magnitudes at the K band from the best-fit temperatures and apply the flux ratios to our model. We linearly interpolate values in-between entries from Pecaut & Mamajek (2013). Our binary flux model can be summarized as

$$F(\lambda) = (1 - D)F_1(\lambda) + DF_2(\lambda), \qquad (1)$$

where $F(\lambda)$ is the total flux at wavelength λ, and $F_1(\lambda)$ and $F_2(\lambda)$ are the flux from the primary and secondary, respectively, with arbitrary RV offsets. D is the dilution, or the fraction of light from the secondary divided by the total light from the system.

We first perform a maximum-likelihood fit by minimizing the negative log of the likelihood, where our log-likelihood function is defined as

$$\ln \mathcal{L} = -\frac{1}{2}\sum_{i=1}^{N}\left(\frac{d(\lambda_i) - F(\lambda_i)}{\sigma_i}\right)^2 + \ln(2\pi\sigma_i^2), \qquad (2)$$

where the subscript i enumerates each wavelength data point up to N total, $d(\lambda_i)$ is the value of our 10 iteration deconvolved stellar template from pychell, and σ_i is the error in our

---

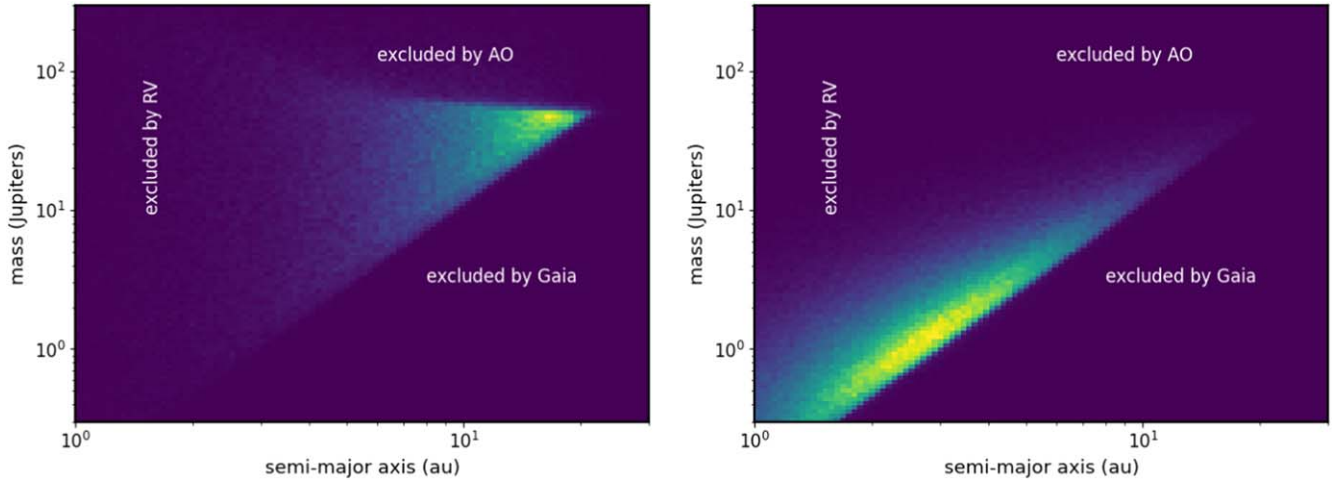[54] http://svo2.cab.inta-csic.es/theory/newov2/index.php

Figure 9. Limits on the separation and contrast ratio of a potential companion detected by Gaia (and RVs). The color map linearly represents the posterior probability of a companion in the separation–companion mass plane, as ascertained by Monte Carlo calculations. The left panel assumes a uniform prior on companion mass, while the right panel uses a log-normal prior centered on 1 Jupiter mass and with a standard deviation of 0.6 dex.
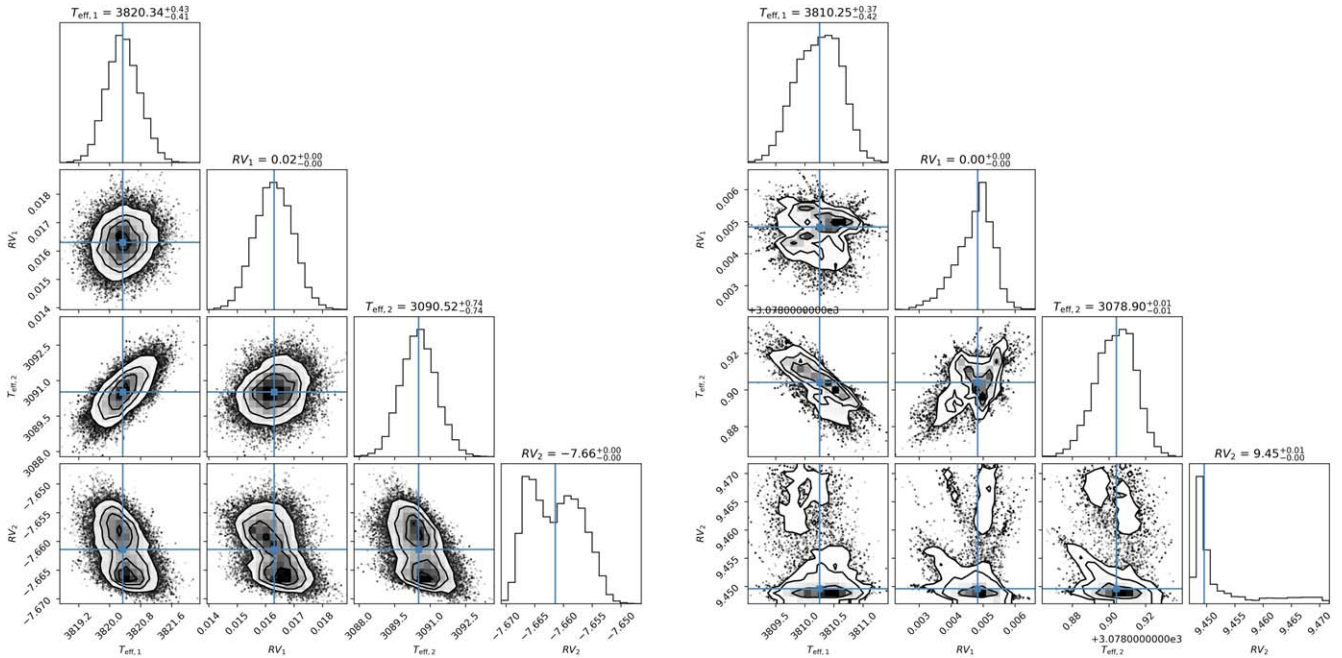

Figure 10. Markov Chain Monte Carlo corner plot of our spectral binary analysis of the iSHELL iteration 10 stellar template. Plots along the diagonal show one-dimensional histograms of the posterior distributions of each parameter. Off-diagonal plots show the covariance between each model parameter. The posterior distributions are bisected to show a zoom of each of the two individual posterior peaks on the left and right corner plots, showing that they are centralized maxima and are not edge solutions in our model parameter space.

observed and deconvolved stellar spectrum $d(\lambda_i)$ at wavelength λ_i for all iSHELL orders considered. We assume that $\sigma_i = 0.01$ is a constant across our spectrum, a conservative assumption given the cumulative S/N of our observations.

The maximum a posteriori values are then used as starting points for an MCMC simulation, where we impose a Gaussian prior on the T_{eff} of the primary corresponding to our posterior from EXOFASTv2, and we impose hard boundaries on the RVs between ±200 km s^{-1}. We run a series of MCMC simulations with differing upper boundaries on the T_{eff} of the secondary corresponding to flux ratios of $<50\%$, $<20\%$, $<15\%$, $<10\%$, and $<5\%$. We find in the $<50\%$ and $<20\%$ limiting-flux-ratio cases that the T_{eff} of the secondary hits the upper boundary in

T_{eff} with no relative RV offset, indicating that our spectra are best described by an equal-temperature binary, a scenario that is excluded by our SED and high-contrast imaging analysis. Since TOI 620 is not overluminous, and since we do not impose this constraint in this spectroscopic analysis, this effectively implies that the single-star solution is preferred for flux ratios of $>20\%$.

However, in the $<10\%$ and $<15\%$ flux-ratio-limited MCMC cases we find consistent and robust doubly peaked solutions that suggest the possibility of a HEB system scenario for TOI 620, in which two smaller stars are both orbiting each other and then the pair is orbiting the more massive primary star, in contrast to the companion analysis in Section 3.7. The corner
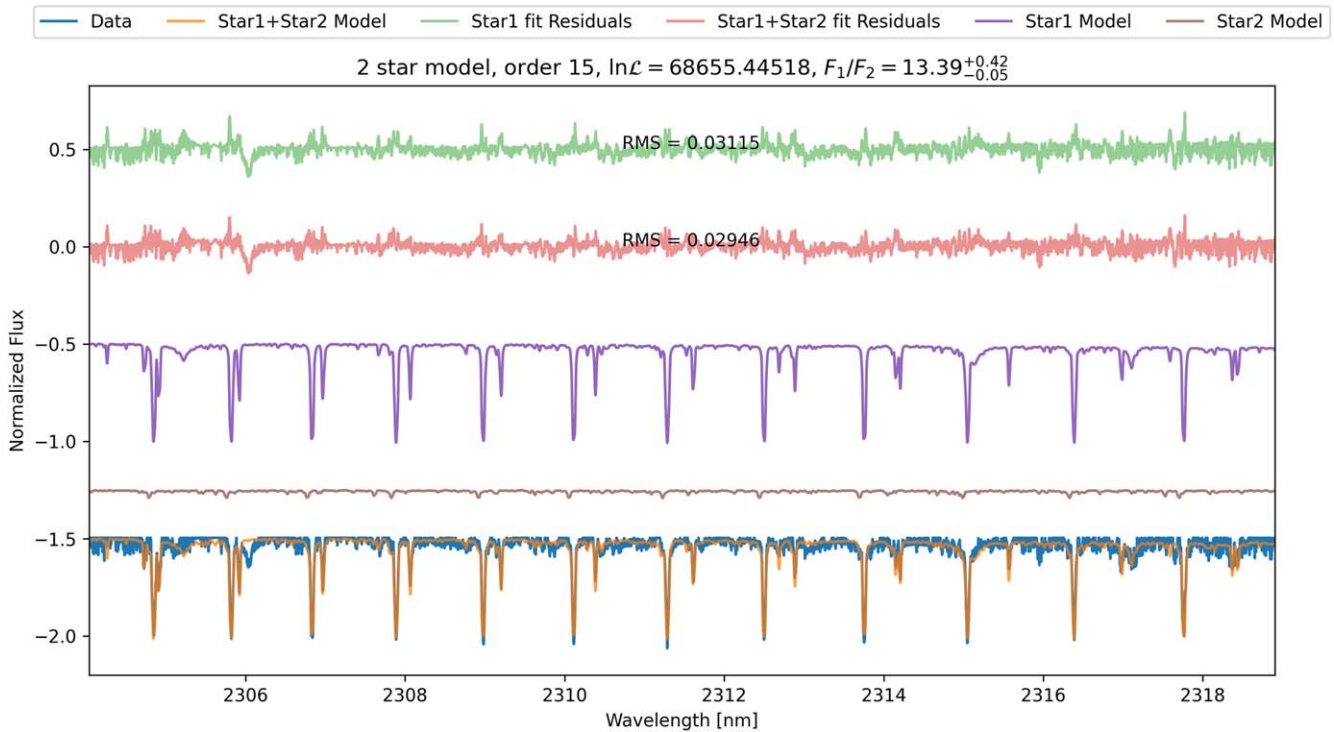
Figure 11. Fits of our spectral binary model of the iSHELL iteration 10 stellar template in the 10% flux-ratio-limited case. The blue line is the iteration 10 stellar template (see Section A), the orange line is the combined final flux model, the purple and brown lines are the individual fluxes from the primary and secondary, respectively, and the green and red lines are the residuals from the single-star and double-star fits, respectively, with rms displayed. The wavelength range shown corresponds to echelle order 15 on the iSHELL spectrograph. An example stellar spectral absorption line at 2306 nm that is missing from the BT-Settl models is readily apparent. Note, in the stellar rest frame, the telluric absorption feature residuals from all of our 379 iSHELL spectra sampled at a range of barycenter velocities are decoherent and not contributing significantly to the observed residuals.

plot of our <10% flux-ratio scenario is shown in Figure 10 with each peak in the posteriors separated and plotted individually. The doubly peaked posteriors are not confined by the prior bounds on the flux ratio. Finally, for the <5% flux-ratio-limited MCMC scenario, we again recover a maximum posterior probability at the upper limit to the flux-ratio range explored, indicating that a robust two-star model is only favored for flux ratios in the 10%–20% range. We do not explore a three-star model.

We show the two-star spectral fit of iSHELL's echelle order 15 (λ 2304–2320 nm; $m = 226$), which is relatively free of macrotellurics compared to other K-band orders, in Figure 11 (Plavchan et al. 2013b), with an rms ∼0.03. Given the S/N >500 of our empirical, deconvolved stellar spectrum, a residual rms $> 2 \times 10^{-3}$ is significant. However, the BT-Settl synthetic stellar models are incomplete in NIR-opacity sources for M-dwarf atmospheres, resulting in missing stellar absorption features and other systematics. Consequently, the residual rms of our best-fitting model is greater than the expected rms from the cumulative S/N of our observations. Our results are nonetheless compelling despite this model incompleteness, as systematics would not produce the isolated local maxima in the likelihood function that we observe, particularly when averaging over 13 iSHELL orders. While we show order 15 as a representative example, the MCMC modeling was performed jointly across orders 5–17 ($m = 216$–228) from our iSHELL data spanning a significant fraction of the K band. Performing a model comparison between this double-star model in the <20% flux-ratio regime and the best-fit single-star model, we find a $\Delta \ln \mathcal{L} = 68655.45$. From this, we compute the corresponding difference in the small-sample Akaike information criterion

(AICc; Akaike 1974; Burnham & Anderson 2002), ΔAICc = -137302.89. Since the value is negative, this indicates that the two-star model is favored over the one-star model, though the magnitude of how much it is favored is dependent on the spectroscopic flux error of 0.01 that we imposed earlier.

From this analysis, we conclude that the iSHELL data indicates the possible presence of one or two low-mass stellar companions with a K-band flux ratio of $13.39^{+0.42}_{-0.05}$, $T_{\rm eff1} = 3090$ K and $T_{\rm eff2} = 3079$ K, and RVs relative to the primary of -7.66 and $+9.45$ km s^{-1}, respectively. The RV separation of ∼17 km s^{-1} is approximately consistent with a Keplerian orbital velocity for the orbital period of the candidate exoplanet (if it were instead an HEB), and slightly offset from the velocity of the primary by a reasonable ∼1 km s^{-1}.

Alternatively, we do not exclude and do not explore in this analysis that this favored SB2 solution could be an artifact of not rotationally broadening our stellar models, which could also potentially yield a false symmetric set of binary companions. Nonetheless, motivated by the Gaia RUWE statistic and this SB2 analysis of our iSHELL spectra, we must carefully consider and explore the possibility that TOI 620 is a circum-secondary planet or HEB false positive in more detail.

For this K-band flux ratio, and the corresponding R-band flux ratio for M dwarfs of these temperatures of ∼57, they would have been detected by the high-contrast imaging in Section 3.5 for projected separations >0″.2; additionally, given the iSHELL slit width of 0″.375 and typical seeing conditions of less than 1 arcsecond, the projected separation must also be less than 1 arcsecond. However, no such companions are detected. Thus, if these stellar companions exist, they must possess a

projected separation of $<0\rlap{.}{''}2$ or <6.6 au, and deeper high-contrast NIR imaging or aperture mask photometry will be required in the future to exclude this possibility. Given the visible flux contrast ratio, any such companions would easily be hidden in the high-resolution spectroscopic data. However, such a false-positive circum-secondary or HEB scenario could be uncovered from chromatic transit photometry. We next turn to our transit analysis to explore the analysis of the primary star transit and these possible false-positive scenarios.

4. Transit Analysis & Results

It is clear from the Gaia RUWE statistic and spectroscopic binary analysis, in conflict with the high-contrast imaging, that there are three distinct possibilities for the source of the transit signal, but from these results alone it is difficult to determine whether we have a single system with a circum-primary planet, a double with a circum-secondary planet, or even triple hierarchical system with an eclipsing binary pair. Motivated by this quandary, we present results from three separate analyses of the TOI 620 light curves in EXOFASTv2 under the assumptions of a circum-primary planet (Section 4.2), circum-secondary planet (Section 4.3), and HEB star system (Section 4.4) to determine which, if any, of these scenarios is the most plausible given the data. To gain additional insight, we first perform traditional vetting analysis in Section 4.1 to see if any of the usual oddities that would indicate an eclipsing binary or other false positive appear in the light curve.

4.1. Vetting Against False Positives

The first of our vetting tests was performed with the Discovery and Vetting of Exoplanets (DAVE) vetting pipeline (Kostov et al. 2019), which shows no significant odd–even differences between consecutive transits (confirming the measured period is not an integer multiple of the true period), no significant photocenter motion during the transits (confirming the target is the source of the transits), and no significant secondary eclipses. Phased transit data and photocenter plots are provided in Appendix B. We confirm these results with the EDI-Vetter Unplugged tool (Zink et al. 2020),[55] which checks for a similar suite of eclipsing binary indicators, and found no evidence pointing to a false-positive scenario.

We additionally perform a false-positive probability (FPP) analysis with vespa (Morton 2012), which uses galactic population statistics for stellar multiplicity, transit depth, duration, and ingress/egress duration to calculate the probability that the target is an eclipsing binary, blended eclipsing binary, HEB, or planet. Using the TESS transit data, this gives a FPP of 1 in 22179. The priors, likelihoods, and probabilities are shown in the Appendix along with TOI 620's location in $\log\delta$–T–T/τ space compared to typical planet populations.

4.2. True-positive Scenario

We next performed an analysis with the signal generated by a planet orbiting the known star. After normalizing the TESS PDC-SAP data as described in Section 2, we jointly model the TESS and all ground-based light-curve follow-up observations with EXOFASTv2. Our minimal priors are detailed in Table 5, including the period, P, time of conjunction, T_C, and radius ratio, R_p/R_*.

Table 5
Prior Probability Distributions for Our EXOFASTv2 MCMC Simulations

Parameter (units)	Initial Value (P_0)	Priors	Prior Citation
P (days)	5.098831	$\mathcal{U}(P_0 \pm 10\%)$	E19
T_C (days)	8518.005713	$\mathcal{U}(P_0 \pm P/3)$	E19
R_p/R_*	0.053	$\cdots$	This work

Note. $\mathcal{N}(\mu, \sigma)$ signifies a Gaussian prior with mean μ and standard deviation σ. $\mathcal{U}(\ell, r)$ signifies a uniform prior with left bound ℓ and right bound r. Parameters that are missing, including e, ω, etc., are initialized to circular and edge-on values, with no imposed priors. Also note that the time of conjunction, T_C, has been subtracted by 2,450,000. References: E19: Eastman et al. (2019).

The posterior values for this initial MCMC run are then used as the initial values for a second iteration run (though we keep the same uniform and Gaussian priors as the initial run) that we allow to run longer, and we confirm the second MCMC converges on the same results within 1σ to check for the robustness of the MCMC posteriors. Each MCMC is run for 225,000 steps, and we measure convergence by ensuring the maximum Gelman–Rubin statistic of the chains is $\lesssim 1.1$ (Gelman & Rubin 1992) at the end of the simulation. The transit models of the MCMC simulation are shown in Figure 12, while the SED model is in Figure 3. A corner plot showing a subset of the most interesting posteriors is presented in Figure 13. The median posterior values and 68% confidence interval 1σ Gaussian equivalent uncertainties are shown in Table 6.

We also perform a separate study of the MuSCAT2 data specifically, due to its simultaneous observations in the g', i', r', and z' bands, to search for a possible chromatic variation of transit depth, and put constraints on any resulting contamination from a companion in the circum-primary scenario. The study is done using PyTransit (Parviainen 2015) and follows the multicolor candidate validation approach described in Parviainen et al. (2019) and Parviainen et al. (2020). With the assumption that TOI 620 b is a circum-primary planet, we look at what constraints can be placed on a secondary star present in the system. We are able to rule out any significant contamination of $>20\%$ in flux from companions of different spectral types, whereas stars of similar spectral type to the host star are limited to brightness ratios $<40\%$ relative to the host star. The former is consistent with our SB2 analysis in Section 3.8 (and does not exclude the potential companions identified therein), and the latter is further constrained by our SED analysis in Section 3.2 since there is no significant overluminosity of the primary. In Figure 14, we show posteriors and covariances for a set of model parameters (effective temperature of the host and contaminant stars, impact parameter, and host stellar density) against the "true" planet-to-star radius ratio, and the flux contamination ratio from the secondary star. We also show the effective planet radius, after correcting for the flux contamination from a secondary, as a function of the flux contamination; the planet remains roughly Neptune-sized, even in the presence of up to 40% flux contamination from a secondary. As a caveat to our analysis, the radius value and uncertainty presented in Table 6 do not account for any inflation from a potential flux contaminant, since we only considered a single-star host in this model.
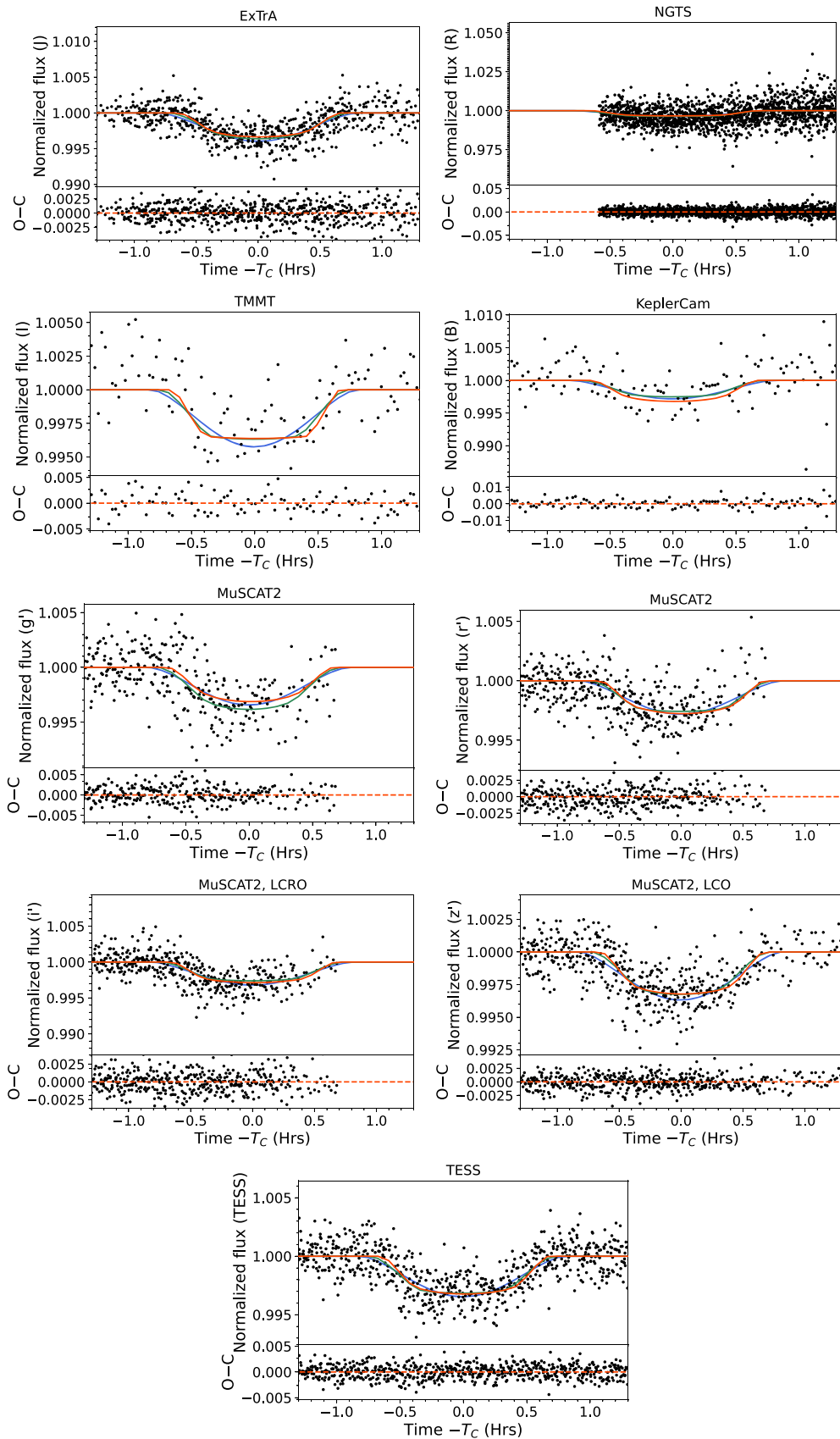
Figure 12. Transit data and models for each filter used in the `EXOFASTv2` analysis of TOI 620. Filters shown, from top left to bottom right, are *J, R, I, B, g', r', i', z',* and TESS. In each filter's plot, the top plot shows the combined transit data from all observations in that filter, phased to the period of the planet (5.09887 days), with each line showing the median transit model for the circum-primary (red), circum-secondary (green), and hierarchical eclipsing binary (HEB, blue) cases. The dilutions in the circum-secondary and HEB scenarios were allowed to independently vary in each bandpass and converge on unphysical values, as shown in Figure 15. The bottom plots show the residuals for the circum-primary model only.
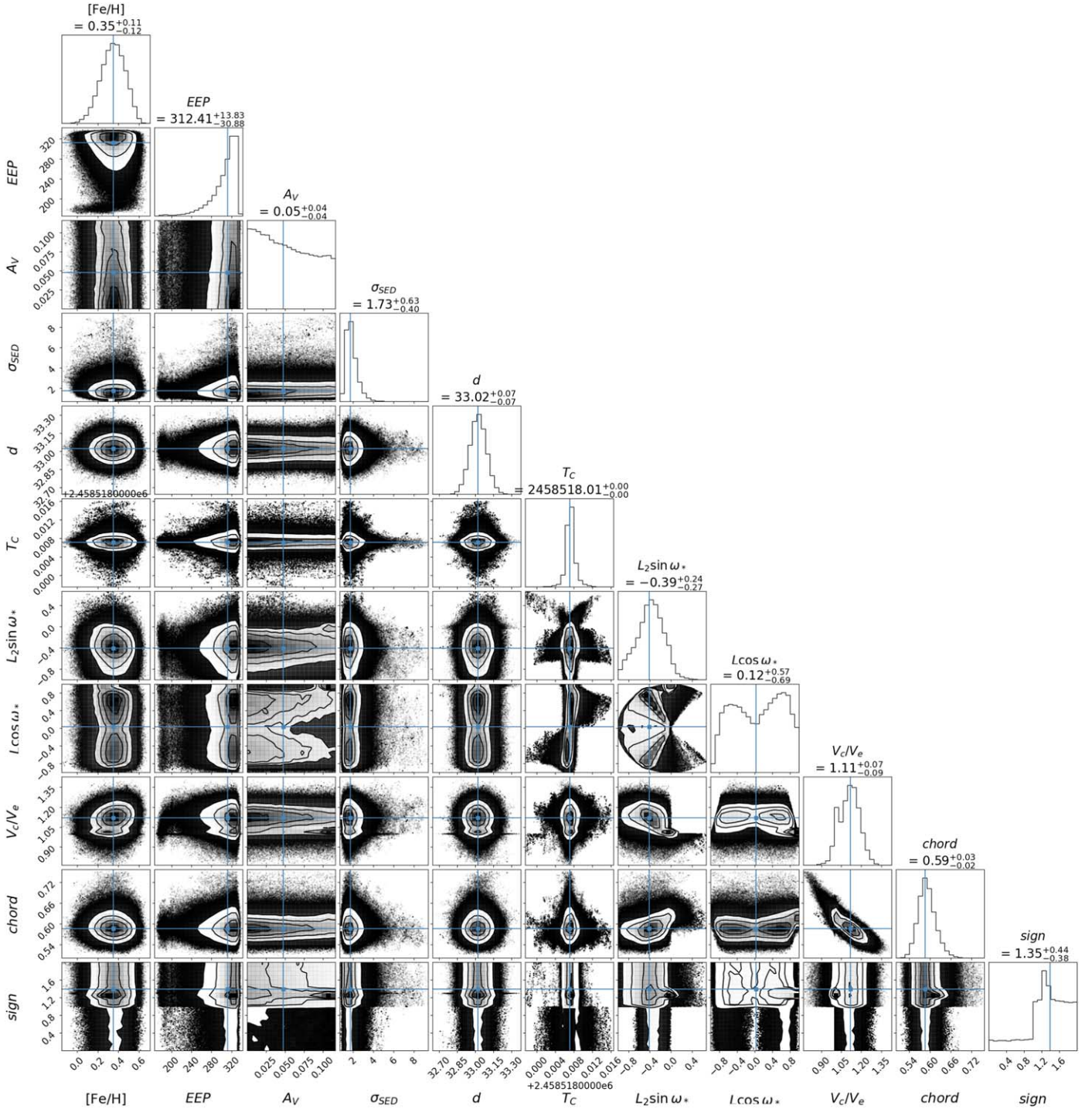
Figure 13. Markov Chain Monte Carlo (MCMC) corner plot of our joint ground and space-based transit model MCMC for TOI 620. Plots along the diagonal show one-dimensional histograms of the posterior distributions of each parameter. Off-diagonal plots show the covariance between each model parameter. Note that chord $= \sqrt{(1 - R_P/R_*)^2 - b^2}$ and $L_2 = \text{sign}(V_c/V_e - 1)L$ (see Eastman et al. 2019). Not all model parameters that were varied are shown in this corner plot. Namely, we do not show the detrending parameters of each data set, linear and quadratic limb-darkening coefficients from each wavelength band, R_*, $R_{*,\text{SED}}$, T_{eff}, $T_{\text{eff, SED}}$, $[\text{Fe/H}]_0$, $\log M_*/M_\odot$, M_P, R_P/R_*, and $\log P$. The posteriors not shown are well behaved, and there is no strong covariance between any of them except the linear and quadratic limb-darkening coefficients, which show anticorrelation, and the metallicity and initial metallicity, which show strong correlation. All MCMC corner plots presented in this paper are generated using `corner.py` (Foreman-Mackey 2016).

4.3. Circum-secondary Scenario

We now model the transit data under the assumption of a circum-secondary transiting planet, using posteriors from our iSHELL SB2 analysis as priors for the star and dilution terms in EXOFASTv2. The dilution priors for each filter are made under

the approximations that TESS $\approx I \approx i'$, $R \approx r'$, and $B \approx g'$, and we set lower bounds on the dilution to prevent them from being driven to zero and recovering the circum-primary solution. We exclude SED modeling with EXOFASTv2 since the broadband apparent magnitudes will be dominated by the flux from the

Table 6
Planetary Parameters: Median Values and 68% Confidence Interval for TOI 620

Parameter	Units	Values
Planetary Parameters:		b
P…	Period (days)…	$5.0988179^{+0.0000045}_{-0.0000046}$
R_P…	Radius ($R_\oplus$)…	3.76 ± 0.15
M_P…	Predicted mass[a] ($M_\oplus$)…	$15.4^{+5.5}_{-3.6}$
T_C…	Time of conjunction[b] (BJD$_{TDB}$)…	$2458518.00718^{+0.00093}_{-0.00083}$
T_T…	Time of minimum projected separation[c] (BJD$_{TDB}$)…	$2458518.00717^{+0.00050}_{-0.00051}$
T_0…	Optimal conjunction Time[d] (BJD$_{TDB}$)…	$2458992.19724^{+0.00078}_{-0.00069}$
a…	Semimajor axis (au)…	$0.04825^{+0.00065}_{-0.00066}$
i…	Inclination (Degrees)…	$87.47^{+0.18}_{-0.30}$
e…	Eccentricity…	$0.22^{+0.28}_{-0.12}$
ω_*…	Argument of periastron (Degrees)…	-84^{+54}_{-64}
T_{eq}…	Equilibrium temperature[e] (K)…	$603.6^{+5.5}_{-5.3}$
τ_{circ}…	Tidal circularization timescale (Gyr)…	14^{+12}_{-13}
K…	RV semiamplitude[a] (m/s)…	$8.9^{+3.6}_{-2.2}$
R_P/R_*…	Radius of planet in stellar radii…	0.0627 ± 0.0017
a/R_*…	Semimajor axis in stellar radii…	$18.87^{+0.52}_{-0.51}$
δ…	$(R_P/R_*)^2$…	$0.00393^{+0.00021}_{-0.00020}$
δ_B…	Transit depth in B (fraction)…	$0.00257^{+0.00096}_{-0.0022}$
δ_I…	Transit depth in I (fraction)…	$0.00346^{+0.00036}_{-0.00065}$
δ_J…	Transit depth in J (fraction)…	$0.00357^{+0.00029}_{-0.00043}$
δ_R…	Transit depth in R (fraction)…	$0.00328^{+0.00047}_{-0.00098}$
$\delta_{g'}$…	Transit depth in g' (fraction)…	$0.00293^{+0.00073}_{-0.0017}$
$\delta_{i'}$…	Transit depth in i' (fraction)…	$0.0010^{+0.0015}_{-0.0022}$
$\delta_{r'}$…	Transit depth in r' (fraction)…	$-0.0003^{+0.0019}_{-0.0027}$
$\delta_{z'}$…	Transit depth in z' (fraction)…	$0.00295^{+0.00060}_{-0.0010}$
δ_{TESS}…	Transit depth in TESS (fraction)…	$0.00255^{+0.00075}_{-0.0011}$
τ…	Ingress/egress transit duration (days)…	0.0137 ± 0.0019
T_{14}…	Total transit duration (days)…	$0.0565^{+0.0013}_{-0.0015}$
T_{FWHM}…	FWHM transit duration (days)…	$0.0428^{+0.0013}_{-0.0015}$
b…	Transit impact parameter…	$0.887^{+0.014}_{-0.017}$
b_S…	Eclipse impact parameter…	$0.66^{+0.11}_{-0.13}$
τ_S…	Ingress/egress eclipse duration (days)…	$0.0061^{+0.0018}_{-0.0017}$
$T_{S,14}$…	Total eclipse duration (days)…	$0.0590^{+0.0021}_{-0.0062}$
$T_{S,FWHM}$…	FWHM eclipse duration (days)…	$0.0527^{+0.0021}_{-0.0066}$
$\delta_{S,2.5\mu m}$…	Blackbody eclipse depth at 2.5 μm (ppm)…	$1.058^{+0.10}_{-0.095}$
$\delta_{S,5.0\mu m}$…	Blackbody eclipse depth at 5.0 μm (ppm)…	$39.6^{+2.7}_{-2.5}$
$\delta_{S,7.5\mu m}$…	Blackbody eclipse depth at 7.5 μm (ppm)…	$115.8^{+7.1}_{-6.7}$
ρ_P…	Density[a] (cgs)…	$1.59^{+0.57}_{-0.36}$
$\log g_P$…	Surface gravity[a]…	$3.03^{+0.13}_{-0.11}$
Θ…	Safronov number…	$0.0242^{+0.0085}_{-0.0054}$
$\langle F \rangle$…	Incident flux (10^9 erg s^{-1} cm^{-2})…	$0.0283^{+0.0018}_{-0.0047}$
T_P…	Time of periastron (BJD$_{TDB}$)…	$2458516.5^{+2.2}_{-1.6}$
T_S…	Time of eclipse (BJD$_{TDB}$)…	$2458515.47^{+0.98}_{-0.87}$
T_A…	Time of ascending node (BJD$_{TDB}$)…	$2458516.62^{+0.51}_{-0.62}$
T_D…	Time of descending node (BJD$_{TDB}$)…	$2458519.41^{+0.68}_{-0.47}$
V_c/V_e…	…	$1.120^{+0.066}_{-0.073}$
$((1-R_P/R_*)^2-b^2)^{1/2}$…	…	$0.586^{+0.023}_{-0.021}$
$sign$…	…	$1.39^{+0.42}_{-0.51}$
$e\cos\omega_*$…	…	$0.00^{+0.30}_{-0.27}$
$e\sin\omega_*$…	…	$-0.147^{+0.081}_{-0.11}$
$M_P \sin i$…	Minimum mass[a] ($M_\oplus$)…	$15.4^{+5.5}_{-3.6}$
M_P/M_*…	Mass ratio[a]…	$0.000080^{+0.000029}_{-0.000019}$
d/R_*…	Separation at mid transit…	$20.0^{+1.7}_{-2.3}$
P_T…	A priori nongrazing transit prob…	$0.0468^{+0.0060}_{-0.0037}$
$P_{T,G}$…	A priori transit prob…	$0.0530^{+0.0068}_{-0.0041}$
P_S…	A priori nongrazing eclipse prob…	$0.0599^{+0.022}_{-0.0056}$
$P_{S,G}$…	A priori eclipse prob…	$0.0680^{+0.025}_{-0.0065}$
Wavelength Parameters:		B

Parameter	Units	Values
u_1…	Linear limb-darkening coeff…	$0.68^{+0.47}_{-0.44}$
u_2…	Quadratic limb-darkening coeff…	$0.04^{+0.48}_{-0.44}$
Transit Parameters:		TESS UT 2019-02-03 (TESS)
σ^2…	Added variance…	$-0.00000039^{+0.00000012}_{-0.00000011}$
F_0…	Baseline flux…	0.999887 ± 0.000063
C_0…	Additive detrending coeff…	…
M_0…	Multiplicative detrending coeff…	…
M_1…	Multiplicative detrending coeff…	…

Notes. Created using EXOFASTv2, commit number 7971a947. See Table 3 in Eastman et al. (2019) for a detailed description of all parameters.
[a] Uses measured radius and estimated mass from Chen & Kipping (2016).
[b] Time of conjunction is commonly reported as the "transit time"

[c] Time of minimum projected separation is a more correct "transit time"

[d] Optimal time of conjunction minimizes the covariance between T_C and period.
[e] Assumes no albedo and perfect redistribution.

primary. Qualitatively, the dilution of the secondary by the primary is greater at bluer wavelengths due to their relative effective temperatures and photometric colors expected from Pecaut & Mamajek (2013); the net result would be a shallower transit in the blue than in the red. However, we find our converged median MCMC dilution posteriors to be relatively flat, and thus inconsistent with the expected dilution curve for a cooler mid-M dwarf secondary, as shown in Figure 15. By rerunning the MCMC with the dilution parameters fixed at their priors, we recover transit depths that are inconsistent with the data, most notably in the B band (Appendix C). The priors, posteriors, and transit times are listed in Appendix C.1, along with an additional analysis of the MuSCAT data.

4.4. Hierarchical Eclipsing Binary Scenario

We next model the transit data under the assumption of an HEB scenario, deriving our priors in the same way as the circum-secondary analysis. This scenario comes with the added complication of not knowing whether we observe both primary and secondary eclipses, meaning the true period could be 5.09881 days or twice that, at 10.19762 days. As such, we create three models corresponding to (1) the 5.09 day period, seeing only even or odd transits, (2) the 10.20 day period's even transits, and (3) the 10.20 day period's odd transits. Our posteriors only converge in case 1, indicating we can rule out the 10.20 day period. We still expect the dilution posteriors to be shallower in the blue compared to the red, but again we find that our median MCMC dilution posteriors are flat and inconsistent with our expectations, as in Figure 15. By rerunning the MCMC with the dilution parameters fixed at their priors, we again recover transit depths that are inconsistent with the data (Appendix D). The priors, posteriors, and transit times are listed in Appendix D.1. We also perform a model comparison test by calculating the $\ln \mathcal{L}$, AICc, and Bayesian information criterion (BIC) for the circum-primary, circum-secondary, and HEB models in Table 7, which shows all models other than the circum-primary are ruled out to relative probabilities (compared to the circum-primary model) of $P_{\rm rel} = \exp(-\Delta \text{AICc}/2) \leqslant 3.41 \times 10^{-7}$.

5. Radial Velocity Analysis & Results

In this section, we present RV data analysis and results. Similarly to the transit analysis, we present results from three separate analyses of the TOI 620 RV data, assuming the planet is circum-primary (Section 5.1), circum-secondary (Section C.2), or an HEB (Section D.2), the latter two of which are detailed in the Appendix and summarized in Section 6.

5.1. Keplerian Radial Velocity Analyses & Results

Each planet is modeled in pychell (Cale et al. 2019) with a standard basis set of five orbital parameters: the period P, time of conjunction T_C, eccentricity e, argument of periastron ω, and RV semiamplitude K, with subscripts denoting the planet each parameter is associated with (in this case, planet b and a candidate c). We also include for each instrument an absolute RV offset term (γ), and a jitter term (σ) which quantifies RV white noise not accounted for by any modeled planet(s), stellar activity, or underestimated RV precision systematics. The $\dot{\gamma}$ term models a linear trend in the RVs over the entire baseline of observations and is indicative of a very-long-period companion for which we have only captured a small portion of the orbit's phase, so it can be approximated as a line; we do not find evidence for a jerk $\ddot{\gamma}$ and exclude it from our model. From our EXOFASTv2 analysis, we found $P_b = 5.0988179^{+0.0000045}_{-0.0000046}$ and $T_C = 2458518.00718^{+0.00093}_{-0.00083}$, both of which have uncertainties which are orders of magnitude finer than we can hope to resolve with the precision, sampling, and time baseline of our RV measurements. We thus fix both RV model parameters at these transit posterior values for all RV analyses in this paper to reduce the model parameter space. We exclude consideration of high-eccentricity $e > 0.5$ orbital solutions, and we find no compelling evidence in our RV measurements obtained to date to support such a high eccentricity. We first present the analysis assuming a circum-primary planet, mirroring our analysis of the light curves in Section 4.

The single-planet and linear-trend RV model, shown in Table 8, yields no recovery of the RV semiamplitude for the transiting b planet, and the maximum a posteriori (MAP) value drops to 0. The expected mass and RV semiamplitude provided
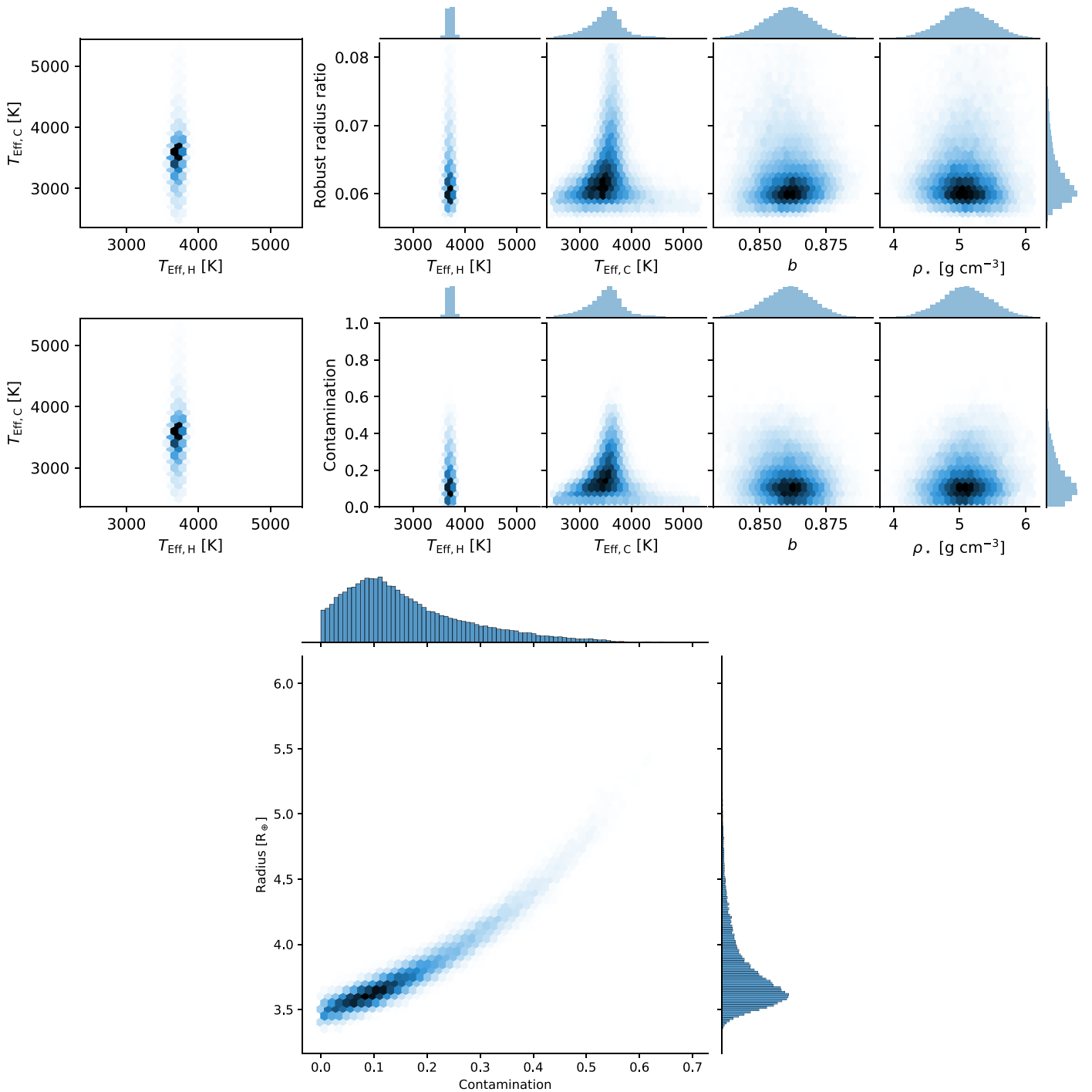
Figure 14. One-dimensional model parameter posterior histograms and model parameter covariances for $T_{\rm eff}$ of the host [H], $T_{\rm eff}$ of the contaminant [C], impact parameter, and host stellar density against the planet-to-star radius ratio (top) and flux contamination (middle) from a secondary star. Bottom: the corrected or "true" exoplanet radius as a function of the flux contamination from a secondary.

by the `EXOFASTv2` fit of the transit data (using the Chen & Kipping 2016 mass–radius relationship) were 15.4 $M_\oplus$ and 8.9 m s^{-1}, respectively, which we can robustly exclude.[56] The MCMC chains (excluding γ offsets and σ jitter model parameter terms) are shown in Figure 16. The corner plot shows in particular the well-behaved posterior of $\dot{\gamma}$ at 0.08 ± 0.01 m s^{-1} day^{-1} and the nondetection on K_b. We get

very similar results by assuming circular orbits. The RV models with MCMC median values are shown with our RV measurements phased to the period of b in Figure 17, while in Figure 18 they are unphased.

A model comparison with and without planet b is shown in Table 9, and shows that our most favored model is that with no planets (e.g., a nondetection of the transiting planet). To confirm that there is not a single data set in use that is diminishing our recovery of TOI 620 b, we run five separate fits, ignoring the $\dot{\gamma}$ term and the iSHELL data, and in each fit

---

[56] This is supported by checking with the predicted values from MRExo (Kanodia et al. 2019).
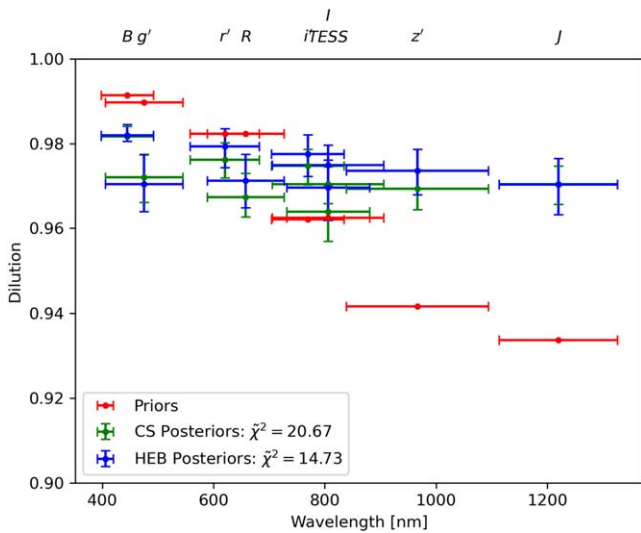
Figure 15. Our Markov Chain Monte Carlo dilution priors (red) vs. posteriors of the secondary for the circum-secondary model (green) and the hierarchical eclipsing binary (HEB, blue) model. We see a prior distribution that decreases with wavelength as expected for flux contamination from a hotter primary star, whereas the posteriors are mostly flat and become inconsistent at short and long wavelengths.

Table 7
A Model Comparison Test between the Transiting Circum-primary, Circum-secondary, and HEB Models

Model	$\ln \mathcal{L}$	ΔAICc	ΔBIC	N free
Circum-primary	45015.895	0.000	0.000	157
Circum-secondary	45001.005	29.781	29.700	157
Circum-secondary (fixed)	44888.868	235.801	164.067	148
HEB	44961.968	107.856	107.782	157
HEB (fixed)	44854.627	304.282	232.555	148

Note. N free is the number of free model parameters, the vast majority of which are light curve and associated detrending parameter normalization constants for each ground-based data set. The models marked as "fixed" are the ones where the dilution terms are held fixed to their prior values.

we remove a single data set (other than iSHELL). The MAP and MCMC recovered K values are listed in Table 10 and show that there is not a single data set that is significantly diminishing the recovery compared to the others.

Finally, we calculate a 5σ upper limit to the mass of TOI 620 b of $M_P \leqslant 7.1\ M_\oplus$. Using the radius of planet b from the EXOFASTv2 analysis in Section 4.2, $R_p = 3.76 \pm 0.15\ R_\oplus$, we derive a 5σ upper limit to the density of TOI 620 b of $\rho_P \leqslant 0.74$ g cm^{-3}. Of the 149 confirmed exoplanets from the NASA exoplanet archive with radii between 3–5 $R_\oplus$ and with measurements for both a mass and radius, the average mass is $\approx 18.7\ M_\oplus$ and the minimum is $2.07\ M_\oplus$, putting our upper limit for TOI 620 b well below average and closer to the minimum. Thus we can conclude that TOI 620 b is a very-low-density planet (see Figure 24).

6. Discussion

In this section, we first cover whether we can be confident that we are constraining the Doppler amplitude of TOI 620 b in Section 6.1 by considering the origin of the transit signal, our
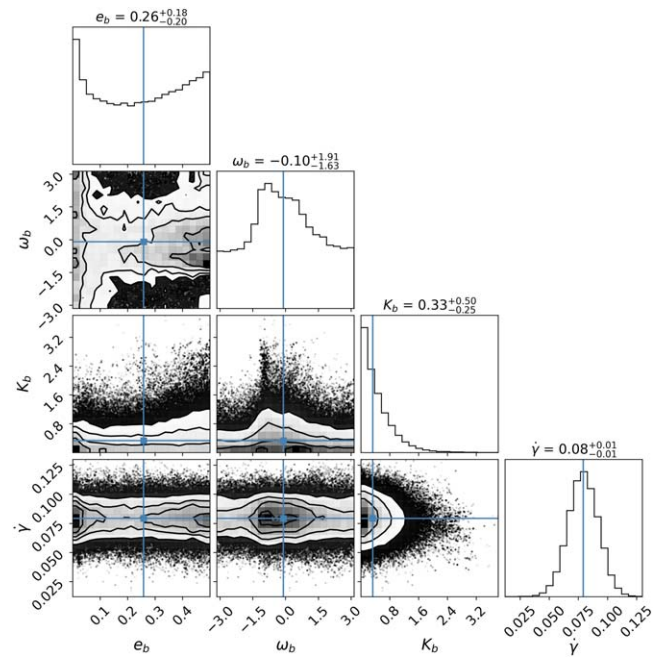

Figure 16. Markov Chain Monte Carlo corner plot of our eccentric ($e < 0.5$) TOI 620 b circum-primary model with all RV data points included, showing the posterior distributions of each model parameter that we allowed to vary. The gamma offsets and jitter terms are not shown, as they are all uncorrelated and to a good approximation are ideal Gaussian distributions. We obtain similar posteriors for K_b and $\dot{\gamma}$ for the assumption of a circular orbit.

RV noise, and systematics (including stellar activity and additional Keplerian RV signals). Then, in Section 6.2 we consider the evidence for and against the existence of additional massive companion(s) (whether stellar or not) to the primary TOI 620 host star. We summarize our findings on the age of TOI 620 in Section 6.3. Finally, in Section 6.4 we discuss the nature and implications of an abnormally low-density TOI 620 b on its composition, evolution, and potential for future observations.

6.1. Are We Actually Constraining the Doppler Amplitude of TOI 620 b?

The lack of recovery of a Doppler signal from TOI 620 b, despite seeing a clear transit signal, could be explained by one or more of the following. First, the transit signal could be associated with an unresolved fainter companion to TOI 620 with a flux too low to impart a significant Doppler signal on the combined flux from the system, e.g., a circum-secondary transiting object, or a HEB. Second, the Keplerian signal could be masked by an additional source of noise, e.g., either stellar "jitter" or apparent Doppler shifts produced by the combination of spectra from two dissimilar stars. Third, TOI 620 could host multiple planets that each impart significant Keplerian signals with different periods and which cannot be disentangled with the limited number of RVs obtained so far. Fourth, the planet could have a mass below our detection threshold. We discuss these possibilities in turn.

6.1.1. Excluding the Circum-secondary and Hierarchical Eclipsing Binary Scenarios with Chromatic Transit Light Curves

We rule out any nearby resolved stars as the source of the transit signal (Section 4.1) and, due to the high proper motion

Table 8
The Model Parameters and Prior Distributions used in Our RV Model that Considers the Transiting b Planet and the Linear $\dot{\gamma}$ Trend, as well as the Recovered MAP Fit and MCMC Posteriors

Parameter (units)	Initial Value (P_0)	Priors	MAP Value	MCMC Posterior
P_b (days)	5.09881	Fixed	...	...
$T_{C,b}$ (days)	2458518.007	Fixed	...	...
e_b	10^{-5}	$\mathcal{U}(0, 0.5)$	10^{-5}	$0.26^{+0.18}_{-0.20}$
ω_b	$\pi/2$	$\mathcal{U}(-\pi, \pi)$	$\pi/2$	$-0.10^{+1.91}_{-1.63}$
K_b (m s^{-1})	5	$\mathcal{U}(0, \infty)$	8.97×10^{-6}	$0.33^{+0.50}_{-0.25}$
γ_{iSHELL} (m s^{-1})	-8.448	$\mathcal{U}(P_0 \pm 100)$	-1.95	$3.83^{+3.08}_{-3.05}$
$\gamma_{\mathrm{CARMENES-Vis}}$ (m s^{-1})	-0.783	$\mathcal{U}(P_0 \pm 100)$	-0.78	$-1.60^{1.96}_{-2.00}$
$\gamma_{\mathrm{CARMENES-NIR}}$ (m s^{-1})	-1.510	$\mathcal{U}(P_0 \pm 100)$	-1.51	$-2.25^{+3.88}_{-3.76}$
γ_{NEID} (m s^{-1})	-1.525	$\mathcal{U}(P_0 \pm 100)$	-1.53	$-0.25^{+1.46}_{-1.50}$
$\gamma_{\mathrm{MAROON-X-blue}}$ (m s^{-1})	0.392	$\mathcal{U}(P_0 \pm 100)$	-3.89	$-5.89^{+1.33}_{-1.27}$
$\gamma_{\mathrm{MAROON-X-red}}$ (m s^{-1})	-1.769	$\mathcal{U}(P_0 \pm 100)$	-6.72	$-7.95^{+1.50}_{-1.53}$
σ_{iSHELL} (m s^{-1})	5	$\mathcal{N}(P_0, 2)$; $\mathcal{U}(10^{-5}, 100)$	13.42	$13.44^{+1.11}_{-1.07}$
$\sigma_{\mathrm{CARMENES-Vis}}$ (m s^{-1})	5	$\mathcal{N}(P_0, 2)$; $\mathcal{U}(10^{-5}, 100)$	3.89	$4.34^{+1.57}_{-1.28}$
$\sigma_{\mathrm{CARMENES-NIR}}$ (m s^{-1})	5	$\mathcal{N}(P_0, 2)$; $\mathcal{U}(10^{-5}, 100)$	5.00	$5.35^{+1.88}_{-1.97}$
σ_{NEID} (m s^{-1})	5	$\mathcal{N}(P_0, 2)$; $\mathcal{U}(10^{-5}, 100)$	5.00	$5.39^{+1.08}_{-0.95}$
$\sigma_{\mathrm{MAROON-X-blue}}$ (m s^{-1})	1	$\mathcal{N}(P_0, 2)$; $\mathcal{U}(10^{-5}, 100)$	1.00	$1.61^{+1.04}_{-0.95}$
$\sigma_{\mathrm{MAROON-X-red}}$ (m s^{-1})	1	$\mathcal{N}(P_0, 2)$; $\mathcal{U}(10^{-5}, 100)$	2.92	$3.32^{+0.89}_{-0.68}$
$\dot{\gamma}$ (m s^{-1} day^{-1})	10^{-5}	$\mathcal{U}(-50, 50)$	0.06	$0.08^{+0.01}_{-0.01}$

Note. "Fixed" indicates the parameter is fixed. $\mathcal{N}(\mu, \sigma)$ signifies a Gaussian prior with mean μ and standard deviation σ. $\mathcal{U}(\ell, r)$ signifies a uniform prior with left bound ℓ and right bound r.

Table 9
A Model Comparison Test for Planet b, Showing that the Most Favorable Model Includes no Planets

Planets	$\ln \mathcal{L}$	Δ AICc	Δ BIC	N free	χ^2_{red}
None	-278.95	0.00	0.00	13	1.79
b	-282.22	15.89	19.54	16	1.97

of the system, we can exclude blended background eclipsing binaries. From our EXOFASTv2 analysis of all the ground and TESS transits, and also from an independent analysis considering only the MuSCAT2 transits, we can decisively rule out an unresolved companion with a circum-secondary transiting object (Section 4.3), and we can also rule out a HEB with a pair of low-mass eclipsing stellar companions (Section 4.4). Under the circum-secondary and HEB scenarios, we would observe a variable transit depth as a function of wavelength, and this is definitively excluded. The same result is obtained by analyzing only the simultaneous quad-band MuSCAT2 transit light curves.

This effect is readily observable in the *B*-band transits, which in these scenarios would produce shallower transits due to an increasing flux contrast between the primary and secondary at shorter wavelengths, but this is not observed. Similarly, the HEB model for the TESS light curve produces an eclipse ("V") shape that is inconsistent with the data, which shows steeper ingresses and egresses due to a smaller planet-to-star radius ratio. While we do not explore the possibility that the secondary could be a hotter white dwarf, we do not see any evidence for UV excess or discrepant broadband photometric colors.

6.1.2. Assessing the Impact of Stellar Activity On Our Ability to Recover a Mass for TOI 620 b from Our Radial Velocities

Stellar oscillations, photospheric convection, magnetic activity, and the rotation of starspots can impart net shifts in spectral lines which appear as systematic noise in RV time series (Luhn et al. 2020). There is no evidence that TOI 620 is a particularly active star, but even the moderate activity characteristic of middle-aged stars can obfuscate the Keplerian signals of low-mass planets and require careful analysis to mitigate (e.g., Cale et al. 2021; Plavchan et al. 2015; Dumusque et al. 2010, 2011; Rajpaul et al. 2015; Vanderburg et al. 2016). One approach is to use photometry of the star (reflecting the extent, rotation, and migration of starspots) as a proxy for activity and its affect on the RV signals, and essentially regress and subtract the photometry-estimated RV variation. In an attempt to recover the Keplerian signal of TOI 620 b, we perform a Gaussian process (GP) regression of the RV time series using a quasiperiodic kernel (or covariance matrix) with hyperparameters determined by an FF' analysis (Aigrain et al. 2012) of the TESS light curve:

$$K(t_i, t_j) = \eta_\sigma^2 \exp\left[-\frac{\Delta t^2}{2\eta_\tau^2} - \frac{1}{2\eta_\ell^2} \sin^2\left(\pi \frac{\Delta t}{\eta_P}\right)\right], \quad (3)$$

where $\Delta t \equiv |t_j - t_i|$. In this definition, η_σ is the amplitude of the autocorrelation in the signal, η_τ is the mean starspot lifetime, η_ℓ is a smoothness parameter, and η_P is the stellar rotation period. We use the FF' analysis technique to estimate η_τ, η_ℓ, and η_P, but since the TESS photometry and RV observations were not contemporaneous, we must fit for the wavelength-dependent amplitudes η_σ using the RV data alone. That being said, the variation in the TESS light curve is around 0.2%, and if we

Table 10
A Comparison of Recovered RV Semiamplitudes and Mass Upper Limits, Excluding Individual Instruments

Removed Dataset	CARMENES-Vis	CARMENES-NIR	MAROON-X blue	MAROON-X red	NEID
MAP K (m s^{-1})	3.07×10^{-10}	2.24×10^{-9}	1.91×10^{-9}	4.95×10^{-9}	3.36×10^{-7}
MCMC K (m s^{-1})	$0.85^{+1.14}_{-0.63}$	$0.56^{+0.81}_{-0.42}$	$0.41^{+0.60}_{-0.30}$	$0.47^{+0.73}_{-0.35}$	$2.06^{+1.48}_{-1.35}$
5σ M ($M_{\oplus}$)	11.88	9.88	11.58	10.69	15.74

Note. The MAP and MCMC Recovered Semiamplitudes, 68% Confidence Intervals, and 5σ Upper Mass Limits of TOI 620 b are shown in Cases where we Remove a Single Dataset (and iSHELL), Fixing $\dot{\gamma} = 0$, and allow for Eccentricities up to 0.5. In no combination of remaining data sets do we recover a detection for TOI 620 b, and in all cases we still arrive at much lower velocity semiamplitude upper limits than expected from a mass–radius relation.

Table 11
The Model Parameters and Prior Distributions Used in our RV Model that Considers the Transiting b Planet, an Additional c Planet at 17.7 Days, and the Linear $\dot{\gamma}$ Trend, as well as the Recovered MAP Fit and MCMC Posteriors

Parameter (units)	Initial Value (P_0)	Priors	MAP Value	MCMC Posterior
P_b (days)	5.09881	Fixed	…	…
$T_{C,b}$ (days)	2458518.007	Fixed	…	…
e_b	10^{-5}	$\mathcal{U}(0, 0.5)$	10^{-5}	$0.19^{+0.22}_{-0.18}$
ω_b	$\pi/2$	$\mathcal{U}(-\pi, \pi)$	3.14	$-0.41^{+2.45}_{-1.74}$
K_b (m s^{-1})	5	$\mathcal{U}(0, \infty)$	4.46×10^{-3}	$0.32^{+0.48}_{-0.24}$
P_c (days)	17.7	$\mathcal{N}(P_0, 0.1)$	17.97	$17.72^{+0.08}_{-0.07}$
$T_{C,c}$ (days)	2458518.007	$\mathcal{U}(P_0 \pm P_c/2)$	2458526.86	$2458520.49^{+3.19}_{-3.47}$
e_c	10^{-5}	$\mathcal{U}(0, 1)$	1.02×10^{-5}	$0.20^{+0.30}_{-0.18}$
ω_c	$\pi/2$	$\mathcal{U}(-\pi, \pi)$	3.14	$1.45^{+0.76}_{-2.48}$
K_c	10	$\mathcal{U}(0, \infty)$	4.36	$4.74^{+1.14}_{-1.06}$
γ_{iSHELL} (m s^{-1})	−8.448	$\mathcal{U}(P_0 \pm 100)$	0.70	$2.48^{+2.98}_{-3.05}$
$\gamma_{\text{CARMENES−Vis}}$ (m s^{-1})	−0.783	$\mathcal{U}(P_0 \pm 100)$	0.60	$0.35^{+1.76}_{-1.79}$
$\gamma_{\text{CARMENES−NIR}}$ (m s^{-1})	−1.510	$\mathcal{U}(P_0 \pm 100)$	−1.51	$-0.28^{+3.83}_{-3.87}$
γ_{NEID} (m s^{-1})	−1.525	$\mathcal{U}(P_0 \pm 100)$	1.40	$0.99^{+1.25}_{-1.30}$
$\gamma_{\text{MAROON−X−blue}}$ (m s^{-1})	−0.033	$\mathcal{U}(P_0 \pm 100)$	−5.40	$-5.92^{+1.30}_{-1.31}$
$\gamma_{\text{MAROON−X−red}}$ (m s^{-1})	−1.770	$\mathcal{U}(P_0 \pm 100)$	−6.87	$-7.02^{+1.46}_{-1.54}$
σ_{iSHELL} (m s^{-1})	5	$\mathcal{N}(P_0, 2); \mathcal{U}(10^{-5}, 100)$	13.04	$13.32^{+1.16}_{-1.10}$
$\sigma_{\text{CARMENES−Vis}}$ (m s^{-1})	5	$\mathcal{N}(P_0, 2); \mathcal{U}(10^{-5}, 100)$	2.69	$3.20^{+1.78}_{-1.49}$
$\sigma_{\text{CARMENES−NIR}}$ (m s^{-1})	5	$\mathcal{N}(P_0, 2); \mathcal{U}(10^{-5}, 100)$	5.00	$5.08^{+1.94}_{-1.92}$
σ_{NEID} (m s^{-1})	5	$\mathcal{N}(P_0, 2); \mathcal{U}(10^{-5}, 100)$	3.64	$4.17^{+1.11}_{-0.95}$
$\sigma_{\text{MAROON−X−blue}}$ (m s^{-1})	1	$\mathcal{N}(P_0, 2); \mathcal{U}(10^{-5}, 100)$	0.97	$0.79^{+0.86}_{-0.55}$
$\sigma_{\text{MAROON−X−red}}$ (m s^{-1})	1	$\mathcal{N}(P_0, 2); \mathcal{U}(10^{-5}, 100)$	1.98	$2.68^{+0.82}_{-0.65}$
$\dot{\gamma}$ (m s^{-1} day^{-1})	10^{-5}	$\mathcal{U}(-50, 50)$	0.06	$0.06^{+0.01}_{-0.01}$

Note. "Fixed" indicates the parameter is fixed. $\mathcal{N}(\mu, \sigma)$ signifies a Gaussian prior with mean μ and standard deviation σ. $\mathcal{U}(\ell, r)$ signifies a uniform prior with left bound ℓ and right bound r.

assume a $v \sin i \sim 2$ km s^{-1} this leads to an expected RV semiamplitude from stellar rotation of $\sim$4 m s^{-1}.

To derive an FF' RV stellar activity model, we first median-normalize the TESS PDC-SAP light curve and mask out the transits and the edges of the light-curve data. We then choose knots at evenly spaced intervals of 0.5 days (excluding any that happen to fall within the TESS data-dump regions) and use scipy to fit a cubic spline to the data, which is used to compute both F and its first derivative, F', and multiply them together. We also then arbitrarily divide the FF' curve by its standard deviation for normalization, since the amplitude will be fit for separately with the RV data. The light curves with the best-fit cubic splines in each sectors are shown in Figure 19. We perform an MCMC fitting analysis with wide uniform priors on $\eta_\sigma \sim \mathcal{U}(0.03, 6)$, $\eta_\tau \sim \mathcal{U}(5, 2000)$, and $\eta_\ell \sim \mathcal{U}(0.1, 0.6)$, while we use a Gaussian prior for η_P based

on periodogram analysis at $\sim$8.9 days. Instead of accounting for intrinsic error bars in the data, we also fit a jitter term, $\sigma_{LC} \sim \mathcal{U}(10^{-5}, 0.2)$. We find a strong doubly peaked posterior on η_P at $8.99^{+0.03}_{-0.04}$ and $9.94^{+0.03}_{-0.04}$ days, the former of which is close to the Lomb–Scargle periodogram peak.

Taking the results of the FF' analysis and using them as priors for GP hyperparameters, we incorporate separate quasiperiodic GPs for each RV instrument in our data set, fixing the model values for η_τ and η_P, while allowing η_ℓ and η_σ to vary. Each instrument has an independent amplitude, $\eta_{\sigma,i}$, but the other three hyperparameters are shared between all instruments. A full summary of the priors used in these runs is shown in Appendix B. The GP analysis is performed using the methods outlined in Cale et al. (2021). Using the 8.99 day η_P, we find well-behaved posteriors, but all GP amplitudes are consistent with 0. We encounter similar results with the 9.94
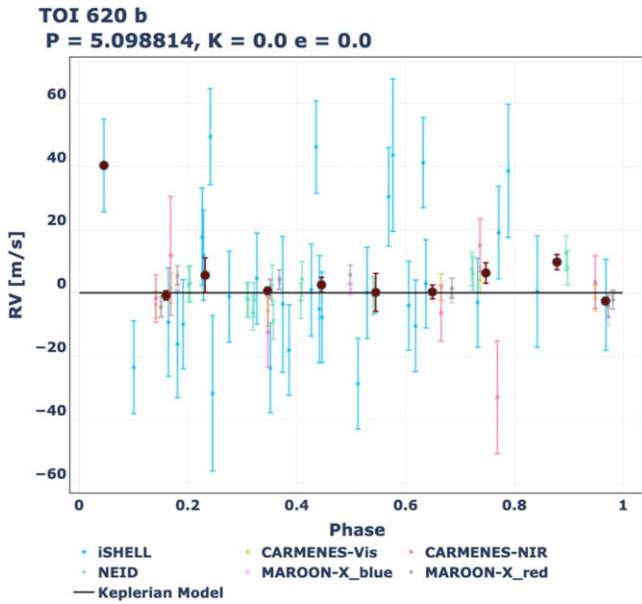
Figure 17. RV time series phased to the period of b, with the black model representing the planet's MAP model fit. The maroon data points are binned RVs every 0.1 in phase. A careful inspection reveals that the RVs are marginally more consistent with a negative K_b, although in this circum-primary scenario we assume a prior of $K_b > 0$.

day η_P. Thus, accounting for stellar activity does not significantly improve our recovery of K_b. In other words, stellar activity is not degrading our recovery of a mass for TOI 620 b.

Another potential source of systematic error would be the superposition of two or more dissimilar spectra as a consequence of unresolved stellar companions; this is separate from the Keplerian signal imparted by any such companion. Contamination of the light from the primary by the secondary could result in blended spectral lines and distorted line shapes. The changing relative Doppler shift of the spectra along the orbit could lead to time variation in the line shape and spurious variation in the measured RV. A standard diagnosis of this effect is the line bisector (Santos et al. 2002), but there is no evidence for such a systematic in our PRV spectra. Additionally, this effect would exhibit a strongly chromatic effect on our RVs, more pronounced in red and NIR wavelengths than the blue visible, due to the lower companion flux contrast toward the red. However, we do not observe any significant difference in the recovery of K_b when excluding the red and NIR RVs in Table 10.

6.1.3. Are There Additional Short-orbital-period Keplerian Companions Masking Our Radial Velocity Recovery of TOI 620 b?

Additional planets in the system might manifest themselves as low-significance signals in Fourier analysis of the RV time series. We search for such signals with a generalized Lomb–Scargle (GLS) periodogram, iteratively removing each identified signal in our model and examining the residuals, shown in Figure 20. We confirm this analysis by creating a corresponding $\ln \mathcal{L}$ periodogram, which shows consistent results.

We recover a 17.7 day signal at $>4\sigma$ significance and with a semiamplitude corresponding to a planet mass of $M_P \sin i = 13.1^{+2.8}_{-2.9} M_\oplus$ and a semimajor axis $a_\mathrm{p} = 0.111^{+0.002}_{-0.002}$ au using the mass of the primary host star and corresponding

Table 12
A Model Comparison Test for Planets b and c Showing that the Most Favorable Model Includes only the c Planet

Planets	$\ln \mathcal{L}$	Δ AICc	Δ BIC	N free	χ^2_red
c	−263.22	0.00	0.00	18	1.77
None	−278.27	13.98	8.46	13	1.77
b, c	−267.39	19.44	21.32	21	1.92
b	−280.69	28.15	26.27	16	1.89

uncertainty from our EXOFASTv2 analysis in Section 3.2. The MAP and MCMC posteriors are listed in Table 11 along with the model's priors, and we present the phased and full RV plots in Figures 18 and 21, and an abbreviated MCMC corner plot in Figure 22. Our model comparison (see Table 12) shows that the model that includes a second ("c") planet candidate is the most favored, but any model including the b planet is disfavored and models without the "c" planet are not ruled out. In other words, the inclusion of a c planet in our RV model does not improve our recovery of a mass for TOI 620 b, nor are we statistically confident in the recovery of the c planet. Analysis of the predicted T_C also shows that this planet is likely not transiting. The uncertainty in the T_C is high; the predicted transit windows are marked in Figure 19. While the TOI 620 b transits are readily apparent by eye, no transits for TOI 620 c are seen.

Taken as a whole, we cannot confirm the c planet as statistically significant ($>5\sigma$) with only the RV data and model comparison presented herein. We also note that 17.7 days is approximately twice the ~8.9 day signal seen in the TESS light curves (Figure 19), and could instead be potentially related to stellar activity. K_c is very close to the expected RV semiamplitude from a stellar rotation of ~4 m s^{-1}. Assuming 17.7 days is the true stellar rotation period, we would have identified the 8.9 day harmonic as the most prominent signal, instead, since our analysis of a single TESS sector light curve would be insensitive to the true period. If this is the case, then our RV data contain no direct evidence for additional planets in the system, and additional RV follow-up will be needed to rule in or out a c planet and/or stellar activity.

6.1.4. The Detection Threshold Mass of TOI 620 b

To assess our detection efficiency versus planet mass, we carry out injection and recovery tests of the RV data. In these tests, we inject simulated Keplerian signals with known orbital parameters ($\{P, e, \omega, T_P, K\}$) into our combined RV data. The time of injected periastron (T_P) is arbitrarily set as 2459273.623416268, which is close to the median of the data, and e_i and ω_i are set to 0. We consider 20 period values from 1.12345–10.12345 days, and 30 semiamplitude values from 0.1–100 m s^{-1}, both evenly spaced in log space to broadly sample our RV sensitivity as a function of orbital period. We model each data set assuming a Keplerian signal with a circular orbit, and with no Keplerian signal but including a linear trend. We also model the injected planet with the period P_i and ephemerides $T_{C,i}$ fixed at the injected values. The only parameter of the injected planet that we do allow to vary is K_i, which we start at 5 m s^{-1} and invoke $\mathcal{U}(0, \infty)$.

For each planet that is injected, we run an MCMC to determine how well we recover K_i and its corresponding uncertainty, and two MAP fits: one with a model that includes the injected planet and one without. A two-dimensional histogram of this recovery data is shown in Figure 23, where
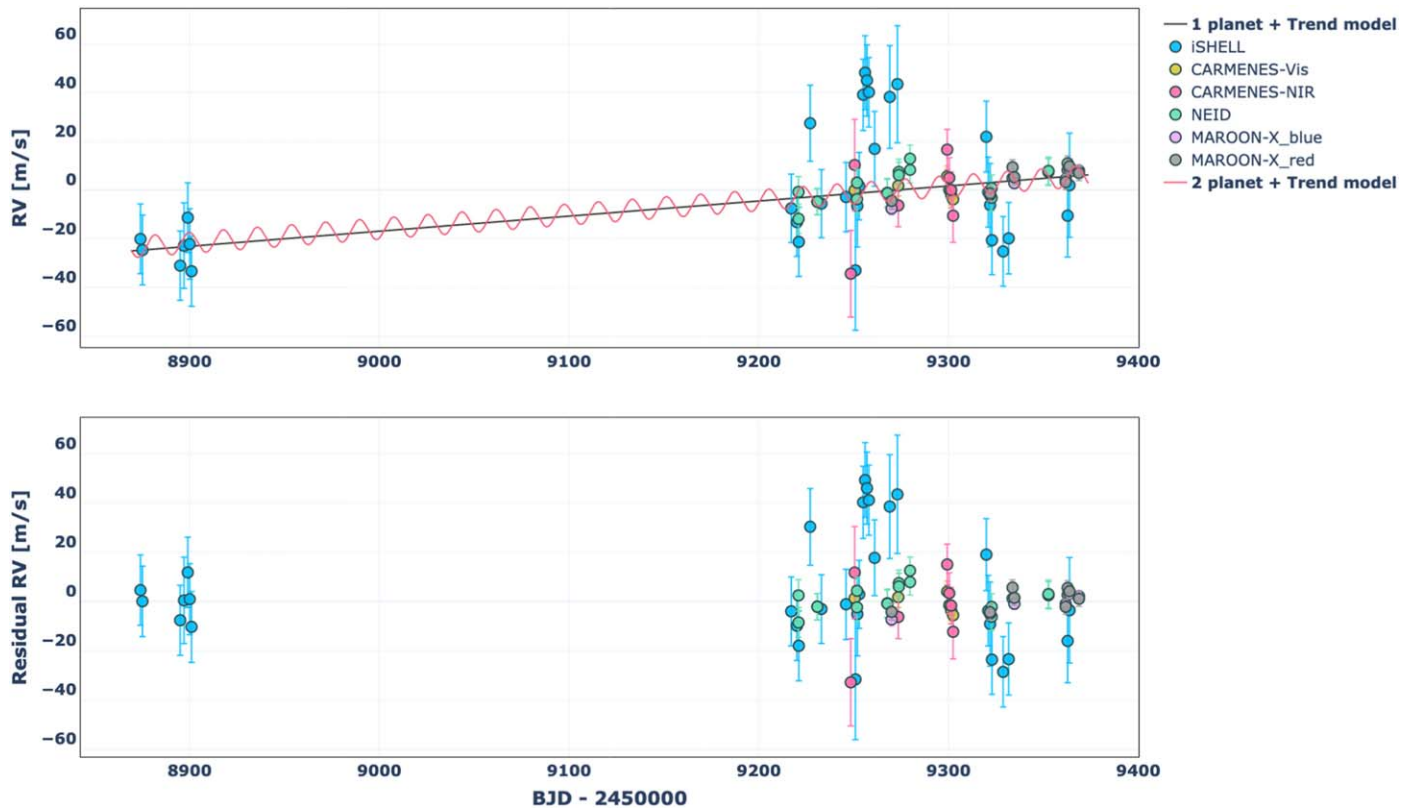
Figure 18. Full unphased RV time series as a function of time, with the black dashed lines representing our one-planet and two-planet (Section 6.1.3) MAP models with the linear trend. The top plot shows the RVs for each instrument and error bars over the full time baseline of observations, while the bottom plot shows the residuals (data − model). The one- and two-planet models have slightly different (<2 m s^{-1}) RV offsets (γ) for each data set, as enumerated in Tables 8 and 11, respectively, but only the one-planet RV offsets are applied to the data as shown for clarity.
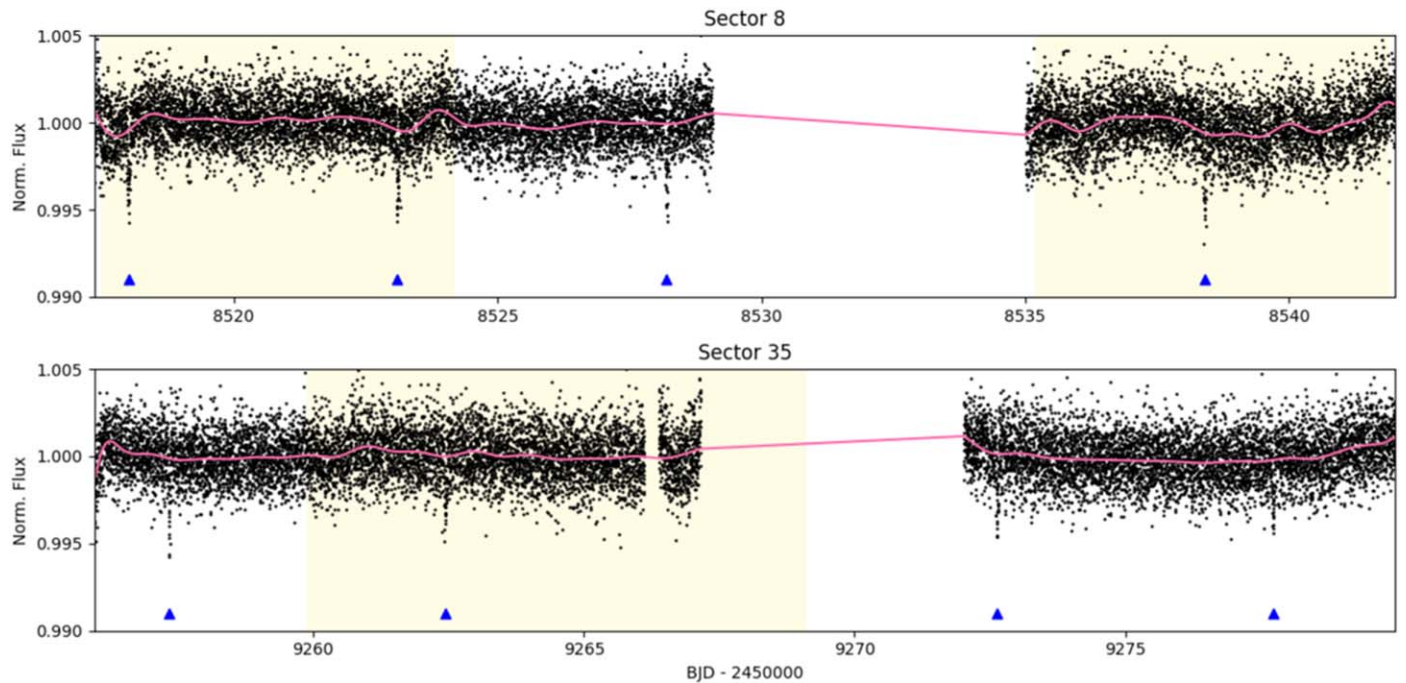
Figure 19. The TESS PDC-SAP light curve of TOI 620 from Sector 8 (top) and Sector 35 (bottom) plotted as a function of time. The times of transit for TOI 620 b are indicated with blue triangles. Data gaps during sectors are due to data downlinks, momentum dumps, and other data artifacts and systematics such as scattered light. The best-fit cubic spline polynomial is shown in pink, and is fitted to the data with the transits of TOI 620 b masked out. Any interpolation in the data-dump regions are thrown out. The yellow shaded regions show the predicted transit windows for TOI 620 c from our two-planet MCMC analysis, showing no obvious presence of a more massive transiting companion to TOI 620 b (see Section 6.1.3)
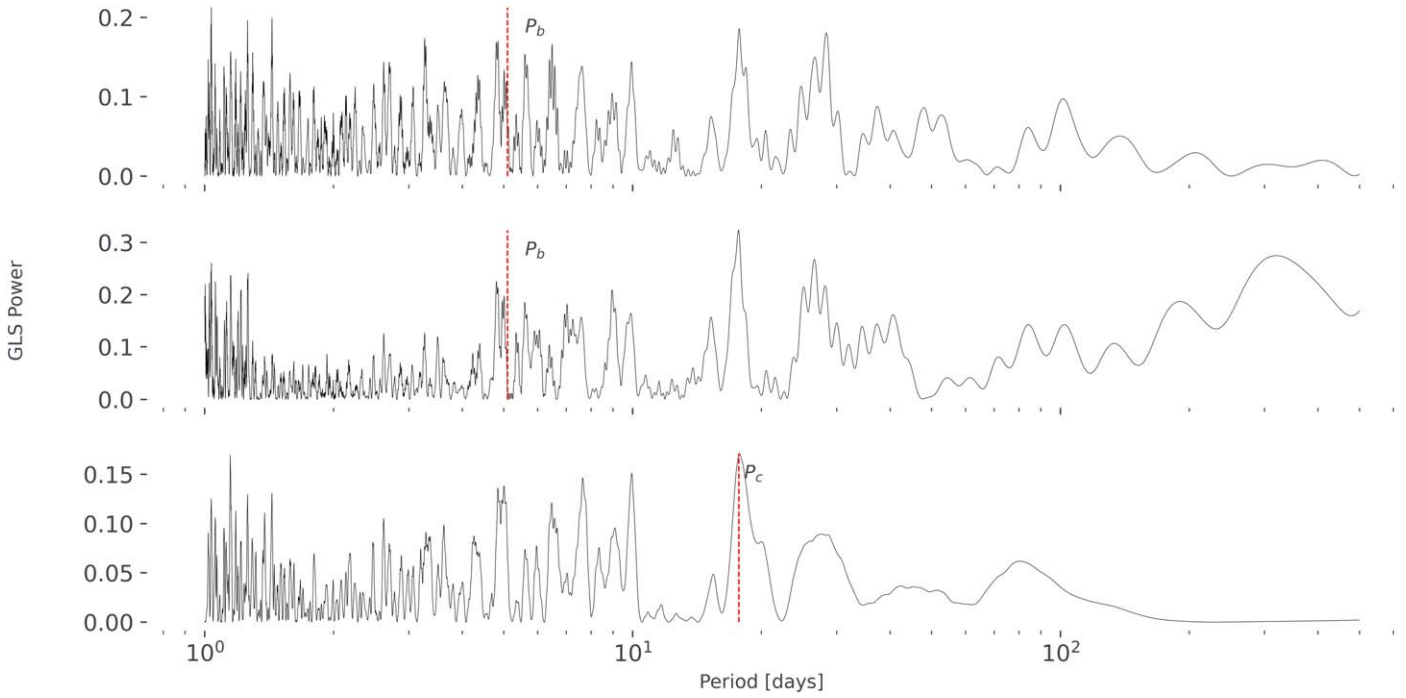
Figure 20. A series of generalized Lomb–Scargle periodograms examining the signals in our TOI 620 RV time series. The horizontal axes are all logarithmic. All three panels depict a single-planet search with a floating T_C. The top panel includes no extra planets, the middle panel models out TOI 620 b to search for a second planet, and the bottom panel models out both TOI 620 b and the linear RV trend to search for a second planet. The periods of b and the tentative c are marked with dashed red vertical lines in each panel.
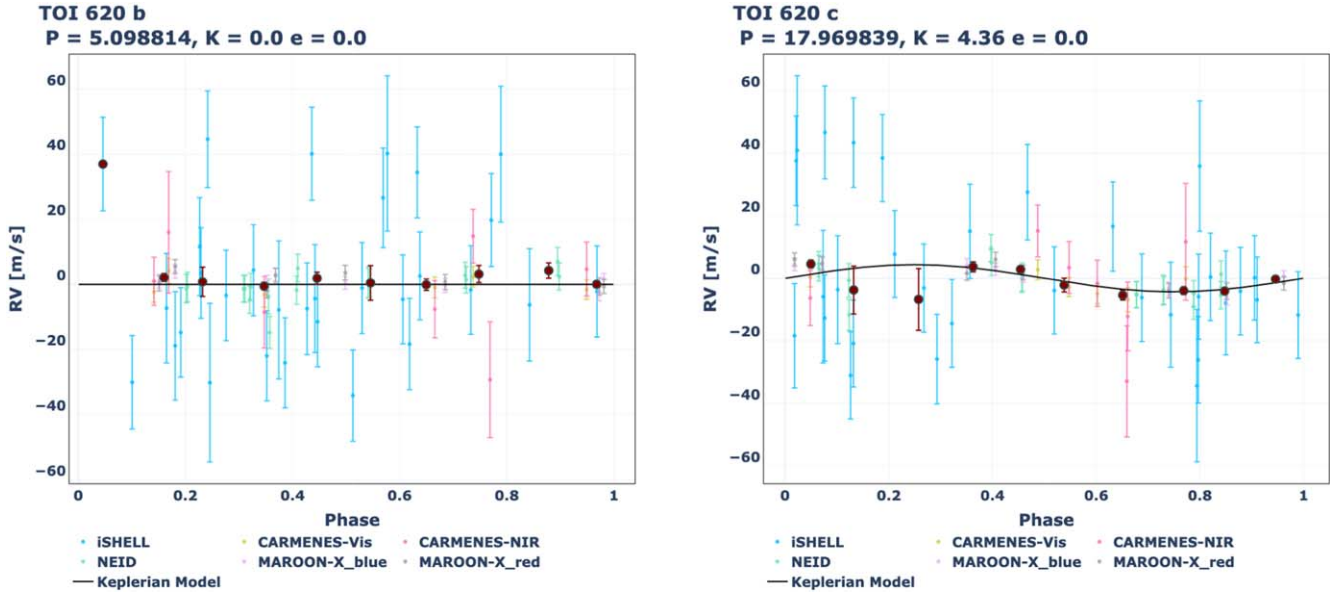
Figure 21. RV time-series plot for our two-planet model phased to the periods of b (left) and c (right), with the black models representing the planet's MAP model fits. The maroon points are binned RVs every 0.1 in orbital phase.

the left panel presents the recovered semiamplitude as a fraction of its uncertainty. The right three charts are one-dimensional histograms depicting the same data as the left panel, for specific ranges of P_i. We can therefore conclude that significant recoveries are possible for our model for a range of orbital periods for any semiamplitudes above ∼3 m s^{-1}. This is the sensitivity limit above which our model begins to recover semiamplitudes of the same order as the injected values, with a confidence of $\geqslant 3\sigma$. This strengthens our confidence that our

upper limit on the Doppler amplitude of TOI 620 b is not limited by RV noise, as a 3 m s^{-1} sensitivity should be well within reasonable expectations to recover a signal at 6.5–8.4 m s^{-1}, as anticipated from the Chen & Kipping (2016) mass–radius relation.

6.2. Are There Additional Massive Companions in the System?

The evidence for a second, massive companion in the system consists of the elevated value of the RUWE statistic (Section 3.7),
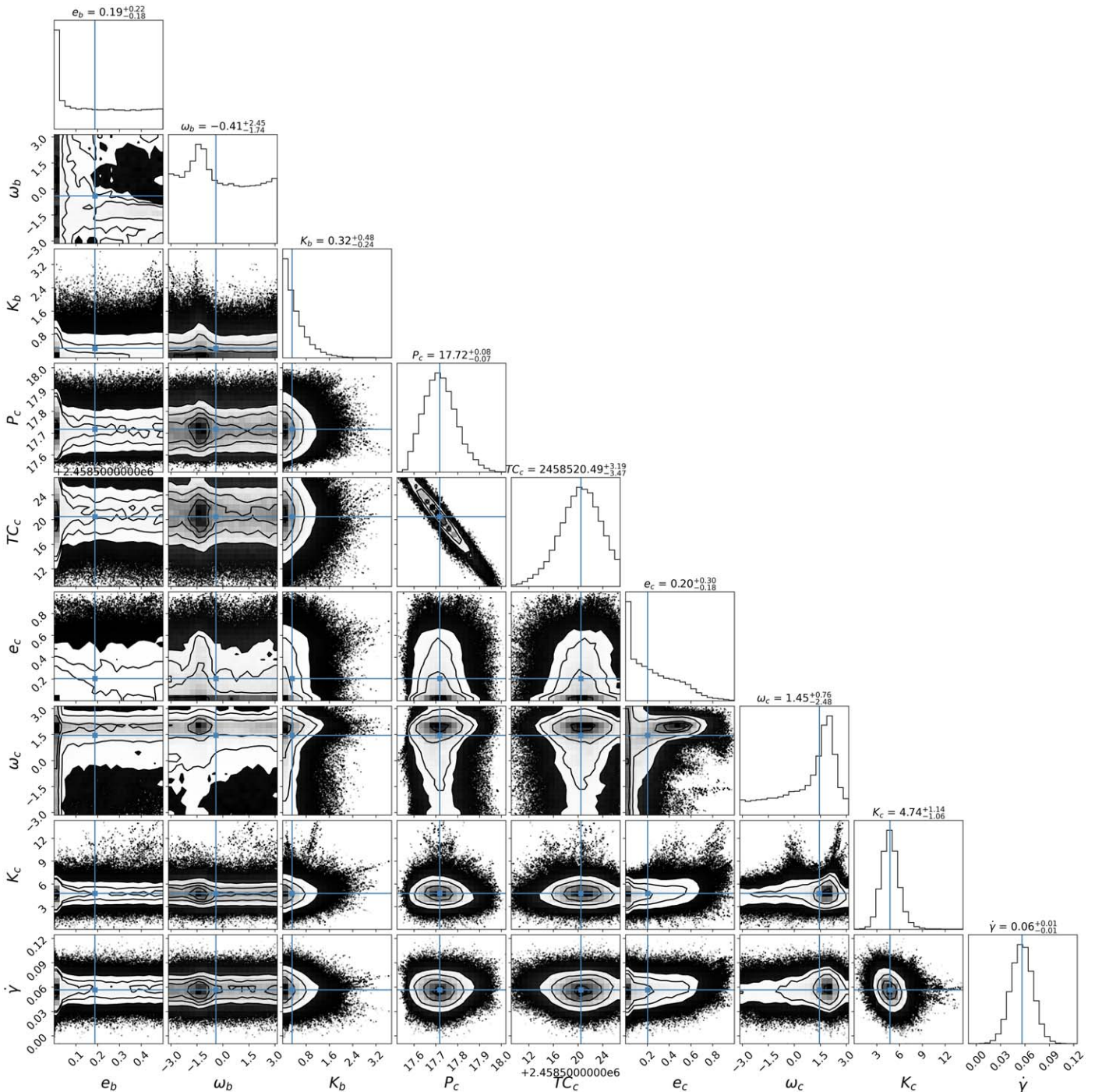
Figure 22. MCMC corner plot of our b and c model with all RV data points included, showing the posterior distributions of each model parameter that we allowed to vary. The gamma offsets and jitter terms are not shown, as they are all uncorrelated and to a good approximation are ideal Gaussian distributions.

which describes the error in the fit of the Gaia astrometry to a single-star solution, the nonzero linear trend (0.08 ± 0.01 m s^{-1} day^{-1}) in our RV data (Section 5.1), and the double-star or hierarchical binary solutions to our spectroscopic modeling of the high-resolution iSHELL NIR spectra (Section 3.8). However, the historical imaging and high-contrast imaging rule out any background star contamination, or any bound stellar companions with angular separations $\gtrsim 0\rlap{.}''2$. Therefore any luminous companions would have to be in a pathological situation where the projected angular separation is much less than the true separation; otherwise, the companion must be a less-luminous brown dwarf or massive Jupiter as constrained in Section 3.7. Further long-term RV monitoring, deeper high-contrast imaging, and the upcoming Gaia DR3, scheduled to be released in April–June, and which
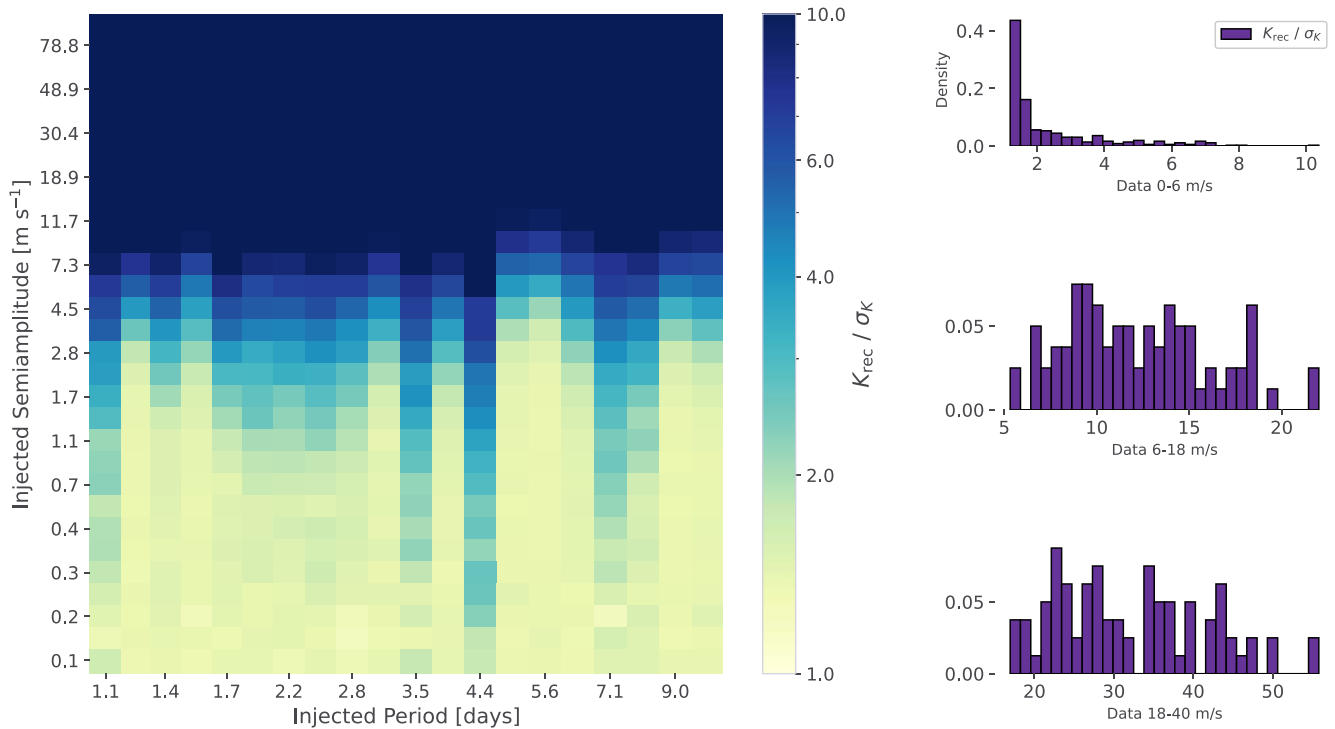
Figure 23. Left: a two-dimensional histogram depicting the recovered semiamplitude of the injected planet in units of the recovered uncertainty, where values above ∼3 represent recoveries. Each tile represents an MCMC analysis performed where the injected planet has a period and semiamplitude determined by the horizontal and vertical axis position of the tile. Both axes scale logarithmically, but the color bars do not. Right: the right three panels are one-dimensional histograms of the same data depicted in the left histogram, but binned into different groups based on the value of the injected semiamplitude. The top histogram covers 0–6 m s^{-1}, the middle 6–18 m s^{-1}, and the bottom 18–40 m s^{-1}. The vertical axes of these histograms are normalized probability densities rather than bin counts.

presumably will include a revised and more accurate RUWE value for TOI 620, may unveil this hidden companion.

6.3. How Old is the TOI 620 System?

A young age for TOI 620 could help explain the anomolously low density for TOI 620 b. However, considering all the data relevant to the age of TOI 620, the short rotation period of ∼9 days is the only indication we have that TOI 620 is potentially a young system. As covered in Section 3.4, the *UVW* space motion of the star does not implicate it as a member of any cluster, and we see no emission in Hα, Na I D lines, X-rays, FUV, NUV, or APASS u'. Additionally, the 17.7 day RV signal in Section 6.1.3 may instead indicate that the rotation period is twice as long and TOI 620 relatively older. Thus, we cannot at this time put a constraint on the age of the system.

6.4. The Implications of a Low-density TOI 620 b

Exhausting all other explanations for our nonrecovery of a Doppler RV signal, we derive a 5σ upper limit in the circum-primary favored scenario of $M_P \leqslant 7.1\ M_\oplus$. When combined with radius estimates from the circum-primary transit data analysis, $R_p = 3.76 \pm 0.15\ R_\oplus$, this gives us a 5σ upper limit on the density of $\rho_P \leqslant 0.74\ \mathrm{g\,cm}^{-3}$, making TOI 620 b one of the puffiest Neptunes ever discovered (see Figure 24).

We calculate updated transmission and emission spectroscopy metrics for TOI 620 b as described in Kempton et al. (2018). Using the 5σ upper limit on the mass, this gives a *lower*
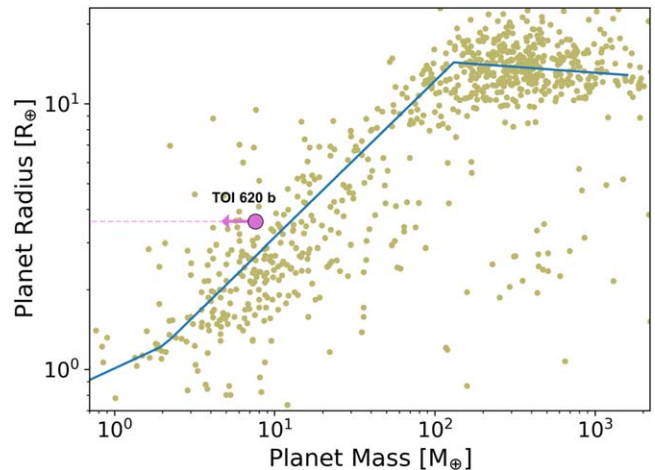
Figure 24. The mass–radius diagram for all exoplanets with provided radii and masses from the NASA Exoplanet Archive. TOI 620 b's 5σ upper limit is plotted in pink with an arrow and dashed line. The arrow extends back down to the median mass from our MCMC chains. The blue line traces the Chen & Kipping (2016) relation. This plot demonstrates that TOI 620 is among some of the lowest-density Neptune-sized planets known.

limit on the TSM to be 327, which already places it within the first (most valuable) TSM quartile defined in Kempton et al. (2018), and higher than any other Neptune-sized TOI using the Chen–Kipping mass–radius relation, as in Figure 1. The new ESM estimate is also significantly larger, at 17.

As mentioned in Section 3.4, there is no evidence (including excess UV/X-ray brightness) that TOI 620 is a young

(<1 Gyr) star. Thus, we can rule youth out as a possible mechanism for the low density of TOI 620 b. There have been a few proposed alternative mechanisms for superpuff formations and observations, including an augmentation of the observed planetary radius due to the presence of photochemical hazes in the upper atmosphere (Gao & Zhang 2020). Lee & Chiang (2016) instead propose that superpuffs form in the outer disk regions (>1 au) with lower opacities and are able to accrete more H/He via rapid cooling. They then migrate inwards to their present locations. In contrast, Millholland (2019) proposes that obliquity tides inflate the radii of superpuffs. This explanation does not require a dominantly H/He atmosphere, but does require planets to be close to the host star, which may be plausible with TOI 620's semimajor axis of <0.05 au. Due to its abnormally low density, this planet would be a good candidate for He λ108030 nm transmission spectroscopy and low-resolution spectrophotometry in order to detect broad spectral features such as Rayleigh scattering or the broad wings of Na and K (e.g., WASP-127 b and WASP-21 b; Chen et al. 2018, 2020) in future work. Although WASP-127 b and WASP-21 b are both hotter than TOI 620, TOI 620 would allow for the exploration of the broad continuum of much cooler atmospheres dominated by other species.

7. Conclusions and Future Work

In this work, we have presented a rigorous exploration and validation of the TOI 620 system based on two seasons of RV measurements from iSHELL, CARMENES, MAROON-X, and NEID, and photometric data from TESS and ground-based follow-up observations from NGTS, LCO, MuSCAT2, TMMT, LCRO, ExTrA and KeplerCam, and high-resolution images from Gemini South, NIRI, NIRC2, NESSI, and ShaneAO.

Taking all of the transit and RV analysis results into account, we can conclude that TOI 620 b is a highly underdense transiting exoplanet orbiting the primary M2.5 star, with $P = 5.0988179 \pm 0.0000045$ days, $T_C = 2458518.00718 \pm 0.00093$, $R_\mathrm{p} = 3.76 \pm 0.15$ $R_\oplus$, and 5σ upper limits of $M_P \leqslant 7.1$ $M_\oplus$ and $\rho_P \leqslant 0.74$ g cm^{-3}. From the RV trend, Gaia RUWE statistic, and high-contrast imaging, we also find a possible additional hidden Jupiter-mass companion planet at $\sim$3 au *or* an ultracool dwarf at 20–30 au. We additionally present a candidate periodic signal in the data at 17.7 days that shows up prominently in the residuals of both our GLS and ln$\mathcal{L}$ periodograms. Injection and recovery analyses show that we can reliably recover planets in the RVs down to $\sim$3 m s^{-1}. We are also able to robustly exclude circum-secondary and hierarchical eclipsing binary scenarios from the chromatic transit light curves.

More RV data is needed to further constrain the mass of TOI 620 b, rule in or out the candidate RV signal at 17.7 days, and to continue to monitor the linear RV trend for a turnover. Deeper high-contrast imaging and aperture masking interferometry with instruments like Keck could resolve a possible bright companion at smaller angular separations than have been analyzed in this paper, and further constrain the mass–semimajor axis parameter space allowed for the hidden massive outer companion. Finally, the nearby TOI 620 b, with its NIR-bright host star, is among the best targets for atmospheric characterization with the JWST, given its abnormally low density and large atmospheric scale-height with a TSM $\geqslant$ 327.

Appendix A
Updated Methods for ISHELL Forward Modeling

Once we have a full set of reduced, extracted spectra from iSHELL, the spectra must be forward-modeled to extract RVs, accounting for the stellar spectrum, gas cell, telluric absorption, fringing sources, and the LSF of the order traces. First, pychell requires an initial guess for the stellar template based on the properties of the host star. Using the effective temperature, radius, mass, and effective gravity estimates from ExoFOP-TESS (IPAC 2015) in our original RV fits via pychell, we assume a solar metallicity and create an initial stellar template with $T = 3500$ K, $\log(g) = 4.5$, and [Fe/H] = 0.0 using the SVO's theoretical spectra web server to create a BT-Settl model,[57] which we further refine by Doppler broadening the spectrum to the rotational velocity of the star, which we assumed to be 2 km s^{-1} from the TRES spectra analysis (Section 3.1). Barycenter velocities are also generated as an input via the barycorrpy library (Kanodia & Wright 2018), based on the algorithms from Wright & Eastman (2014).

The initial fitting produced a suboptimal stellar template with absorption lines that were too shallow and unphysical telluric velocities. To produce better results, we performed tests by varying the stellar template temperatures from 3000–4000 K, in steps of 100 K, on a subgroup of gathered spectra, and found that the 4000 K templates produced the lowest rms flux residuals and deeper stellar absorption lines. We used this as our initial template going forward. The discrepancy between this initial guess and our posteriors from EXOFASTv2 does not greatly impact our results thanks to our iterative stellar template process. We choose to "iterate" the stellar template by coadding residuals in the stellar rest frame, and repeating the forward modeling of the extracted spectra, a process known as iterative Jacobian deconvolution. We iterate for a total of 10 times to obtain final RV measurements; 10 iterations of the stellar template and repeated forward modeling is chosen because additional iterations do not yield significant further reductions in the RVs' or flux residuals' rms. Individual RV measurements for a given night are coadded using a series of statistical weighting techniques across images and orders to obtain binned nightly RV measurements and error bars to generate our final nightly RV measurements. After this iterative process, the final 10th iteration stellar template is best described by an effective temperature of ∼3800 K rather than the starting value of 4000 K. This demonstrates the ramifications of the iterative process and how it converges on a more accurate stellar template by using our empirical spectra, which is particularly useful when synthetic spectra are lacking in some NIR-opacity sources. This is the template that was used in our SB2 analysis (Section 3.8). These methods are described further in Cale et al. (2019).

With one coadded RV measurement per observation night, we again use pychell, this time in combination with the codependent package optimize, which is a general-purpose Bayesian analysis tool that pychell expands upon with RV-specific MCMC tools and is very similar in implementation to radvel (Fulton et al. 2018). We have filtered out two individual spectra from UT 2021 February 5 and one from UT 2021 May 29, due to RV measurements that did not converge properly and were in disagreement with other spectra from the same night by hundreds of kilometers per second. We suspect

---

[57] http://svo2.cab.inta-csic.es/theory/newov2/index.php?models=bt-settl

this was due to an initially poor focus on the night of observation of 1″5 that was later improved to 1″1, giving us an overall S/N of only 87 for the night. We also removed the entire nights of UT 2020 May 17, 2020 June 14, and 2021 June 4, the latter of which is due to poor spectral fits and individual RV measurements that were also inconsistent. In this case, we suspect the cause of poor data may have been due to the high air mass of TOI 620 during observations, which reached 1.8. The first two nights do seem internally consistent and the spectral fits appear to be of the expected quality, but the final coadded RV measurements are radically different from all other data, at >150 m s^{-1} and <-70 m s^{-1}, respectively, putting them both more than 3σ away from the expected RV trend. It is possible that these were caused by flare events or unfortunate slit alignments, or potentially they even may be physical if they correspond to the periastron of a highly eccentric companion. With the data we have collected, however, we cannot say

anything definitive about these outlier RV data points and remove them from our analysis.

Appendix B
Circum-primary: Transit Times and Vetting Plots for the One-planet case, and Priors for the GP Case

Here we present additional Figures and Tables specifically relating to false-positive vetting and the circum-primary transit and RV models. Table B1 shows the transit times, impact parameters, and depths for each transit used in our circum-primary model. Figures B1 and B2 show TESS Sector 8 and Sector 34 light-curve analyses, and Figure B3 shows photo-center difference images and PSFs, all from DAVE. Figure B4 depicts the results of our vespa analysis using galactic population statistics. Finally, Table B2 gives the priors used in our single-planet GP RV models, and Figure B5 shows the unphased RV time-series for these models.

$TIC_000296739893$, P = 5.098870 Days, E = 1512.906252 Days

Pri	Sec	Ter	Pos	FA₁	FA₂	F_Red	Pri-Ter	Pri-Pos	Sec-Ter	Sec-Pos	Odd-Evn	DMM	Shape	TAT
30.0	3.56	3.25	4.46	5.02	2.57	1.25	26.8	25.6	0.32	-0.89	0.39	1.00	0.13	1.22
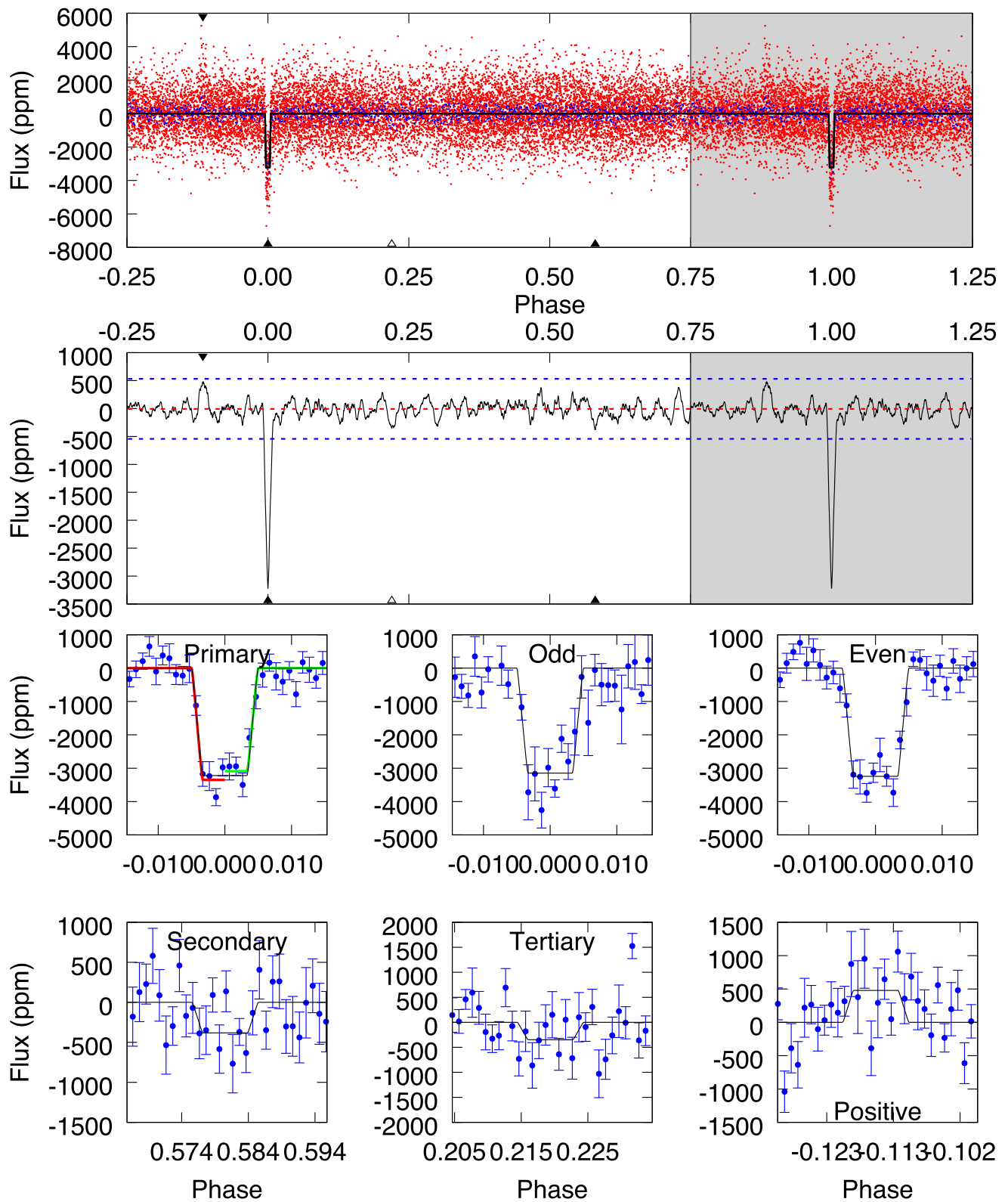
Figure B1. Sector 8 DAVE Report for TOI 620. The top panel shows phased transit data, with TESS data in red, binned data in blue, and repeated data in the gray region. The transit model is the black curve. The middle panel shows autocorrelated flux over the same phase. The bottom six panels depict different phased scenarios showing primary, odd, even, secondary, tertiary, and positive transits.

$TIC_0 00296739893$, P = 5.098870 Days, E = 2252.237035 Days

| Pri	Sec	Ter	Pos	FA$_1$	FA$_2$	F$_{Red}$	Pri-Ter	Pri-Pos	Sec-Ter	Sec-Pos	Odd-Evn	DMM	Shape	TAT
27.8	4.76	3.86	2.95	5.02	2.57	1.15	23.9	24.9	0.91	1.82	0.28	1.00	0.10	0.21
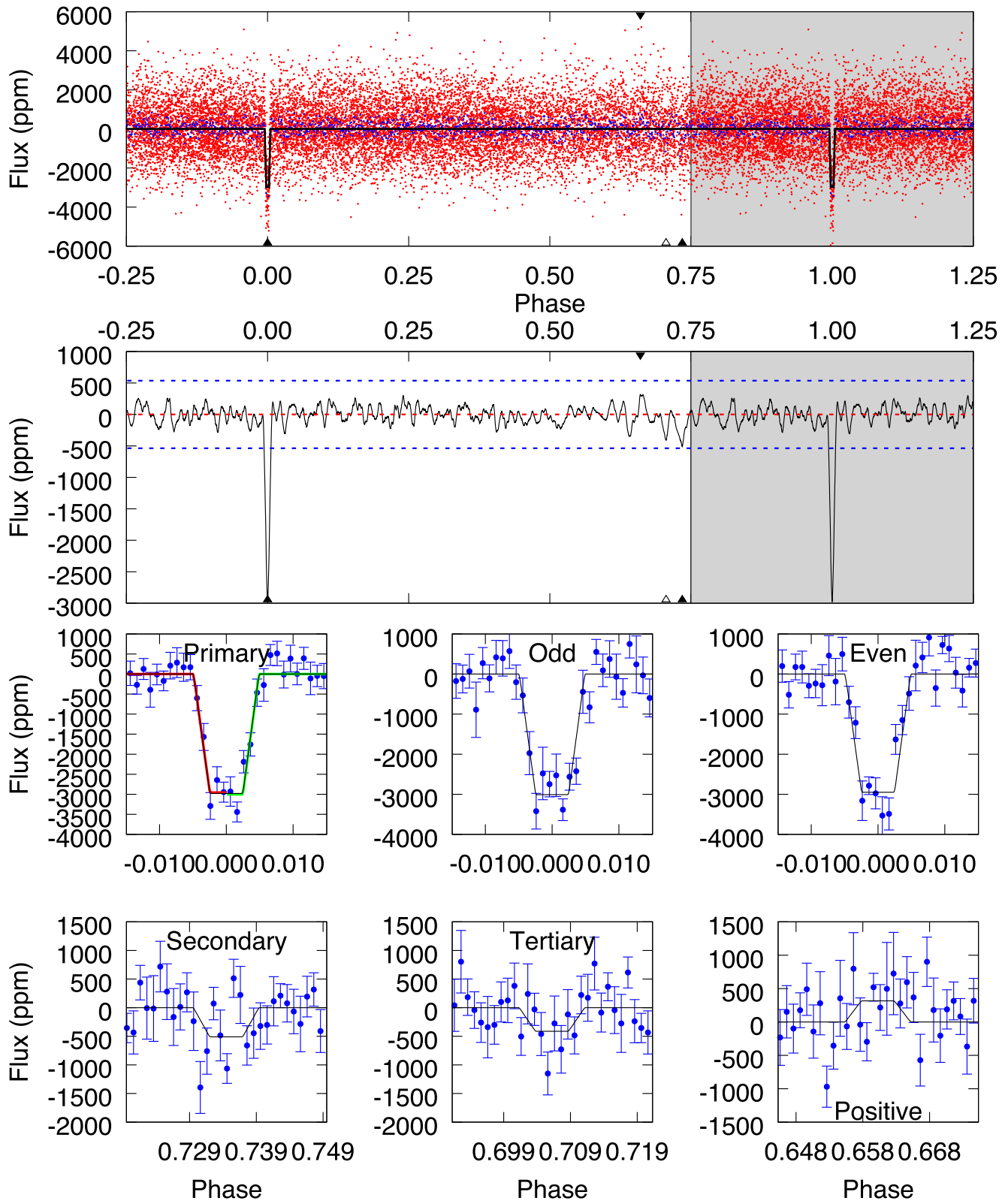
Figure B2. Sector 35 DAVE Report for TOI 620. The top panel shows phased transit data, with TESS data in red, binned data in blue, and repeated data in the gray region. The transit model is the black curve. The middle panel shows autocorrelated flux over the same phase. The bottom six panels depict different phased scenarios showing primary, odd, even, secondary, tertiary, and positive transits.
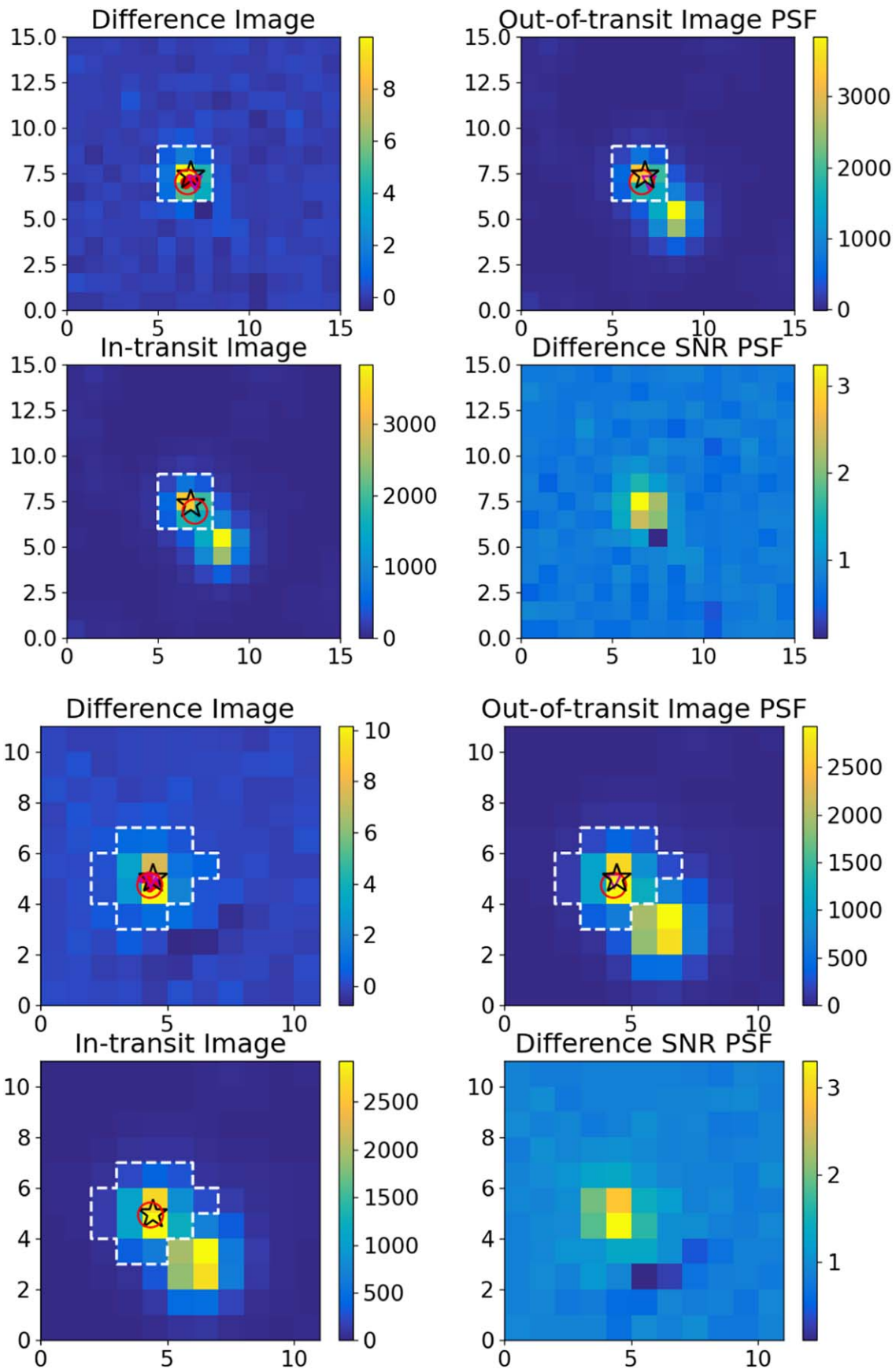
Figure B3. Photocenter difference images and PSFs for Sectors 8 (top 4) and 35 (bottom 4). The black-outlined star indicates the TIC position, while the red circle is the observed photocenter. The white dashed line indicates the TESS target pixels used to extract the light curve, just as the orange outlines showed in the TPF plot (Figure 2).
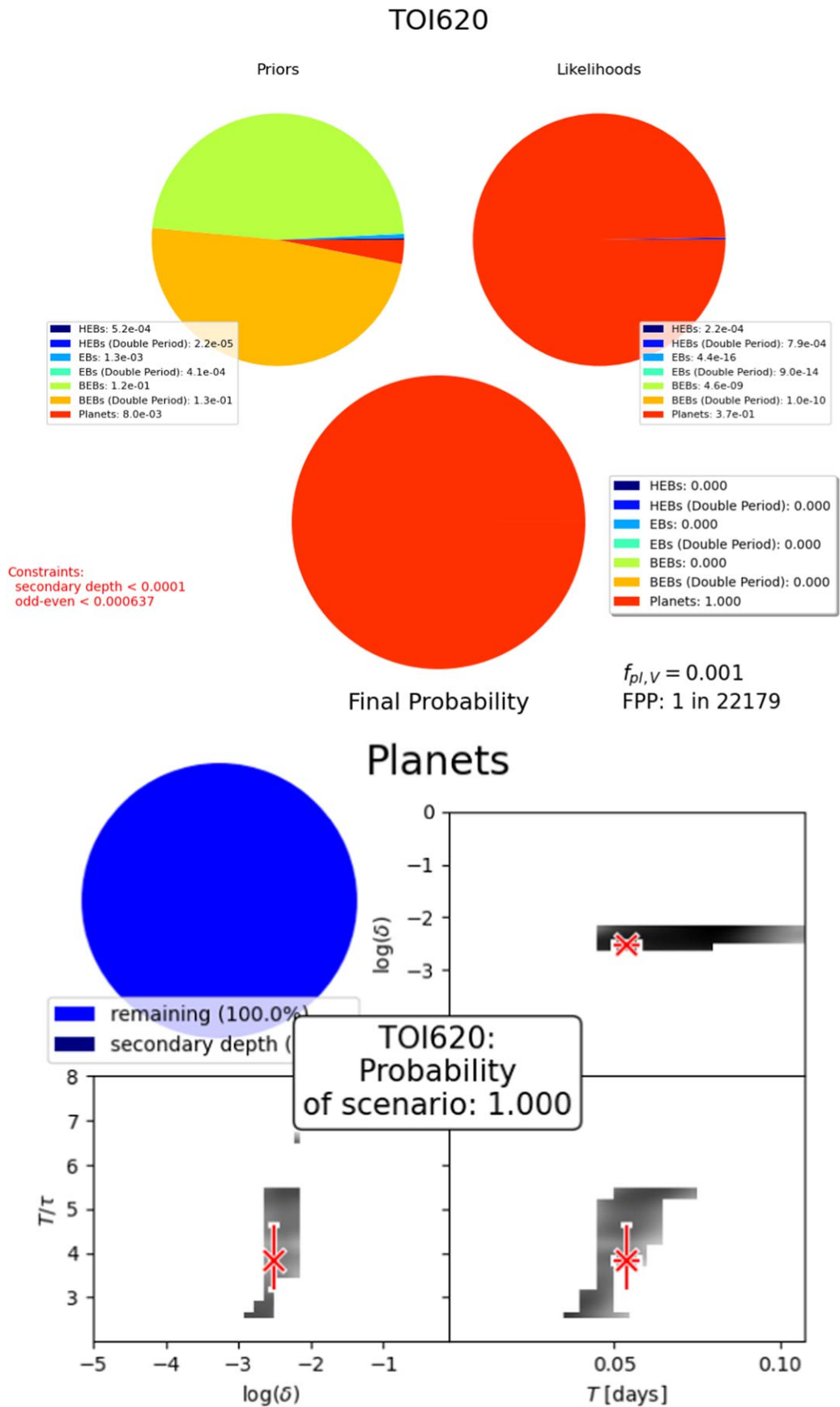
Figure B4. Top: pi charts of the prior probabilities, likelihoods, and posterior probabilities of TOI 620 assuming it is a planet or an EB, BEB, or HEB at 1 or 2 times the period, from vespa. Bottom: the probability of the planet scenario, and the position of TOI 620 in $\log \delta - T - T/\tau$ space compared to other planets taken from galactic population statistics, also from vespa.
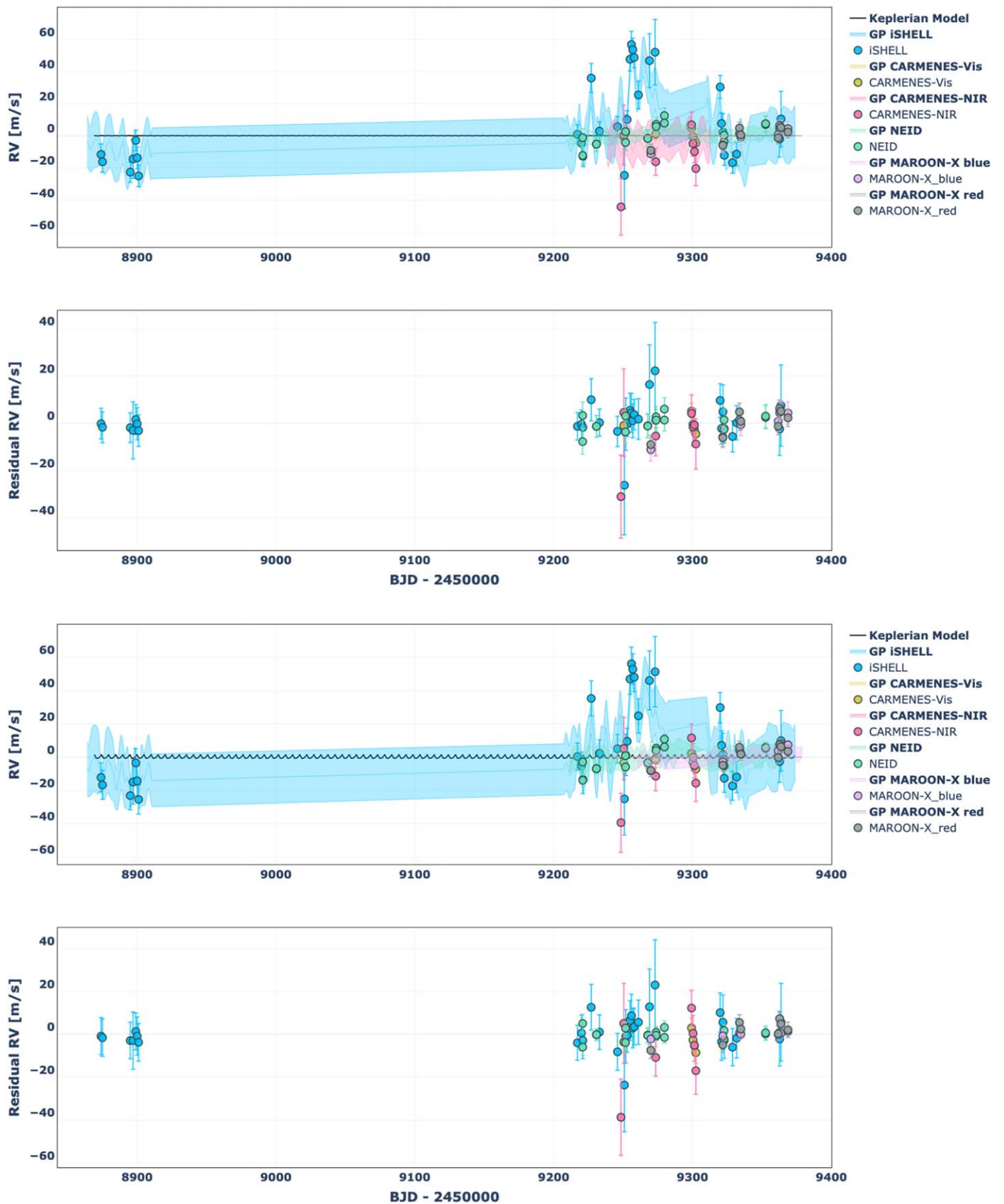
Figure B5. Full RV time-series plot for the Gaussian process (GP) model with the 8.99 day prior on η_P (top 2), and the 9.94 day prior on η_P (bottom 2), unphased. Residuals (data − model) are shown in the lower plots. In both cases, the GP models do not significantly improve our recovery of K_b.

Table B1
Median Values and 68% Confidence Interval for Transit Times, Impact Parameters, and Depths

| Transit	Planet	Epoch	T_T	b	Depth
TESS UT 2019-02-03 (TESS)	b	0	$2458518.00717^{+0.00050}_{-0.00051}$	$0.886^{+0.014}_{-0.017}$	$0.003226^{+0.00010}_{-0.000098}$
TESS UT 2019-02-08 (TESS)	b	1	$2458523.10599 \pm 0.00050$	$0.886^{+0.014}_{-0.017}$	$0.003226^{+0.00010}_{-0.000098}$
TESS UT 2019-02-13 (TESS)	b	2	$2458528.20481 \pm 0.00050$	$0.886^{+0.014}_{-0.017}$	$0.003226^{+0.00010}_{-0.000098}$
TESS UT 2019-02-23 (TESS)	b	4	$2458538.40244 \pm 0.00049$	$0.886^{+0.014}_{-0.017}$	$0.003226^{+0.00010}_{-0.000098}$
NGTS UT 2019-04-20 (R)	b	15	$2458594.48944 \pm 0.00045$	$0.886^{+0.014}_{-0.017}$	$0.00345^{+0.00026}_{-0.00027}$
LCO UT 2019-04-20 (z')	b	15	$2458594.48944 \pm 0.00045$	$0.886^{+0.014}_{-0.017}$	0.00330 ± 0.00014
TMMT UT 2019-04-25 (I)	b	16	$2458599.58826 \pm 0.00045$	$0.886^{+0.014}_{-0.017}$	0.00358 ± 0.00022
NGTS UT 2019-06-10 (R)	b	25	$2458645.47762 \pm 0.00042$	$0.886^{+0.014}_{-0.017}$	$0.00345^{+0.00026}_{-0.00027}$
MuSCAT2 UT 2020-01-16 (g')	b	68	$2458864.72679 \pm 0.00031$	$0.886^{+0.014}_{-0.017}$	$0.00314^{+0.00025}_{-0.00030}$
MuSCAT2 UT 2020-01-16 (i')	b	68	$2458864.72679 \pm 0.00031$	$0.886^{+0.014}_{-0.017}$	0.00290 ± 0.00018
MuSCAT2 UT 2020-01-16 (r')	b	68	$2458864.72679 \pm 0.00031$	$0.886^{+0.014}_{-0.017}$	0.00278 ± 0.00020
MuSCAT2 UT 2020-01-16 (z')	b	68	$2458864.72679 \pm 0.00031$	$0.886^{+0.014}_{-0.017}$	0.00330 ± 0.00014
KeplerCam UT 2020-01-26 (B)	b	70	$2458874.92442 \pm 0.00031$	$0.886^{+0.014}_{-0.017}$	$0.00313^{+0.00029}_{-0.00034}$
MuSCAT2 UT 2020-03-02 (g')	b	77	$2458910.61615 \pm 0.00030$	$0.886^{+0.014}_{-0.017}$	$0.00314^{+0.00025}_{-0.00030}$
MuSCAT2 UT 2020-03-02 (i')	b	77	$2458910.61615 \pm 0.00030$	$0.886^{+0.014}_{-0.017}$	0.00290 ± 0.00018
MuSCAT2 UT 2020-03-02 (r')	b	77	$2458910.61615 \pm 0.00030$	$0.886^{+0.014}_{-0.017}$	0.00278 ± 0.00020
MuSCAT2 UT 2020-03-02 (z')	b	77	$2458910.61615 \pm 0.00030$	$0.886^{+0.014}_{-0.017}$	0.00330 ± 0.00014
MuSCAT2 UT 2020-04-16 (g')	b	86	$2458956.50551 \pm 0.00030$	$0.886^{+0.014}_{-0.017}$	$0.00314^{+0.00025}_{-0.00030}$
MuSCAT2 UT 2020-04-16 (i')	b	86	$2458956.50551 \pm 0.00030$	$0.886^{+0.014}_{-0.017}$	0.00290 ± 0.00018
MuSCAT2 UT 2020-04-16 (r')	b	86	$2458956.50551 \pm 0.00030$	$0.886^{+0.014}_{-0.017}$	0.00278 ± 0.00020
MuSCAT2 UT 2020-04-16 (z')	b	86	$2458956.50551 \pm 0.00030$	$0.886^{+0.014}_{-0.017}$	0.00330 ± 0.00014
LCRO UT 2020-11-27 (i')	b	130	$2459180.85350 \pm 0.00035$	$0.886^{+0.014}_{-0.017}$	0.00290 ± 0.00018
MuSCAT2 UT 2021-01-07 (i')	b	138	$2459221.64404 \pm 0.00037$	$0.886^{+0.014}_{-0.017}$	0.00290 ± 0.00018
MuSCAT2 UT 2021-01-07 (r')	b	138	$2459221.64404 \pm 0.00037$	$0.886^{+0.014}_{-0.017}$	0.00278 ± 0.00020
MuSCAT2 UT 2021-01-07 (z')	b	138	$2459221.64404 \pm 0.00037$	$0.886^{+0.014}_{-0.017}$	0.00330 ± 0.00014
TESS UT 2021-02-11 (TESS)	b	145	$2459257.33576 \pm 0.00039$	$0.886^{+0.014}_{-0.017}$	$0.003226^{+0.00010}_{-0.000098}$
TESS UT 2021-02-16 (TESS)	b	146	$2459262.43458 \pm 0.00039$	$0.886^{+0.014}_{-0.017}$	$0.003226^{+0.00010}_{-0.000098}$
TESS UT 2021-02-27 (TESS)	b	148	$2459272.63222 \pm 0.00040$	$0.886^{+0.014}_{-0.017}$	$0.003226^{+0.00010}_{-0.000098}$
ExTrA UT 2021-03-04 (J)	b	149	$2459277.73104 \pm 0.00040$	$0.886^{+0.014}_{-0.017}$	$0.00336^{+0.00013}_{-0.00012}$
TESS UT 2021-03-04 (TESS)	b	149	$2459277.73104 \pm 0.00040$	$0.886^{+0.014}_{-0.017}$	$0.003226^{+0.00010}_{-0.000098}$
ExTrA UT 2021-04-13 (J)	b	157	$2459318.52158^{+0.00043}_{-0.00042}$	$0.886^{+0.014}_{-0.017}$	$0.00336^{+0.00013}_{-0.00012}$
ExTrA UT 2021-04-19 (J)	b	158	$2459323.62040 \pm 0.00043$	$0.886^{+0.014}_{-0.017}$	$0.00336^{+0.00013}_{-0.00012}$
ExTrA UT 2021-06-03 (J)	b	167	$2459369.50976 \pm 0.00046$	$0.886^{+0.014}_{-0.017}$	$0.00336^{+0.00013}_{-0.00012}$

Table B2

The Model Parameters and Prior Distributions used in Our GP RV Model that Considers an Eccentric Transiting b Planet and the Linear $\dot{\gamma}$ Trend, as used in Section 6.1.2

Parameter (units)	Initial Value (P_0)	Priors	Prior Citation
P_b (days)	5.09881	Fixed	This work
$T_{C,b}$ (days)	2458518.007	Fixed	This work
e_b	10^{-5}	$\mathcal{U}(0, 0.5)$	This work
ω_b	$\pi/2$	$\mathcal{U}(-\pi, \pi)$	This work
K_b (m s^{-1})	5	$\mathcal{U}(0, \infty)$	This work
γ_{iSHELL} (m s^{-1})	-8.448	$\mathcal{U}(P_0 \pm 100)$	This work
$\gamma_{\text{CARMENES−Vis}}$ (m s^{-1})	-0.783	$\mathcal{U}(P_0 \pm 100)$	This work
$\gamma_{\text{CARMENES−NIR}}$ (m s^{-1})	-1.510	$\mathcal{U}(P_0 \pm 100)$	This work
γ_{NEID} (m s^{-1})	-1.525	$\mathcal{U}(P_0 \pm 100)$	This work
$\gamma_{\text{MAROON−X−blue}}$ (m s^{-1})	0.017	$\mathcal{U}(P_0 \pm 100)$	This work
$\gamma_{\text{MAROON−X−red}}$ (m s^{-1})	-1.269	$\mathcal{U}(P_0 \pm 100)$	This work
σ_{iSHELL} (m s^{-1})	5	$\mathcal{N}(P_0, 2); \mathcal{U}(10^{-5}, 100)$	This work
$\sigma_{\text{CARMENES−Vis}}$ (m s^{-1})	5	$\mathcal{N}(P_0, 2); \mathcal{U}(10^{-5}, 100)$	This work
$\sigma_{\text{CARMENES−NIR}}$ (m s^{-1})	5	$\mathcal{N}(P_0, 2); \mathcal{U}(10^{-5}, 100)$	This work
σ_{NEID} (m s^{-1})	5	$\mathcal{N}(P_0, 2); \mathcal{U}(10^{-5}, 100)$	This work
$\sigma_{\text{MAROON−X−blue}}$ (m s^{-1})	1	$\mathcal{N}(P_0, 2); \mathcal{U}(10^{-5}, 100)$	This work
$\sigma_{\text{MAROON−X−red}}$ (m s^{-1})	1	$\mathcal{N}(P_0, 2); \mathcal{U}(10^{-5}, 100)$	This work
$\dot{\gamma}$ (m s^{-1} day^{-1})	0.08	$\mathcal{N}(0.08, 0.01)$	This work
$\eta_{\sigma,\text{iSHELL}}$ (m s^{-1})	0.9	$\mathcal{J}(0.01, 100)$	Cale et al. (2021)
$\eta_{\sigma,\text{CARMENES−Vis}}$ (m s^{-1})	0.9	$\mathcal{J}(0.01, 100)$	Cale et al. (2021)
$\eta_{\sigma,\text{CARMENES−NIR}}$ (m s^{-1})	0.9	$\mathcal{J}(0.01, 100)$	Cale et al. (2021)
$\eta_{\sigma,\text{NEID}}$ (m s^{-1})	0.9	$\mathcal{J}(0.01, 100)$	Cale et al. (2021)
$\eta_{\sigma,\text{MAROON−X−blue}}$ (m s^{-1})	0.9	$\mathcal{J}(0.01, 100)$	Cale et al. (2021)
$\eta_{\sigma,\text{MAROON−X−red}}$ (m s^{-1})	0.9	$\mathcal{J}(0.01, 100)$	Cale et al. (2021)
η_τ (days)	9.41/11.17	Fixed/Fixed	Cale et al. (2021)
η_ℓ	0.15/0.13	$\mathcal{N}(0.15, 0.1)/\mathcal{N}(0.13, 0.1)$	This work
η_P	8.99/9.94	Fixed/Fixed	This work

Note. "Fixed" indicates the parameter is fixed. $\mathcal{N}(\mu, \sigma)$ signifies a Gaussian prior with mean μ and standard deviation σ. $\mathcal{U}(\ell, r)$ signifies a uniform prior with left bound ℓ and right bound r. $\mathcal{J}(\ell, r)$ signifies a Jeffrey's prior with lower bound ℓ and upper bound r.

Appendix C
Circum-secondary: Analysis & Results, Transit Times, Transit and RV Posteriors, and Full Corner Plots

C.1. Transit Analysis

Here we present additional Figures and Tables relating to the circum-secondary transit models. Table C1 shows the prior distributions, Table C2 shows the transit times, impact parameters, and depths, and Table C3 shows the posterior distributions. Figure C1 shows the circum-secondary MCMC transit model in the B band.

We conduct a second independent analysis of the circum-secondary scenario using the simultaneous quad-band MuS-CAT2 data alone. Again, we find that the circum-secondary scenario is in contradiction with the results found in the SB2 analysis. In Figure C2, we show marginal and joint posteriors for a set of parameters (effective temperature of the host and contaminant stars, impact parameter, and host stellar density) plotted against the contamination fraction. The analysis yields

an upper limit to the flux from the primary of 19% of the brightness of the secondary, which is unphysical given that we are making the assumption in the circum-secondary analysis that the secondary must be much fainter than the primary.

C.2. Radial Velocity Analysis

Modeling the RVs of TOI 620 in the circum-secondary and HEB scenarios is identical to the circum-primary scenario with the exception of allowing the semiamplitude, K, to be negative. The physical manifestation of this result would suggest a large direct RV signal coming from a circum-secondary star or an HEB that is diluted by the primary light and thus reduced in amplitude by some (large) factor. In this case, we recover a negative K_b signal at 2.4σ significance (Table C4). Each RV instrument individually supports a negative K at varying statistical significance except MAROON-X. The RV plots for this scenario are presented in Figures C3 and C4. All of the posteriors are well behaved and uncorrelated.

Table C1
Prior Probability Distributions for Our EXOFASTv2 MCMC Simulations in the Circum-secondary case

Parameter (units)	Initial Value (P_0)	Priors	Prior Citation
M_* ($M_\odot$)	0.18	$\mathcal{U}(0.08, 0.30)$	This work
R_* ($R_\odot$)	0.18	$\mathcal{U}(0.08, 0.30)$	This work
$T_{\rm eff}$ (K)	3090	None	This work
A_V (mag)	0	$\mathcal{U}(P_0, 0.11625)$	Schlafly & Finkbeiner (2011)
ϖ (mas)	30.28300	$\mathcal{N}(P_0, 0.06117)$	Gaia Collaboration et al. (2018)
[Fe/H]	0	$\mathcal{N}(0, 1)$	this work
P (days)	5.098831	$\mathcal{U}(P_0 \pm 10\%)$	Eastman et al. (2019)
T_C (days)	2458518.005713	$\mathcal{U}(P_0 \pm P/3)$	Eastman et al. (2019)
R_p/R_*	0.344	None	This work
Dilute$_B$	0.991	$\mathcal{U}(0.98, 1)$	This work
Dilute$_J$	0.934	$\mathcal{U}(0.86, 1)$	This work
Dilute$_{g'}$	0.990	$\mathcal{U}(0.96, 1)$	This work
Dilute$_{r'}$	0.982	$\mathcal{U}(0.96, 1)$	This work
Dilute$_R$	0.982	$\mathcal{U}(0.96, 1)$	This work
Dilute$_{i'}$	0.962	$\mathcal{U}(0.92, 1)$	This work
Dilute$_{\rm TESS}$	0.974	$\mathcal{U}(0.94, 1)$	This work
Dilute$_I$	0.974	$\mathcal{U}(0.94, 1)$	This work
Dilute$_{z'}$	0.942	$\mathcal{U}(0.88, 1)$	This work

Note. $\mathcal{N}(\mu, \sigma)$ signifies a Gaussian prior with mean μ and standard deviation σ. $\mathcal{U}(\ell, r)$ signifies a uniform prior with left bound ℓ and right bound r. A_V is the extinction in the V band, and ϖ is the parallax. Dilute is the fraction of light from from close neighboring targets. Parameters that are missing, including orbital e, ω, are assumed to take default values of circular.

Table C2
Median Values and 68% Confidence Interval for Transit Times, Impact Parameters, and Depths for the Circum-secondary Case

Transit	Planet	Epoch	T_T	b	Depth
TESS UT 2019-02-03 (TESS)	b	0	$2458518.00730 \pm 0.00049$	$0.17^{+0.13}_{-0.11}$	$0.107^{+0.017}_{-0.015}$
TESS UT 2019-02-08 (TESS)	b	1	$2458523.10612 \pm 0.00049$	$0.17^{+0.13}_{-0.11}$	$0.107^{+0.017}_{-0.015}$
TESS UT 2019-02-13 (TESS)	b	2	$2458528.20494 \pm 0.00048$	$0.17^{+0.13}_{-0.11}$	$0.107^{+0.017}_{-0.015}$
TESS UT 2019-02-23 (TESS)	b	4	$2458538.40258 \pm 0.00048$	$0.17^{+0.13}_{-0.11}$	$0.107^{+0.017}_{-0.015}$
NGTS UT 2019-04-20 (R)	b	15	$2458594.48958 \pm 0.00044$	$0.17^{+0.13}_{-0.11}$	$0.108^{+0.019}_{-0.015}$
LCO UT 2019-04-20 (z')	b	15	$2458594.48958 \pm 0.00044$	$0.17^{+0.13}_{-0.11}$	$0.107^{+0.018}_{-0.015}$
TMMT UT 2019-04-25 (I)	b	16	$2458599.58840^{+0.00043}_{-0.00044}$	$0.17^{+0.13}_{-0.11}$	$0.105^{+0.019}_{-0.015}$
NGTS UT 2019-06-10 (R)	b	25	$2458645.47777 \pm 0.00041$	$0.17^{+0.13}_{-0.11}$	$0.108^{+0.019}_{-0.015}$
MuSCAT2 UT 2020-01-16 (g')	b	68	$2458864.72697^{+0.00030}_{-0.00031}$	$0.17^{+0.13}_{-0.11}$	$0.126^{+0.025}_{-0.020}$
MuSCAT2 UT 2020-01-16 (i')	b	68	$2458864.72697^{+0.00030}_{-0.00031}$	$0.17^{+0.13}_{-0.11}$	$0.109^{+0.019}_{-0.015}$
MuSCAT2 UT 2020-01-16 (r')	b	68	$2458864.72697^{+0.00030}_{-0.00031}$	$0.17^{+0.13}_{-0.11}$	$0.106^{+0.018}_{-0.015}$
MuSCAT2 UT 2020-01-16 (z')	b	68	$2458864.72697^{+0.00030}_{-0.00031}$	$0.17^{+0.13}_{-0.11}$	$0.107^{+0.018}_{-0.015}$
KeplerCam UT 2020-01-26 (B)	b	70	$2458874.92461^{+0.00030}_{-0.00031}$	$0.17^{+0.13}_{-0.11}$	$0.126^{+0.027}_{-0.023}$
MuSCAT2 UT 2020-03-02 (g')	b	77	$2458910.61634^{+0.00029}_{-0.00030}$	$0.17^{+0.13}_{-0.11}$	$0.126^{+0.025}_{-0.020}$
MuSCAT2 UT 2020-03-02 (i')	b	77	$2458910.61634^{+0.00029}_{-0.00030}$	$0.17^{+0.13}_{-0.11}$	$0.109^{+0.019}_{-0.015}$
MuSCAT2 UT 2020-03-02 (r')	b	77	$2458910.61634^{+0.00029}_{-0.00030}$	$0.17^{+0.13}_{-0.11}$	$0.106^{+0.018}_{-0.015}$
MuSCAT2 UT 2020-03-02 (z')	b	77	$2458910.61634^{+0.00029}_{-0.00030}$	$0.17^{+0.13}_{-0.11}$	$0.107^{+0.018}_{-0.015}$
MuSCAT2 UT 2020-04-16 (g')	b	86	$2458956.50571 \pm 0.00029$	$0.17^{+0.13}_{-0.11}$	$0.126^{+0.025}_{-0.020}$
MuSCAT2 UT 2020-04-16 (i')	b	86	$2458956.50571 \pm 0.00029$	$0.17^{+0.13}_{-0.11}$	$0.109^{+0.019}_{-0.015}$
MuSCAT2 UT 2020-04-16 (r')	b	86	$2458956.50571 \pm 0.00029$	$0.17^{+0.13}_{-0.11}$	$0.106^{+0.018}_{-0.015}$
MuSCAT2 UT 2020-04-16 (z')	b	86	$2458956.50571 \pm 0.00029$	$0.17^{+0.13}_{-0.11}$	$0.107^{+0.018}_{-0.015}$
LCRO UT 2020-11-27 (i')	b	130	$2459180.85373^{+0.00034}_{-0.00035}$	$0.17^{+0.13}_{-0.11}$	$0.109^{+0.019}_{-0.015}$
MuSCAT2 UT 2021-01-07 (i')	b	138	$2459221.64428 \pm 0.00037$	$0.17^{+0.13}_{-0.11}$	$0.109^{+0.019}_{-0.015}$
MuSCAT2 UT 2021-01-07 (r')	b	138	$2459221.64428 \pm 0.00037$	$0.17^{+0.13}_{-0.11}$	$0.106^{+0.018}_{-0.015}$
MuSCAT2 UT 2021-01-07 (z')	b	138	$2459221.64428 \pm 0.00037$	$0.17^{+0.13}_{-0.11}$	$0.107^{+0.018}_{-0.015}$
TESS UT 2021-02-11 (TESS)	b	145	$2459257.33601 \pm 0.00039$	$0.17^{+0.13}_{-0.11}$	$0.107^{+0.017}_{-0.015}$
TESS UT 2021-02-16 (TESS)	b	146	$2459262.43483 \pm 0.00039$	$0.17^{+0.13}_{-0.11}$	$0.107^{+0.017}_{-0.015}$
TESS UT 2021-02-27 (TESS)	b	148	$2459272.63246^{+0.00039}_{-0.00040}$	$0.17^{+0.13}_{-0.11}$	$0.107^{+0.017}_{-0.015}$
ExTrA UT 2021-03-04 (J)	b	149	$2459277.73128 \pm 0.00040$	$0.17^{+0.13}_{-0.11}$	$0.121^{+0.021}_{-0.017}$
TESS UT 2021-03-04 (TESS)	b	149	$2459277.73128 \pm 0.00040$	$0.17^{+0.13}_{-0.11}$	$0.107^{+0.017}_{-0.015}$
ExTrA UT 2021-04-13 (J)	b	157	$2459318.52183 \pm 0.00042$	$0.17^{+0.13}_{-0.11}$	$0.121^{+0.021}_{-0.017}$
ExTrA UT 2021-04-19 (J)	b	158	$2459323.62065 \pm 0.00043$	$0.17^{+0.13}_{-0.11}$	$0.121^{+0.021}_{-0.017}$
ExTrA UT 2021-06-03 (J)	b	167	$2459369.51002 \pm 0.00046$	$0.17^{+0.13}_{-0.11}$	$0.121^{+0.021}_{-0.017}$

Table C3
Median Values and 68% Confidence Interval for the Circum-secondary Case

Parameter	Units	Values
Stellar Parameters:		
M_*…	Mass ($M_\odot$)…	$0.183^{+0.037}_{-0.035}$
R_*…	Radius ($R_\odot$)…	0.201 ± 0.016
L_*…	Luminosity ($L_\odot$)…	$0.0054^{+0.0039}_{-0.0030}$
ρ_*…	Density (cgs)…	$31.8^{+2.6}_{-3.0}$
$\log g$…	Surface gravity (cgs)…	$5.091^{+0.030}_{-0.034}$
$T_{\rm eff}$…	Effective temperature (K)…	3470^{+440}_{-560}
[Fe/H]…	Metallicity (dex)…	$-0.40^{+0.63}_{-0.84}$
[Fe/H]$_0$…	Initial metallicity[a]…	$-0.43^{+0.61}_{-0.83}$
Age…	Age (Gyr)…	$6.8^{+4.8}_{-4.7}$
EEP…	Equal evolutionary phase[b]…	248^{+15}_{-24}
Planetary Parameters:		b
P…	Period (days)…	5.0988187 ± 0.0000045
R_P…	Radius ($R_\oplus$)…	$6.66^{+0.67}_{-0.62}$
M_P…	Predicted mass[c] ($M_\oplus$)…	40^{+16}_{-11}
T_C…	Time of conjunction[d] (BJD$_{\rm TDB}$)…	$2458518.00730 \pm 0.00049$
T_T…	Time of minimum projected separation[e] (BJD$_{\rm TDB}$)…	$2458518.00730 \pm 0.00049$
T_0…	Optimal conjunction time[f] (BJD$_{\rm TDB}$)…	$2458966.70335 \pm 0.00029$
a…	Semimajor axis (au)…	$0.0329^{+0.0021}_{-0.0022}$
i…	Inclination (Degrees)…	$89.73^{+0.19}_{-0.23}$
$T_{\rm eq}$…	Equilibrium temperature[g] (K)…	414^{+53}_{-67}
$\tau_{\rm circ}$…	Tidal circularization timescale (Gyr)…	$1.98^{+0.92}_{-0.59}$
K…	RV semiamplitude[c] (m/s)…	47^{+18}_{-12}
R_P/R_*…	Radius of planet in stellar radii…	$0.304^{+0.024}_{-0.021}$
a/R_*…	Semimajor axis in stellar radii…	$35.24^{+0.92}_{-1.1}$
δ…	$(R_P/R_*)^2$…	$0.092^{+0.015}_{-0.012}$
$\delta_{\rm B}$…	Transit depth in B (fraction)…	$0.175^{+0.19}_{-0.064}$
$\delta_{\rm I}$…	Transit depth in I (fraction)…	$0.107^{+0.028}_{-0.018}$
$\delta_{\rm J}$…	Transit depth in J (fraction)…	$0.149^{+0.054}_{-0.035}$
$\delta_{\rm R}$…	Transit depth in R (fraction)…	$0.112^{+0.033}_{-0.019}$
$\delta_{g'}$…	Transit depth in g' (fraction)…	$0.176^{+0.13}_{-0.057}$
$\delta_{i'}$…	Transit depth in i' (fraction)…	$0.114^{+0.031}_{-0.020}$
$\delta_{r'}$…	Transit depth in r' (fraction)…	$0.109^{+0.028}_{-0.019}$
$\delta_{z'}$…	Transit depth in z' (fraction)…	$0.112^{+0.026}_{-0.019}$
$\delta_{\rm TESS}$…	Transit depth in TESS (fraction)…	$0.106^{+0.022}_{-0.016}$
τ…	Ingress/egress transit duration (days)…	$0.0144^{+0.0012}_{-0.0010}$
T_{14}…	Total transit duration (days)…	$0.0595^{+0.0015}_{-0.0013}$
$T_{\rm FWHM}$…	FWHM transit duration (days)…	$0.04504^{+0.00097}_{-0.00094}$
b…	Transit impact parameter…	$0.17^{+0.13}_{-0.11}$
$\delta_{S,2.5\mu m}$…	Blackbody eclipse depth at 2.5 μm (ppm)…	$0.36^{+1.0}_{-0.33}$
$\delta_{S,5.0\mu m}$…	Blackbody eclipse depth at 5.0 μm (ppm)…	114^{+100}_{-75}
$\delta_{S,7.5\mu m}$…	Blackbody eclipse depth at 7.5 μm (ppm)…	670^{+330}_{-320}
ρ_P…	Density[c] (cgs)…	$0.76^{+0.29}_{-0.19}$
$\log g_P$…	Surface gravity[c]…	$2.95^{+0.13}_{-0.11}$
Θ…	Safronov number…	$0.078^{+0.029}_{-0.019}$
$\langle F \rangle$…	Incident flux (10^9 erg s^{-1} cm^{-2})…	$0.0067^{+0.0042}_{-0.0034}$
T_P…	Time of periastron (BJD$_{\rm TDB}$)…	$2458518.00730 \pm 0.00049$
T_S…	Time of eclipse (BJD$_{\rm TDB}$)…	$2458515.45789 \pm 0.00049$
T_A…	Time of ascending node (BJD$_{\rm TDB}$)…	$2458521.83142 \pm 0.00049$
T_D…	Time of descending node (BJD$_{\rm TDB}$)…	$2458519.28201 \pm 0.00049$
V_c/V_e…	…	1.00
$M_P \sin i$…	Minimum mass[c] ($M_\oplus$)…	40^{+16}_{-11}
M_P/M_*…	Mass ratio[c]…	$0.00068^{+0.00027}_{-0.00017}$
d/R_*…	Separation at mid transit…	$35.24^{+0.92}_{-1.1}$
P_T…	A priori nongrazing transit prob…	$0.01976^{+0.0010}_{-0.00094}$
$P_{T,G}$…	A priori transit prob…	$0.03708^{+0.0012}_{-0.00098}$
Wavelength Parameters:		B
u_1…	Linear limb-darkening coeff…	$0.98^{+0.55}_{-0.62}$
A_D…	Dilution from neighboring stars…	$0.9817^{+0.0023}_{-0.0012}$

Table C3

(Continued)

Parameter	Units	Values
Transit Parameters:		TESS UT 2019-02-03 (TESS)
F_0…	Baseline flux…	$0.999887^{+0.000062}_{-0.000063}$
C_0…	Additive detrending coeff…	…
M_0…	Multiplicative detrending coeff…	…
M_1…	Multiplicative detrending coeff…	…

Notes. Created using EXOFASTv2, commit number 7971a947. See Table 3 in Eastman et al. (2019) for a detailed description of all parameters.
[a] The metallicity of the star at birth.
[b] Corresponds to static points in a star's evolutionary history. See Section 2 in Dotter (2016).
[c] Uses measured radius and estimated mass from Chen & Kipping (2016).
[d] Time of conjunction is commonly reported as the "transit time."
[e] Time of minimum projected separation is a more correct "transit time."
[f] Optimal time of conjunction minimizes the covariance between T_C and period.
[g] Assumes no albedo and perfect redistribution
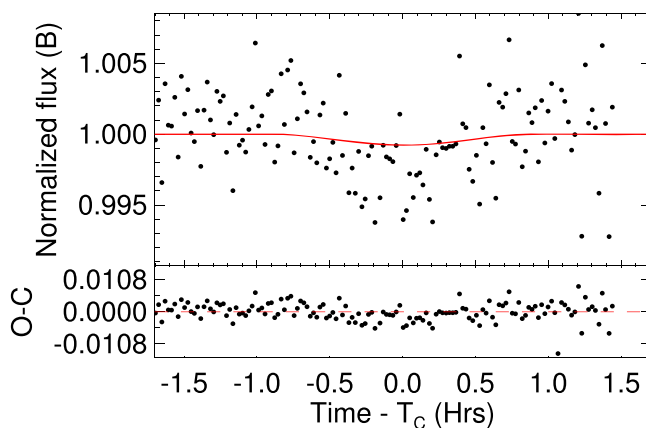
Figure C1. The MCMC transit model for TOI 620 b in the circum-secondary case from EXOFASTv2 in the B band. The model is the red line, and the data are the black points. It is clearly visible that the transit depth in the data is deeper than what the model predicts from the flux dilution of the secondary by the primary. The reduced χ^2 for this model is 9.07.
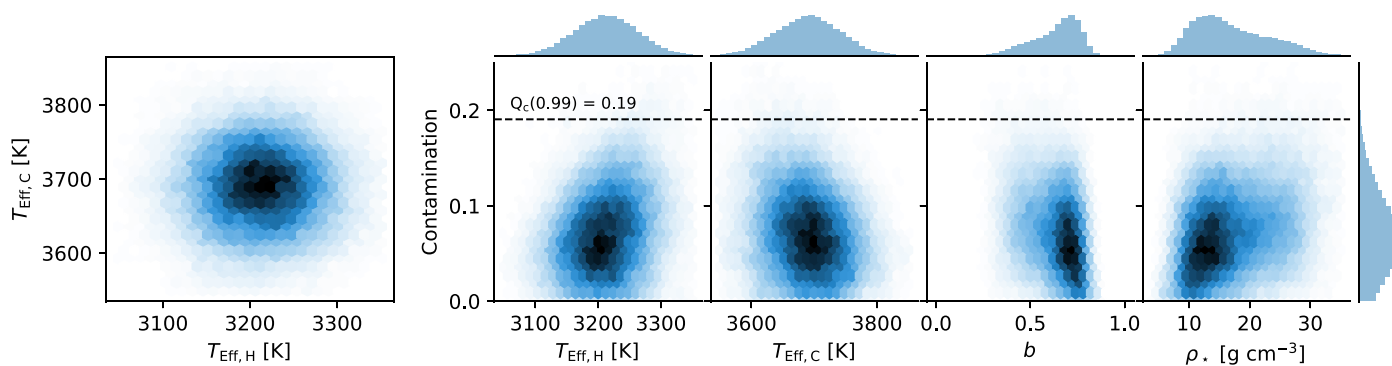
Figure C2. Posteriors and covariances for the circum-secondary MCMC of the MuSCAT2 quad-band transit light curves for a set of model parameters: effective temperature of the host [H] secondary star and contaminant [C] primary star, impact parameter, and host stellar density, plotted against the flux contamination ratio. The upper limit to a flux ratio from the primary contributing 19% of the light to the system rules out the circum-secondary scenario as it is not physically possible to have a bound primary companion that is both hotter and less luminous than the secondary.

Table C4
The Model Parameters and Posterior Distributions used in Our RV Model that Considers the Transiting b Planet as
Circum-secondary and the Linear $\dot{\gamma}$ Trend

Parameter (units)	MAP Value	MCMC Posterior
P_b (days)	5.09881 (Locked)	…
$T_{C,b}$ (days)	2458518.007 (Locked)	…
e_b	0 (Locked)	…
ω_b	0 (Locked)	…
K_b (m s^{-1})	-2.58	$-2.62^{+0.96}_{-0.93}$
γ_{iSHELL} (m s^{-1})	4.11	$4.01^{+2.96}_{-2.94}$
$\gamma_{\text{CARMENES-Vis}}$ (m s^{-1})	-1.63	$-1.65^{+1.58}_{-1.56}$
$\gamma_{\text{CARMENES-NIR}}$ (m s^{-1})	-2.56	$-2.42^{+3.61}_{-3.71}$
γ_{NEID} (m s^{-1})	0.59	$0.64^{+1.16}_{-1.23}$
$\gamma_{\text{MAROON-X-blue}}$ (m s^{-1})	-6.50	$-6.41^{+1.36}_{-1.32}$
$\gamma_{\text{MAROON-X-red}}$ (m s^{-1})	-7.59	$-7.50^{+1.58}_{-1.60}$
σ_{iSHELL} (m s^{-1})	13.14	$13.31^{+1.14}_{-1.05}$
$\sigma_{\text{CARMENES-Vis}}$ (m s^{-1})	2.26	$3.23^{+1.75}_{-1.48}$
$\sigma_{\text{CARMENES-NIR}}$ (m s^{-1})	4.88	$5.10^{+1.84}_{-1.94}$
σ_{NEID} (m s^{-1})	3.69	$4.08^{+1.09}_{-0.94}$
$\sigma_{\text{MAROON-X-blue}}$ (m s^{-1})	1.93	$2.26^{+1.02}_{-0.87}$
$\sigma_{\text{MAROON-X-red}}$ (m s^{-1})	3.17	$3.52^{+0.91}_{-0.71}$
$\dot{\gamma}$ (m s^{-1} day^{-1})	0.08	$0.08^{+0.01}_{-0.01}$

Note. The priors are identical to the circum-primary run except the K_b value is allowed to be negative.
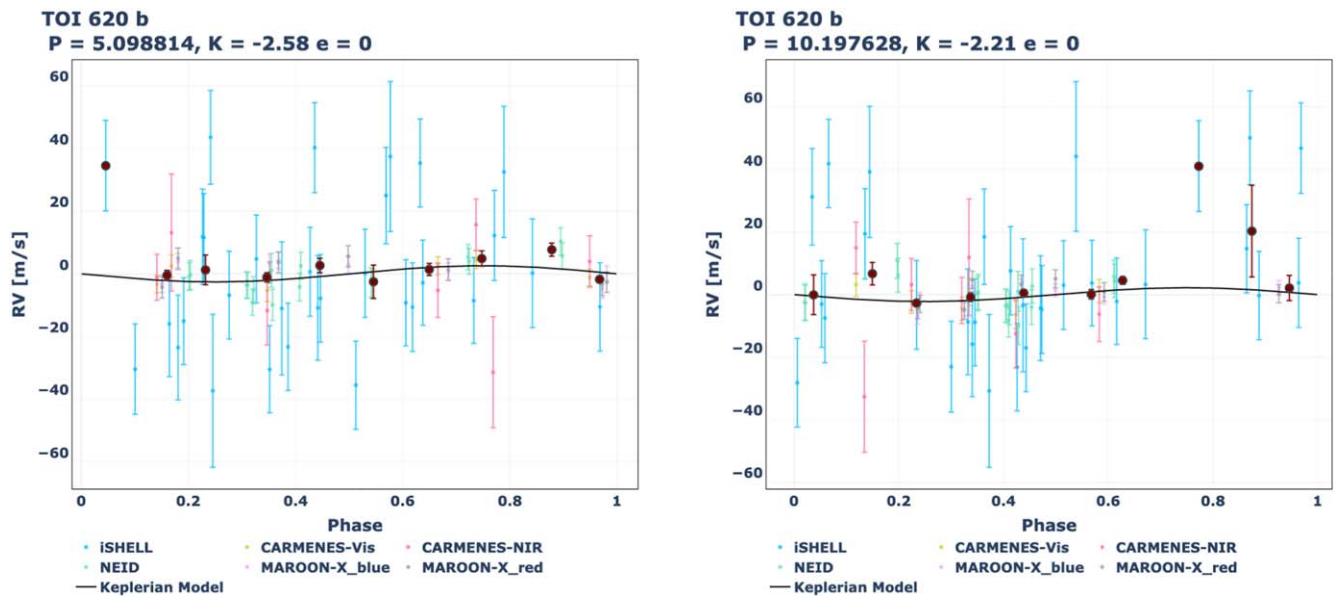
Figure C3. RV time-series plot for the circum-secondary case (left) and HEB case (right) phased to the period of b, with the black model representing the planet's MAP model fit.
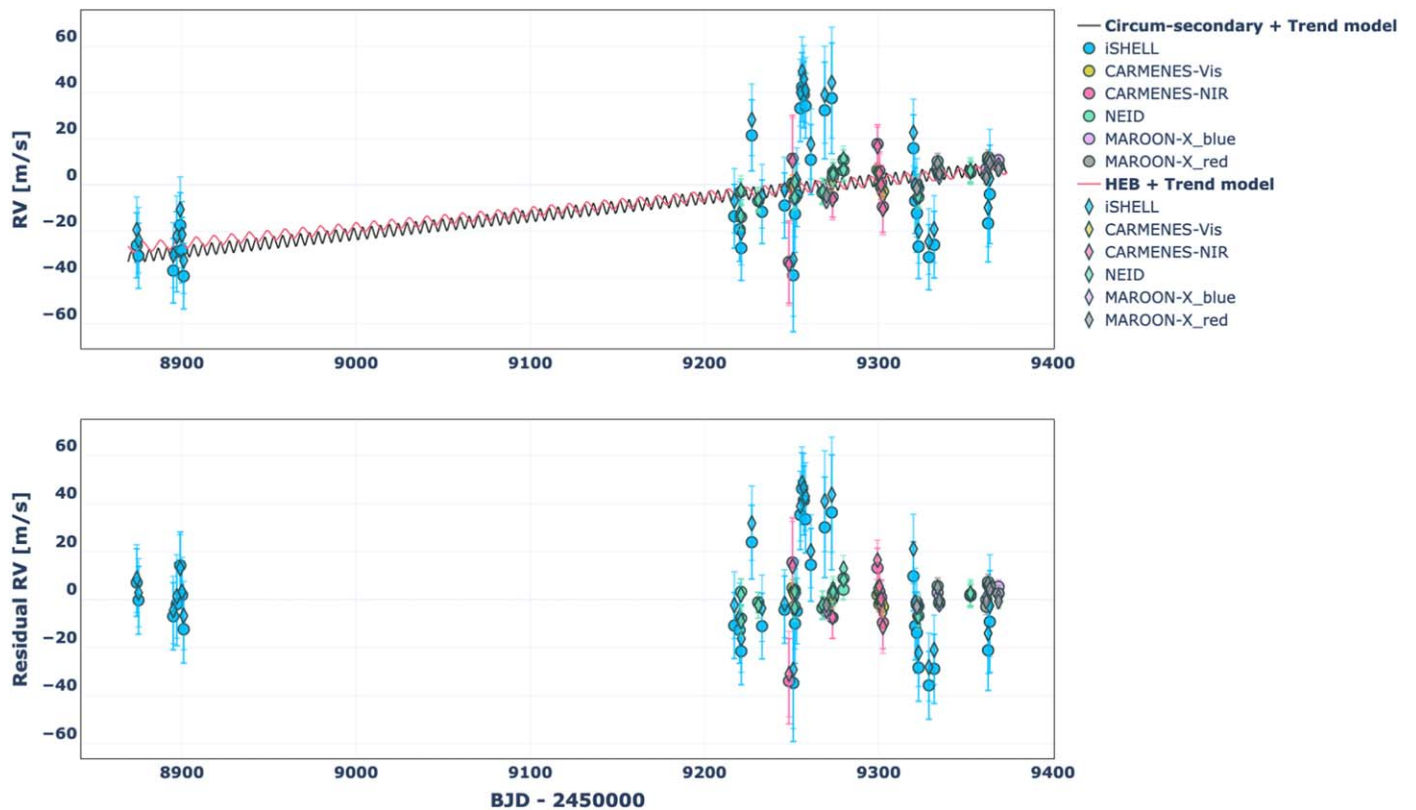
Figure C4. Full RV time-series plot for the circum-secondary and HEB cases, with the black line representing the circum-secondary model and the red line representing the HEB model. The top plot shows the RVs for each instrument and error bars over the full time baseline of observations, while the bottom plot shows the residuals (data – model).

Appendix D
HEB: Analysis & Results, Transit Times, Transit and RV Posteriors, and Full Corner Plots

D.1. Transit Analysis

Here we present additional Figures and Tables relating to the HEB transit models. Table D1 shows the prior distributions, Table D2 shows the transit times, impact parameters, and depths, and Table D3 shows the posterior distributions. Figure D1 shows the HEB MCMC transit model in the B band.

D.2. Radial Velocity Analysis

The analysis of TOI 620's RVs in the circum-secondary case, by allowing a negative K, works equally well for an HEB scenario, and it is difficult to distinguish between the two from RVs alone. However, unique to the HEB scenario is the possibility of the true period being 10.20 days. Our priors are identical to the circum-secondary analysis with the exception of the period being doubled. We obtain nearly identical results, with a recovered negative K_b at 2.4σ significance (Table D4). The RV plots for this scenario are presented in Figures C3 and C4. All posteriors are well behaved and uncorrelated.

Table D1
Prior Probability Distributions for Our EXOFASTv2 MCMC Simulations in the HEB case

Parameter (units)	(P_0), 1	(P_0), 2	(P_0), 3	Priors	Prior Citation
M_* ($M_\odot$)	0.18	0.18	0.18	$\mathcal{U}(0.08, 0.30)$	This work
R_* ($R_\odot$)	0.18	0.18	0.18	$\mathcal{U}(0.08, 0.30)$	This work
T_{eff} (K)	3090	3090	3090	None	This work
A_V (mag)	0	0	0	$\mathcal{U}(P_0, 0.11625)$	Schlafly & Finkbeiner (2011)
ϖ (mas)	30.283	30.283	30.283	$\mathcal{N}(P_0, 0.06117)$	Gaia Collaboration et al. (2018)
[Fe/H]	0	0	0	$\mathcal{N}(0, 1)$	This work
P (days)	5.098831	10.197662	10.197662	$\mathcal{U}(P_0 \pm 10\%)$	Eastman et al. (2019)
T_C (days)	2458518.005713	2458518.005713	2458523.105	$\mathcal{U}(P_0 \pm P/3)$	Eastman et al. (2019)
R_p/R_*	0.88	0.88	0.88	$\mathcal{U}(0.5, 2)$	This work
M_p ($M_\odot$)	0.16	0.16	0.16	$\mathcal{N}(P_0, 0.05)$	This work
Dilute_B	0.991	0.991	0.991	$\mathcal{U}(0.98, 1)$	This work
Dilute_J	0.934	0.934	0.934	$\mathcal{U}(0.86, 1)$	This work
$\mathrm{Dilute}_{g'}$	0.990	0.990	0.990	$\mathcal{U}(0.96, 1)$	This work
$\mathrm{Dilute}_{r'}$	0.982	0.982	0.982	$\mathcal{U}(0.96, 1)$	This work
Dilute_R	0.982	0.982	0.982	$\mathcal{U}(0.96, 1)$	This work
$\mathrm{Dilute}_{i'}$	0.962	0.962	0.962	$\mathcal{U}(0.92, 1)$	This work
$\mathrm{Dilute}_{\mathrm{TESS}}$	0.974	0.974	0.974	$\mathcal{U}(0.94, 1)$	This work
Dilute_I	0.974	0.974	0.974	$\mathcal{U}(0.94, 1)$	This work
$\mathrm{Dilute}_{z'}$	0.942	0.942	0.942	$\mathcal{U}(0.88, 1)$	This work

Note. The starting value P_0 has three columns corresponding to the three cases that were run assuming a 5.09 day period and a 10.19 day period with even and odd transits. $\mathcal{N}(\mu, \sigma)$ signifies a Gaussian prior with mean μ and standard deviation σ. $\mathcal{U}(\ell, r)$ signifies a uniform prior with left bound ℓ and right bound r. A_V is the extinction in the V band, and ϖ is the parallax. Dilute is the fraction of light from from close neighboring targets. Parameters that are missing, including orbital e, ω, are assumed to take default values of circular.

Table D2
Median Values and 68% Confidence Interval for Transit Times, Impact Parameters, and Depths for the HEB Case

Transit	Planet	Epoch	T_T	b	Depth
TESS UT 2019-02-03 (TESS)	b	0	$2458518.00675^{+0.00068}_{-0.00091}$	$1.80^{+0.23}_{-0.13}$	$0.0914^{+0.0020}_{-0.0037}$
TESS UT 2019-02-08 (TESS)	b	1	$2458523.10557^{+0.00068}_{-0.00091}$	$1.80^{+0.23}_{-0.13}$	$0.0914^{+0.0020}_{-0.0037}$
TESS UT 2019-02-13 (TESS)	b	2	$2458528.20438^{+0.00068}_{-0.00089}$	$1.80^{+0.23}_{-0.13}$	$0.0914^{+0.0020}_{-0.0037}$
TESS UT 2019-02-23 (TESS)	b	4	$2458538.40203^{+0.00068}_{-0.00088}$	$1.80^{+0.23}_{-0.13}$	$0.0914^{+0.0020}_{-0.0037}$
NGTS UT 2019-04-20 (R)	b	15	$2458594.48908^{+0.00064}_{-0.00082}$	$1.80^{+0.23}_{-0.13}$	$0.0892^{+0.0042}_{-0.0069}$
LCO UT 2019-04-20 (z')	b	15	$2458594.48908^{+0.00064}_{-0.00082}$	$1.80^{+0.23}_{-0.13}$	$0.0663^{+0.0035}_{-0.0028}$
TMMT UT 2019-04-25 (I)	b	16	$2458599.58791^{+0.00064}_{-0.00082}$	$1.80^{+0.23}_{-0.13}$	$0.0859^{+0.0061}_{-0.0050}$
NGTS UT 2019-06-10 (R)	b	25	$2458645.47730^{+0.00062}_{-0.00076}$	$1.80^{+0.23}_{-0.13}$	$0.0892^{+0.0042}_{-0.0069}$
MuSCAT2 UT 2020-01-16 (g')	b	68	$2458864.72658^{+0.00040}_{-0.00040}$	$1.80^{+0.23}_{-0.13}$	$0.0824^{+0.011}_{-0.0074}$
MuSCAT2 UT 2020-01-16 (i')	b	68	$2458864.72658^{+0.00047}_{-0.00040}$	$1.80^{+0.23}_{-0.13}$	$0.0821^{+0.0071}_{-0.0073}$
MuSCAT2 UT 2020-01-16 (r')	b	68	$2458864.72658^{+0.00047}_{-0.00040}$	$1.80^{+0.23}_{-0.13}$	$0.0913^{+0.0066}_{-0.010}$
MuSCAT2 UT 2020-01-16 (z')	b	68	$2458864.72658^{+0.00047}_{-0.00040}$	$1.80^{+0.23}_{-0.13}$	$0.0663^{+0.0035}_{-0.0028}$
KeplerCam UT 2020-01-26 (B)	b	70	$2458874.92422^{+0.00046}_{-0.00039}$	$1.80^{+0.23}_{-0.13}$	$0.0831^{+0.0052}_{-0.0074}$
MuSCAT2 UT 2020-03-02 (g')	b	77	$2458910.61595^{+0.00048}_{-0.00036}$	$1.80^{+0.23}_{-0.13}$	$0.0824^{+0.011}_{-0.0074}$
MuSCAT2 UT 2020-03-02 (i')	b	77	$2458910.61595^{+0.00048}_{-0.00036}$	$1.80^{+0.23}_{-0.13}$	$0.0821^{+0.0071}_{-0.0073}$
MuSCAT2 UT 2020-03-02 (r')	b	77	$2458910.61595^{+0.00048}_{-0.00036}$	$1.80^{+0.23}_{-0.13}$	$0.0913^{+0.0066}_{-0.010}$
MuSCAT2 UT 2020-03-02 (z')	b	77	$2458910.61595^{+0.00048}_{-0.00036}$	$1.80^{+0.23}_{-0.13}$	$0.0663^{+0.0035}_{-0.0028}$
MuSCAT2 UT 2020-04-16 (g')	b	86	$2458956.50536^{+0.00044}_{-0.00034}$	$1.80^{+0.23}_{-0.13}$	$0.0824^{+0.011}_{-0.0074}$
MuSCAT2 UT 2020-04-16 (i')	b	86	$2458956.50536^{+0.00044}_{-0.00034}$	$1.80^{+0.23}_{-0.13}$	$0.0821^{+0.0071}_{-0.0073}$
MuSCAT2 UT 2020-04-16 (r')	b	86	$2458956.50536^{+0.00044}_{-0.00034}$	$1.80^{+0.23}_{-0.13}$	$0.0913^{+0.0066}_{-0.010}$
MuSCAT2 UT 2020-04-16 (z')	b	86	$2458956.50536^{+0.00044}_{-0.00034}$	$1.80^{+0.23}_{-0.13}$	$0.0663^{+0.0035}_{-0.0028}$
LCRO UT 2020-11-27 (i')	b	130	$2459180.85360^{+0.00036}_{-0.00044}$	$1.80^{+0.23}_{-0.13}$	$0.0821^{+0.0071}_{-0.0073}$
MuSCAT2 UT 2021-01-07 (i')	b	138	$2459221.64421^{+0.00031}_{-0.00048}$	$1.80^{+0.23}_{-0.13}$	$0.0821^{+0.0071}_{-0.0073}$
MuSCAT2 UT 2021-01-07 (r')	b	138	$2459221.64421^{+0.00031}_{-0.00048}$	$1.80^{+0.23}_{-0.13}$	$0.0913^{+0.0066}_{-0.010}$
MuSCAT2 UT 2021-01-07 (z')	b	138	$2459221.64421^{+0.00031}_{-0.00048}$	$1.80^{+0.23}_{-0.13}$	$0.0663^{+0.0035}_{-0.0028}$
TESS UT 2021-02-11 (TESS)	b	145	$2459257.33598^{+0.00027}_{-0.00049}$	$1.80^{+0.23}_{-0.13}$	$0.0914^{+0.0020}_{-0.0037}$
TESS UT 2021-02-16 (TESS)	b	146	$2459262.43481^{+0.00025}_{-0.00050}$	$1.80^{+0.23}_{-0.13}$	$0.0914^{+0.0020}_{-0.0037}$
TESS UT 2021-02-27 (TESS)	b	148	$2459272.63244^{+0.00026}_{-0.00049}$	$1.80^{+0.23}_{-0.13}$	$0.0914^{+0.0020}_{-0.0037}$
ExTrA UT 2021-03-04 (J)	b	149	$2459277.73127^{+0.00027}_{-0.00048}$	$1.80^{+0.23}_{-0.13}$	$0.0604^{+0.0033}_{-0.0039}$
TESS UT 2021-03-04 (TESS)	b	149	$2459277.73127^{+0.00027}_{-0.00048}$	$1.80^{+0.23}_{-0.13}$	$0.0914^{+0.0020}_{-0.0037}$
ExTrA UT 2021-04-13 (J)	b	157	$2459318.52183^{+0.00032}_{-0.00048}$	$1.80^{+0.23}_{-0.13}$	$0.0604^{+0.0033}_{-0.0039}$
ExTrA UT 2021-04-19 (J)	b	158	$2459323.62066^{+0.00031}_{-0.00048}$	$1.80^{+0.23}_{-0.13}$	$0.0604^{+0.0033}_{-0.0039}$
ExTrA UT 2021-06-03 (J)	b	167	$2459369.51006^{+0.00031}_{-0.00049}$	$1.80^{+0.23}_{-0.13}$	$0.0604^{+0.0033}_{-0.0039}$

Table D3
Median Values and 68% Confidence Interval for the HEB Case, Created using EXOFASTv2 Commit Number 7971a947

Parameter	Units	Values
Stellar Parameters:		
M_*…	Mass ($M_\odot$)…	$0.151^{+0.076}_{-0.021}$
R_*…	Radius ($R_\odot$)…	0.278 ± 0.012
L_*…	Luminosity ($L_\odot$)…	$0.0077^{+0.0072}_{-0.0026}$
ρ_*…	Density (cgs)…	$10.0^{+3.3}_{-1.6}$
$\log g$…	Surface gravity (cgs)…	$4.726^{+0.14}_{-0.056}$
$T_{\rm eff}$…	Effective temperature (K)…	3260^{+490}_{-360}
[Fe/H]…	Metallicity (dex)…	$-0.21^{+0.38}_{-0.49}$
$[{\rm Fe/H}]_0$…	Initial metallicity[a]…	$-0.30^{+0.44}_{-0.39}$
Age…	Age (Gyr)…	$0.058^{+0.057}_{-0.013}$
EEP…	Equal evolutionary phase[b]…	$152^{+18}_{-10.}$
Planetary Parameters:		b
P…	Period (days)…	$5.0988228^{+0.0000061}_{-0.0000068}$
R_P…	Radius ($R_\oplus$)…	$35.0^{+8.0}_{-3.4}$
M_P…	Predicted mass ($M_\oplus$)…	41100^{+14000}_{-9400}
T_C…	Time of conjunction[c] ($\rm BJD_{TDB}$)…	$2458518.00675^{+0.00068}_{-0.00091}$
T_T…	Time of minimum projected separation[d] ($\rm BJD_{TDB}$)…	$2458518.00675^{+0.00068}_{-0.00091}$
T_0…	Optimal conjunction Time[e] ($\rm BJD_{TDB}$)…	$2459032.98773^{+0.00035}_{-0.00037}$
a…	Semimajor axis (au)…	$0.0380^{+0.0035}_{-0.0023}$
i…	Inclination (Degrees)…	$86.45^{+0.28}_{-0.27}$
$T_{\rm eq}$…	Equilibrium temperature[f] (K)…	423^{+61}_{-47}
$\tau_{\rm circ}$…	Tidal circularization timescale (Gyr)…	$1.61^{+0.71}_{-0.99}$
K…	RV semiamplitude (m/s)…	35900^{+7000}_{-7200}
R_P/R_*…	Radius of planet in stellar radii…	$1.18^{+0.22}_{-0.11}$
a/R_*…	Semimajor axis in stellar radii…	$29.6^{+1.7}_{-1.2}$
δ…	$(R_P/R_*)^2$…	$1.39^{+0.57}_{-0.25}$
$\delta_{\rm B}$…	Transit depth in B (fraction)…	$0.066^{+0.028}_{-0.026}$
$\delta_{\rm I}$…	Transit depth in I (fraction)…	$0.083^{+0.011}_{-0.021}$
$\delta_{\rm J}$…	Transit depth in J (fraction)…	$-0.39^{+0.17}_{-0.46}$
$\delta_{\rm R}$…	Transit depth in R (fraction)…	$0.082^{+0.012}_{-0.014}$
$\delta_{g'}$…	Transit depth in g' (fraction)…	$0.072^{+0.017}_{-0.038}$
$\delta_{i'}$…	Transit depth in i' (fraction)…	$0.071^{+0.021}_{-0.045}$
$\delta_{r'}$…	Transit depth in r' (fraction)…	$0.0921^{+0.0075}_{-0.018}$
$\delta_{z'}$…	Transit depth in z' (fraction)…	$-0.112^{+0.067}_{-0.27}$
$\delta_{\rm TESS}$…	Transit depth in TESS (fraction)…	$0.0933^{+0.0050}_{-0.0089}$
τ…	Ingress/egress transit duration (days)…	$0.03393^{+0.00097}_{-0.0010}$
T_{14}…	Total transit duration (days)…	$0.0679^{+0.0019}_{-0.0021}$
$T_{\rm FWHM}$…	FWHM transit duration (days)…	$0.03393^{+0.00097}_{-0.0010}$
b…	Transit impact parameter…	$1.80^{+0.23}_{-0.13}$
$\delta_{S,2.5\mu m}$…	Blackbody eclipse depth at 2.5 μm (ppm)…	$8.2^{+35}_{-5.9}$
$\delta_{S,5.0\mu m}$…	Blackbody eclipse depth at 5.0 μm (ppm)…	2100^{+3500}_{-990}
$\delta_{S,7.5\mu m}$…	Blackbody eclipse depth at 7.5 μm (ppm)…	11600^{+12000}_{-3400}
ρ_P…	Density (cgs)…	$5.1^{+1.5}_{-1.9}$
$\log g_P$…	Surface gravity…	$4.505^{+0.064}_{-0.12}$
Θ…	Safronov number…	$19.9^{+6.9}_{-5.6}$
$\langle F \rangle$…	Incident flux (10^9 erg s^{-1} cm^{-2})…	$0.0073^{+0.0052}_{-0.0027}$
T_P…	Time of periastron ($\rm BJD_{TDB}$)…	$2458518.00675^{+0.00068}_{-0.00091}$
T_S…	Time of eclipse ($\rm BJD_{TDB}$)…	$2458515.45733^{+0.00068}_{-0.00091}$
T_A…	Time of ascending node ($\rm BJD_{TDB}$)…	$2458521.83086^{+0.00068}_{-0.00091}$
T_D…	Time of descending node ($\rm BJD_{TDB}$)…	$2458519.28145^{+0.00068}_{-0.00091}$
V_c/V_e…	…	1.00
$M_P \sin i$…	Minimum mass ($M_\oplus$)…	41000^{+14000}_{-9400}
M_P/M_*…	Mass ratio…	$0.76^{+0.35}_{-0.19}$
d/R_*…	Separation at mid transit…	$29.6^{+1.7}_{-1.2}$
P_T…	A priori nongrazing transit prob…	$-0.0061^{+0.0039}_{-0.0070}$
$P_{T,G}$…	A priori transit prob…	$0.0747^{+0.0041}_{-0.0040}$
Wavelength Parameters:		B
u_1…	Linear limb-darkening coeff…	$0.70^{+0.25}_{-0.50}$

Table D3
(Continued)

Parameter	Units	Values
Transit Parameters:		TESS UT 2019-02-03 (TESS)
σ^2…	Added variance…	$-0.000000386^{+0.00000010}_{-0.000000073}$
F_0…	Baseline flux…	$0.999914^{+0.000042}_{-0.000087}$
C_0…	Additive detrending coeff…	…
M_0…	Multiplicative detrending coeff…	…
M_1…	Multiplicative detrending coeff…	…

Notes. See Table 3 in Eastman et al. (2019) for a detailed description of all parameters.
[a] The metallicity of the star at birth.
[b] Corresponds to static points in a star's evolutionary history. See Section 2 in Dotter (2016).
[c] Time of conjunction is commonly reported as the "transit time."
[d] Time of minimum projected separation is a more correct "transit time."
[e] Optimal time of conjunction minimizes the covariance between T_C and period.
[f] Assumes no albedo and perfect redistribution.
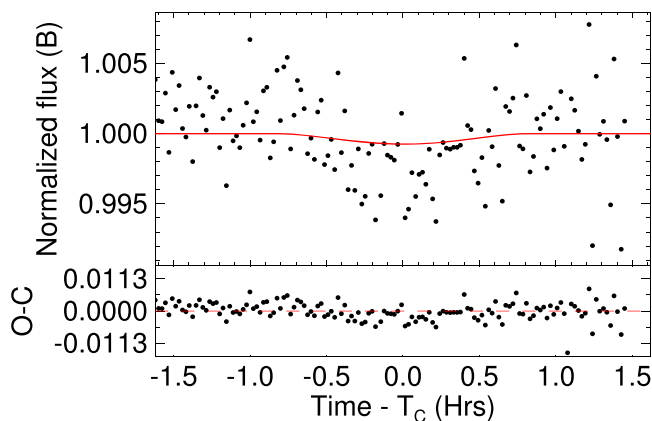
Figure D1. The MCMC transit model for TOI 620 b in the HEB case from `EXOFASTv2` in the B band. The model is the red line, and the data are the black points. It is clearly visible that the transit depth in the data is deeper than what the model predicts from the flux dilution of the secondary by the primary. The reduced χ^2 for this model is 9.28.

Table D4
The Model Parameters and Posterior Distributions used in Our RV Model that Considers the Transiting b Planet as an HEB and the Linear $\dot\gamma$ Trend

Parameter (units)	MAP Value	MCMC Posterior
P_b (days)	10.19762 (Locked)	…
$T_{C,b}$ (days)	2458518.007 (Locked)	…
e_b	0 (Locked)	…
ω_b	0 (Locked)	…
K_b (m s^{-1})	-2.21	$-2.48^{+0.96}_{-0.95}$
γ_{iSHELL} (m s^{-1})	-2.62	$4.12^{+2.90}_{-3.01}$
$\gamma_{\mathrm{CARMENES-Vis}}$ (m s^{-1})	-0.11	$-0.06^{+1.89}_{-2.02}$
$\gamma_{\mathrm{CARMENES-NIR}}$ (m s^{-1})	-1.51	$-0.61^{+3.86}_{-3.81}$
γ_{NEID} (m s^{-1})	0.20	$0.88^{+1.41}_{-1.48}$
$\gamma_{\mathrm{MAROON-X-blue}}$ (m s^{-1})	-4.43	$-5.09^{+1.21}_{-1.21}$
$\gamma_{\mathrm{MAROON-X-red}}$ (m s^{-1})	-6.43	$-7.00^{+1.50}_{-1.50}$
σ_{iSHELL} (m s^{-1})	13.24	$13.17^{+1.14}_{-1.08}$
$\sigma_{\mathrm{CARMENES-Vis}}$ (m s^{-1})	3.36	$4.07^{+1.54}_{-1.30}$
$\sigma_{\mathrm{CARMENES-NIR}}$ (m s^{-1})	5.00	$5.48^{+1.08}_{-0.93}$
σ_{NEID} (m s^{-1})	5.00	$5.14^{+1.08}_{-0.93}$
$\sigma_{\mathrm{MAROON-X-blue}}$ (m s^{-1})	1.00	$1.21^{+1.03}_{-0.80}$
$\sigma_{\mathrm{MAROON-X-red}}$ (m s^{-1})	2.68	$3.11^{+0.86}_{-0.66}$
$\dot\gamma$ (m s^{-1} day^{-1})	0.07	$0.08^{+0.01}_{-0.01}$

Note. The priors are identical to the circum-secondary run except the P_b value is locked at twice the TESS period.

Appendix E
Radial Velocity Table

Table E1 shows our full set of radial velocities and errors from all instruments used in this analysis.
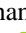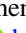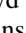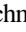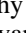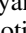
Table E1
A Full List of the RV Values, Times, and Errors Used in this Paper

BJD$_{TDB}$ (days)	RV (m s^{-1})	Error (m s^{-1})	Instrument	Offset[a] (m s^{-1})	Offset Error[a] (m s^{-1})
2458874.042603…	−22.03…	4.96…	iSHELL	…	…
2458875.075875…	−26.54…	5.03…	iSHELL	…	…
2458895.047871…	−32.99…	4.71…	iSHELL	…	…
2458897.065268…	−24.80…	11.31…	iSHELL	…	…
2458899.036716…	−13.29…	4.83…	iSHELL	…	…
2458900.046926…	−24.11…	5.34…	iSHELL	…	…
2458901.022179…	−35.33…	5.21…	iSHELL	…	…
2459217.085069…	−9.48…	4.07…	iSHELL	…	…
2459220.070212…	−15.13…	4.32…	iSHELL	…	…
2459220.905235…	−2.32…	3.95…	NEID	…	…
2459220.915972…	−13.34…	3.31…	NEID	…	…
2459221.062629…	−23.22…	4.63…	iSHELL	…	…
2459227.095393…	25.50…	7.97…	iSHELL	…	…
2459230.866622…	−6.31…	1.94…	NEID	…	…
2459230.877358…	−6.31…	2.06…	NEID	…	…
2459233.027990…	−7.54…	3.89…	iSHELL	…	…
2459245.996343…	−4.82…	4.87…	iSHELL	…	…
2459248.508540…	−35.88…	17.06…	CARMENES-NIR	…	…
2459250.546740…	8.82…	18.00…	CARMENES-NIR	…	…
2459250.546800…	−0.89…	2.73…	CARMENES-Vis	…	…
2459250.939338…	−34.97…	20.55…	iSHELL	…	…
2459251.765798…	−5.28…	2.41…	NEID	…	…
2459251.776534…	1.46…	2.20…	NEID	…	…
2459251.940203…	−8.45…	10.23…	iSHELL	…	…
2459252.938448…	−0.33…	3.46…	iSHELL	…	…
2459255.020459…	37.18…	5.89…	iSHELL	…	…
2459256.017137…	46.30…	7.11…	iSHELL	…	…
2459257.009042…	43.08…	5.83…	iSHELL	…	…
2459258.011730…	38.23…	4.90…	iSHELL	…	…
2459261.040202…	14.99…	7.52…	iSHELL	…	…
2459267.742876…	−2.67…	3.09…	NEID	…	…
2459267.753612…	−2.82…	2.54…	NEID	…	…
2459269.006339…	36.29…	16.24…	iSHELL	…	…
2459269.942464…	−11.47…	2.51…	MAROON-X blue	−1.5…	0.5…
2459269.942464…	−11.20…	1.77…	MAROON-X red	−2.0…	0.5…
2459273.024693…	41.53…	19.96…	iSHELL	…	…
2459273.476340…	0.95…	1.70…	CARMENES-Vis	…	…
2459273.476430…	−7.83…	7.20…	CARMENES-NIR	…	…
2459273.764119…	5.94…	1.68…	NEID	…	…
2459273.774855…	4.61…	1.90…	NEID	…	…
2459279.744662…	11.40…	2.38…	NEID	…	…
2459279.758946…	6.76…	1.99…	NEID	…	…
2459299.334560…	4.82…	1.67…	CARMENES-Vis	…	…
2459299.334360…	15.12…	6.62…	CARMENES-NIR	…	…
2459300.414680…	3.48…	6.62…	CARMENES-NIR	…	…
2459300.415170…	−0.68…	1.38…	CARMENES-Vis	…	…
2459301.395920…	−1.51…	5.45…	CARMENES-NIR	…	…
2459301.396090…	−2.75…	1.66…	CARMENES-Vis	…	…
2459302.446160…	−12.04…	9.77…	CARMENES-NIR	…	…
2459302.446330…	−4.59…	2.81…	CARMENES-Vis	…	…
2459319.904094…	19.94…	5.76…	iSHELL	…	…
2459320.909564…	−2.78…	5.12…	iSHELL	…	…
2459321.840076…	−5.94…	1.93…	MAROON-X blue	0.0…	0.0…
2459321.840076…	−8.10…	1.26…	MAROON-X red	0.0…	0.0…
2459321.909542…	−8.14…	10.57…	iSHELL	…	…
2459322.701506…	−4.73…	1.99…	NEID	…	…
2459322.712242…	−0.73…	2.12…	NEID	…	…

Table E1
(Continued)

BJD$_{\text{TDB}}$ (days)	RV (m s^{-1})	Error (m s^{-1})	Instrument	Offset[a] (m s^{-1})	Offset Error[a] (m s^{-1})
2459322.864615…	−22.52…	4.54…	iSHELL	…	…
2459328.783324…	−27.13…	5.02…	iSHELL	…	…
2459331.781398…	−21.77…	5.93…	iSHELL	…	…
2459333.810183…	1.01…	1.71…	MAROON-X blue	0.0…	0.0…
2459333.810183…	2.66…	1.09…	MAROON-X red	0.0…	0.0…
2459334.761529…	−1.08…	1.93…	MAROON-X blue	0.0…	0.0…
2459334.761529…	−1.46…	1.28…	MAROON-X red	0.0…	0.0…
2459352.691482…	5.86…	2.41…	NEID	…	…
2459352.702216…	6.37…	2.71…	NEID	…	…
2459361.765208…	0.49…	1.29…	MAROON-X blue	2.0…	1.0…
2459361.765208…	−3.45…	0.80…	MAROON-X red	2.5…	1.0…
2459362.784009…	−12.48…	10.33…	iSHELL	…	…
2459362.784227…	4.28…	1.80…	MAROON-X blue	2.0…	1.0…
2459362.784227…	4.29…	0.74…	MAROON-X red	2.5…	1.0…
2459363.739140…	4.71…	1.70…	MAROON-X blue	2.0…	1.0…
2459363.739140…	3.03…	1.00…	MAROON-X red	2.5…	1.0…
2459363.770313…	0.04…	16.68…	iSHELL	…	…
2459368.754018…	4.11…	2.17…	MAROON-X blue	2.0…	1.0…
2459368.754018…	0.24…	1.05…	MAROON-X red	2.5…	1.0…

Note.
[a] See explanation for the offset and offset error in Section 2.3.3.

ORCID iDs

Michael A. Reefe ⬤ https://orcid.org/0000-0003-4701-8497
Rafael Luque ⬤ https://orcid.org/0000-0002-4671-2957
Eric Gaidos ⬤ https://orcid.org/0000-0002-5258-6846
Corey Beard ⬤ https://orcid.org/0000-0001-7708-2364
Peter P. Plavchan ⬤ https://orcid.org/0000-0002-8864-1667
Bryson L. Cale ⬤ https://orcid.org/0000-0001-6279-0595
Enric Palle ⬤ https://orcid.org/0000-0003-0987-1593
Hannu Parviainen ⬤ https://orcid.org/0000-0001-5519-1391
Dax L. Feliz ⬤ https://orcid.org/0000-0002-2457-7889
Jason Eastman ⬤ https://orcid.org/0000-0003-3773-5142
Keivan Stassun ⬤ https://orcid.org/0000-0002-3481-9052
Jonathan Gagné ⬤ https://orcid.org/0000-0002-2592-9612
Jon M. Jenkins ⬤ https://orcid.org/0000-0002-4715-9460
Patricia T. Boyd ⬤ https://orcid.org/0000-0003-0442-4284
Karen A. Collins ⬤ https://orcid.org/0000-0001-6588-9574
William Fong ⬤ https://orcid.org/0000-0003-0241-2757
Natalia Guerrero ⬤ https://orcid.org/0000-0002-5169-9427
Jose-Manuel Almenara-Villa ⬤ https://orcid.org/0000-0003-3208-9815
Jacob Bean ⬤ https://orcid.org/0000-0003-4733-6532
Charles A. Beichman ⬤ https://orcid.org/0000-0002-5627-5471
John Berberian ⬤ https://orcid.org/0000-0003-1466-8389
Allyson Bieryla ⬤ https://orcid.org/0000-0001-6637-5401
Xavier Bonfils ⬤ https://orcid.org/0000-0001-9003-8894
François Bouchy ⬤ https://orcid.org/0000-0002-7613-393X
Edward M. Bryant ⬤ https://orcid.org/0000-0001-7904-4441
Luca Cacciapuoti ⬤ https://orcid.org/0000-0001-8266-0894
Caleb I. Cañas ⬤ https://orcid.org/0000-0003-4835-0619
David R. Ciardi ⬤ https://orcid.org/0000-0002-5741-3047
Kevin I. Collins ⬤ https://orcid.org/0000-0003-2781-3207
Ian J. M. Crossfield ⬤ https://orcid.org/0000-0002-1835-1891
Courtney D. Dressing ⬤ https://orcid.org/0000-0001-8189-0233
Philipp Eigmüller ⬤ https://orcid.org/0000-0003-4096-0594
Mohammed El Mufti ⬤ https://orcid.org/0000-0001-8364-2903
Emma Esparza-Borges ⬤ https://orcid.org/0000-0002-2341-3233
Akihiko Fukui ⬤ https://orcid.org/0000-0002-4909-5763
Peter Gao ⬤ https://orcid.org/0000-0002-8518-9601
Claire Geneser ⬤ https://orcid.org/0000-0001-9596-8820
Crystal L. Gnilka ⬤ https://orcid.org/0000-0003-2519-6161
Erica Gonzales ⬤ https://orcid.org/0000-0002-9329-2190
Arvind F. Gupta ⬤ https://orcid.org/0000-0002-5463-9980
Sam Halverson ⬤ https://orcid.org/0000-0003-1312-9391
Fred Hearty ⬤ https://orcid.org/0000-0002-1664-3102
Steve B. Howell ⬤ https://orcid.org/0000-0002-2532-2853
Shubham Kanodia ⬤ https://orcid.org/0000-0001-8401-4300
David Kasper ⬤ https://orcid.org/0000-0003-0534-6388
Takanori Kodama ⬤ https://orcid.org/0000-0001-9032-5826
Veselin Kostov ⬤ https://orcid.org/0000-0001-9786-1031
David W. Latham ⬤ https://orcid.org/0000-0001-9911-7388
Monika Lendl ⬤ https://orcid.org/0000-0001-9699-1459
Andrea Lin ⬤ https://orcid.org/0000-0002-9082-6337
John H. Livingston ⬤ https://orcid.org/0000-0002-4881-3620
Jack Lubin ⬤ https://orcid.org/0000-0001-8342-7736
Suvrath Mahadevan ⬤ https://orcid.org/0000-0001-9596-7983
Rachel Matson ⬤ https://orcid.org/0000-0001-7233-7508
Elisabeth Matthews ⬤ https://orcid.org/0000-0003-0593-1560
Felipe Murgas ⬤ https://orcid.org/0000-0001-9087-1245
Norio Narita ⬤ https://orcid.org/0000-0001-8511-2981
Patrick Newman ⬤ https://orcid.org/0000-0003-3848-3418
Joe Ninan ⬤ https://orcid.org/0000-0001-8720-5612
Ares Osborn ⬤ https://orcid.org/0000-0002-5899-7750
Samuel N. Quinn ⬤ https://orcid.org/0000-0002-8964-8377
Paul Robertson ⬤ https://orcid.org/0000-0003-0149-9678
Arpita Roy ⬤ https://orcid.org/0000-0001-8127-5775
Joshua Schlieder ⬤ https://orcid.org/0000-0001-5347-7062
Christian Schwab ⬤ https://orcid.org/0000-0002-0091-7105
Andreas Seifahrt ⬤ https://orcid.org/0000-0003-4526-3747
Guðmundur Stefánsson ⬤ https://orcid.org/0000-0001-7409-5688
Daniel Stevens ⬤ https://orcid.org/0000-0002-5951-8328
Julian Stürmer ⬤ https://orcid.org/0000-0002-4410-4712

Angelle Tanner ● https://orcid.org/0000-0002-2903-2140
Ryan Terrien ● https://orcid.org/0000-0002-4788-8858
David Vermilion ● https://orcid.org/0000-0002-4501-564X
Sharon X. Wang ● https://orcid.org/0000-0002-6937-9034
Justin Wittrock ● https://orcid.org/0000-0002-7424-9891
Jason T. Wright ● https://orcid.org/0000-0001-6160-5888
Mathias Zechmeister ● https://orcid.org/0000-0002-6532-4378
Farzaneh Zohrabi ● https://orcid.org/0000-0003-2872-9883

References

Addison, B. C., Wright, D. J., Nicholson, B. A., et al. 2021, MNRAS, 502, 3704

Aigrain, S., Pont, F., & Zucker, S. 2012, MNRAS, 419, 3147

Akaike, H. 1974, ITAC, 19, 716

Akeson, R. L., Chen, X., Ciardi, D., et al. 2013, PASP, 125, 989

Allart, R., Bourrier, V., Lovis, C., et al. 2018, Sci, 362, 1384

Aller, A., Lillo-Box, J., Jones, D., Miranda, L. F., & Barceló Forteza, S. 2020, A&A, 635, A128

Anglada-Escudé, G., & Butler, R. P. 2012, ApJS, 200, 15

Anglada-Escudé, G., Plavchan, P., Mills, S., et al. 2012, PASP, 124, 586

Barbary, K. 2016, JOSS, 1, 58

Batalha, N., Lewis, T., Fortney, J., et al. 2019, ApJL, 885, L25

Beichman, C. A., & Greene, T. P. 2018, in Handbook of Exoplanets, ed. H. J. Deeg & J. A. Belmonte (Cham: Springer), 85

Belokurov, V., Penoyre, Z., Oh, S., et al. 2020, MNRAS, 496, 1922

Bertin, E., & Arnouts, S. 1996, A&AS, 117, 393

Bitsch, B., Raymond, S. N., & Izidoro, A. 2019, A&A, 624, A109

Bluhm, P., Luque, R., Espinoza, N., et al. 2020, A&A, 639, A132

Boller, T., Freyberg, M. J., Trümper, J., et al. 2016, A&A, 588, A103

Bonfils, X., Almenara, J. M., Jocou, L., et al. 2015, Proc. SPIE, 9605, 96051L

Borucki, W. J., Koch, D. G., Basri, G., et al. 2011, ApJ, 736, 19

Brahm, R., Nielsen, L. D., Wittenmyer, R. A., et al. 2020, AJ, 160, 235

Brandeker, A., & Cataldi, G. 2019, A&A, 621, A86

Brown, T. M., Baliber, N., Bianco, F. B., et al. 2013, PASP, 125, 1031

Bryant, E. M., Bayliss, D., McCormac, J., et al. 2020, MNRAS, 494, 5872

Buchhave, L. A., Bakos, G. Á., Hartman, J. D., et al. 2010, ApJ, 720, 1118

Burnham, K. P., & Anderson, D. R. 2002, Model Selection and Multimodel Inference (Berlin: Springer)

Cale, B., Plavchan, P., LeBrun, D., et al. 2019, AJ, 158, 170

Cale, B., Reefe, M., Plavchan, P., et al. 2021, AJ, 162, 295

Chen, G., Casasayas-Barris, N., Pallé, E., et al. 2020, A&A, 642, A54

Chen, G., Pallé, E., Welbanks, L., et al. 2018, A&A, 616, A145

Chen, J., & Kipping, D. 2016, ApJ, 834, 17

Choi, J., Dotter, A., Conroy, C., et al. 2016, ApJ, 823, 102

Ciardi, D. R., Beichman, C. A., Horch, E. P., & Howell, S. B. 2015, ApJ, 805, 16

Collins, K. A., Kielkopf, J. F., Stassun, K. G., & Hessman, F. V. 2017, AJ, 153, 77

Curtis, J. L., Agüeros, M. A., Matt, S. P., et al. 2020, ApJ, 904, 140

Deming, D. L., Wilkins, A. N., McCullough, P. R., et al. 2013, ApJ, 774, 95

Ding, P.-J., Zhu, Z., & Liu, J.-C. 2019, RAA, 19, 068

Dotter, A. 2016, ApJS, 222, 8

Dreizler, S., Crossfield, I. J. M., Kossakowski, D., et al. 2020, A&A, 644, A127

Duchêne, G., & Kraus, A. 2013, ARA&A, 51, 269

Dumusque, X., Santos, N. C., Udry, S., Lovis, C., & Bonfils, X. 2011, A&A, 527, A82

Dumusque, X., Udry, S., Lovis, C., Santos, N. C., & Monteiro, M. J. P. F. G. 2010, A&A, 525, A140

Eastman, J., Gaudi, B. S., & Agol, E. 2013, PASP, 125, 83

Eastman, J. D., Rodriguez, J. E., Agol, E., et al. 2019, arXiv:1907.09480

Ehrenreich, D., Bourrier, V., Wheatley, P. J., et al. 2015, Natur, 522, 459

Fernandes, R. B., Mulders, G. D., Pascucci, I., Mordasini, C., & Emsenhuber, A. 2019, ApJ, 874, 81

Fischer, D. A., Anglada-Escude, G., Arriagada, P., et al. 2016, PASP, 128, 066001

Foreman-Mackey, D. 2016, JOSS, 1, 24

Foreman-Mackey, D., Hogg, D. W., Lang, D., & Goodman, J. 2013, PASP, 125, 306

Foreman-Mackey, D., Price-Whelan, A., Vousden, W., et al. 2020, dfm/corner.py, 2.1.0.rc1, Zenodo, doi:10.5281/zenodo.3937526

Fulton, B. J., Petigura, E. A., Blunt, S., & Sinukoff, E. 2018, PASP, 130, 044504

Fulton, B. J., Petigura, E. A., Howard, A. W., et al. 2017, AJ, 154, 109

Fűrész, G. 2008, PhD thesis, University of Szeged, Hungary, http://www.sao.arizona.edu/html/FLWO/60/TRES/GABORthesis.pdf

Furlan, E., Ciardi, D. R., Everett, M. E., et al. 2017, AJ, 153, 71

Gagné, J., & Faherty, J. K. 2018, ApJ, 862, 138

Gaia Collaboration, Brown, A. G. A., Vallenari, A., et al. 2016, A&A, 595, A2

Gaia Collaboration, Brown, A. G. A., Vallenari, A., et al. 2018, A&A, 616, A1

Gaidos, E., Mann, A. W., Lépine, S., et al. 2014, MNRAS, 443, 2561

Gan, T., Bedell, M., Wang, S. X., et al. 2021, MNRAS, 507, 2220

Gao, P., & Zhang, X. 2020, BAAS, 52, 213.03

Gelman, A., & Rubin, D. B. 1992, StaSc, 7, 457

Giclas, H. L., Burnham, R., & Thomas, N. G. 1971, Lowell Proper Motion Survey Northern Hemisphere (Flagstaff, AZ: Lowell Observatory)

Greene, T. P., Line, M. R., Montero, C., et al. 2015, ApJ, 817, 17

Guerrero, N. M., Seager, S., Huang, C. X., et al. 2021, ApJS, 254, 39

Harris, C. R., Millman, K. J., van der Walt, S. J., et al. 2020, Natur, 585, 357

Henden, A. A., Levine, S., Terrell, D., et al. 2018, in AAS Meeting 232 (Washington, DC: AAS), 223.06

Hobson, M. J., Brahm, R., Jordán, A., et al. 2021, AJ, 161, 235

Hodapp, K. W., Jensen, J. B., Irwin, E. M., et al. 2003, PASP, 115, 1388

Howard, A. W., Marcy, G. W., Bryson, S. T., et al. 2012, ApJS, 201, 15

Howell, S. B., Everett, M. E., Horch, E. P., et al. 2016, ApJ, 829, L2

Howell, S. B., Everett, M. E., Sherry, W., Horch, E., & Ciardi, D. R. 2011, AJ, 142, 19

Hunter, J. D. 2007, CSE, 9, 90

IPAC 2013, NASA Exoplanet Archive, doi:10.26133/NEA1

IPAC 2015, ExoFOP-TESS, doi:10.26134/ExoFOP3

Jenkins, J. M. 2002, ApJ, 575, 493

Jenkins, J. M., Tenenbaum, P., Seader, S., et al. 2020, in Kepler Data Processing Handbook, KSCI-19081-003, ed. J. M. Jenkins (Moffett Field, CA: NASA Ames Research Center)

Jenkins, J. M., Chandrasekaran, H., McCauliff, S. D., et al. 2010, Proc. SPIE, 7740, 77400D

Jenkins, J. M., Twicken, J. D., McCauliff, S., et al. 2016, Proc. SPIE, 9913, 99133E

Kanodia, S., Wolfgang, A., Stefansson, G. K., Ning, B., & Mahadevan, S. 2019, MRExo: Non-parametric Mass-radius Relationship for Exoplanets, Astrophysics Source Code Library, ascl:1912.020

Kanodia, S., & Wright, J. 2018, RNAAS, 2, 4

Kanodia, S., Cañas, C. I., Stefansson, G., et al. 2020, ApJ, 899, 29

Kawaler, S. D. 2015, in ASP Conf. Ser., 493, 19th European Workshop on White Dwarfs, ed. P. Dufour, P. Bergeron, & G. Fontaine (San Francisco, CA: ASP), 65, arXiv:1410.6934

Kempton, E. M.-R., Bean, J. L., Louie, D. R., et al. 2018, PASP, 130, 114401

Kostov, V. B., Mullally, S. E., Quintana, E. V., et al. 2019, AJ, 157, 124

Kreidberg, L., Line, M. R., Bean, J. L., et al. 2015, ApJ, 814, 66

Lam, S. K., Pitrou, A., & Seibert, S. 2015, in Proc. Second Workshop on the LLVM Compiler Infrastructure in HPC, LLVM '15 (New York: Association for Computing Machinery), 6

Lee, E. J., & Chiang, E. 2016, ApJ, 817, 90

Li, J., Tenenbaum, P., Twicken, J. D., et al. 2019, PASP, 131, 024506

Lindegren, L., Hernández, J., Bombrun, A., et al. 2018, A&A, 616, A2

Line, M. R., Knutson, H. A., Wolf, A. S., & Yung, Y. L. 2013, ApJ, 783, 70

Line, M. R., Wolf, A. S., Zhang, X., et al. 2013, ApJ, 775, 137

Lissauer, J. J., Marcy, G. W., Rowe, J. F., et al. 2012, ApJ, 750, 112

Lomb, N. R. 1976, Ap&SS, 39, 447

Luhn, J. K., Wright, J. T., Howard, A. W., & Isaacson, H. 2020, AJ, 159, 235

Luyten, W. J. 1979, NLTT Catalogue, Vol. I (Minneapolis, MN: Univ. Minnesota)

Madhusudhan, N. 2019, ARA&A, 57, 617

Malhotra, R. 2015, ApJ, 808, 71

Mann, A. W., Feiden, G. A., Gaidos, E., Boyajian, T., & von Braun, K. 2015, ApJ, 804, 64

Mann, A. W., Dupuy, T., Kraus, A. L., et al. 2019, ApJ, 871, 63

Marcy, G. W., Isaacson, H., Howard, A. W., et al. 2014, ApJS, 210, 20

Mayor, M., & Queloz, D. 1995, Natur, 378, 355

Meyer, M. R., Amara, A., Reggiani, M., & Quanz, S. P. 2018, A&A, 612, L3

Millholland, S. 2019, ApJ, 886, 72

Monson, A. J., Beaton, R. L., Scowcroft, V., et al. 2017, AJ, 153, 96

Morton, T. D. 2012, ApJ, 761, 6

Narita, N., Fukui, A., Kusakabe, N., et al. 2015, JATIS, 1, 045001

Narita, N., Fukui, A., Kusakabe, N., et al. 2018, JATIS, 5, 1

Newton, E. R., Irwin, J., Charbonneau, D., et al. 2016, ApJ, 821, 93

Nielsen, E. L., De Rosa, R. J., Macintosh, B., et al. 2019, AJ, 158, 13

Nortmann, L., Pallé, E., Salz, M., et al. 2018, Sci, 362, 1388

Nowak, G., Luque, R., Parviainen, H., et al. 2020, A&A, 642, A173

Osborn, A., Armstrong, D. J., Cale, B., et al. 2021, MNRAS, 507, 2782
Parviainen, H. 2015, MNRAS, 450, 3233
Parviainen, H., Palle, E., Zapatero-Osorio, M. R., et al. 2020, A&A, 633, A28
Parviainen, H., Tingley, B., Deeg, H. J., et al. 2019, A&A, 630, A89
Paxton, B., Bildsten, L., Dotter, A., et al. 2011, ApJS, 192, 3
Paxton, B., Cantiello, M., Arras, P., et al. 2013, ApJS, 208, 4
Paxton, B., Marchant, P., Schwab, J., et al. 2015, ApJS, 220, 15
Pecaut, M. J., & Mamajek, E. E. 2013, ApJS, 208, 9
Plavchan, P., Anglada-Escude, G., White, R., et al. 2013a, in AAS/DPS Meeting 45 (Washington, DC: AAS), 204.02
Plavchan, P. P., Anglada-Escude, G., White, R., et al. 2013b, Proc. SPIE, 8864, 88641J
Plavchan, P., Latham, D., Gaudi, S., et al. 2015, arXiv:1503.01770
Quinn, S. N., White, R. J., Latham, D. W., et al. 2014, ApJ, 787, 27
Quirrenbach, A., Amado, P. J., Ribas, I., et al. 2018, Proc. SPIE, 10702, 246
Rajpaul, V., Aigrain, S., Osborne, M. A., Reece, S., & Roberts, S. 2015, MNRAS, 452, 2269
Reinhold, T., & Reiners, A. 2013, A&A, 557, A11
Ricker, G. R., Winn, J. N., Vanderspek, R., et al. 2015, JATIS, 1, 014003
Robitaille, T. P., Tollerud, E. J., Greenfield, P., et al. 2013, A&A, 558, A33
Rodríguez Martínez, R., Gaudi, B. S., Rodriguez, J. E., et al. 2020, AJ, 160, 111
Rogers, L. A. 2015, ApJ, 801, 41
Rogers, L. A., & Seager, S. 2010, ApJ, 712, 974
Rowell, N., Davidson, M., Lindegren, L., et al. 2021, A&A, 649, A11
Santos, N. C., Mayor, M., Naef, D., et al. 2002, A&A, 392, 215
Scargle, J. D. 1982, ApJ, 263, 835
Schlafly, E. F., & Finkbeiner, D. P. 2011, ApJ, 737, 103
Schlieder, J. E., Gonzales, E. J., Ciardi, D. R., et al. 2021, FrASS, 8, 63
Scholz, A., Moore, K., Jayawardhana, R., et al. 2018, ApJ, 859, 153
Scholz, R.-D., Meusinger, H., & Jahreiß, H. 2005, A&A, 442, 211
Schwab, C., Rakich, A., Gong, Q., et al. 2016, Proc. SPIE, 9908, 2220
Scott, N. J., Howell, S. B., Horch, E. P., & Everett, M. E. 2018, PASP, 130, 054502
Seager, S., & Mallen-Ornelas, G. 2003, ApJ, 585, 1038
Seifahrt, A., Stürmer, J., Bean, J. L., & Schwab, C. 2018, Proc. SPIE, 10702, 1930
Sha, L., Huang, C. X., Shporer, A., et al. 2021, AJ, 161, 82
Simonian, G. V. A., Pinsonneault, M. H., & Terndrup, D. M. 2019, ApJ, 871, 174
Sing, D. K., Fortney, J. J., Nikolov, N., et al. 2016, Natur, 529, 59
Skrutskie, M. F., Cutri, R. M., Stiening, R., et al. 2006, AJ, 131, 1163
Smith, J. C., Stumpe, M. C., Van Cleve, J. E., et al. 2012, PASP, 124, 1000
Southworth, J. 2010, MNRAS, 408, 1689
Srinath, S., McGurk, R., Rockosi, C., et al. 2014, Proc. SPIE, 9148, 91482Z
Stassun, K. G., Oelkers, R. J., Paegert, M., et al. 2019, AJ, 158, 138
Stauffer, J., Rebull, L. M., Cody, A. M., et al. 2018, AJ, 156, 275
Stumpe, M. C., Smith, J. C., Catanzarite, J. H., et al. 2014, PASP, 126, 100
Stumpe, M. C., Smith, J. C., Van Cleve, J. E., et al. 2012, PASP, 124, 985
Szentgyorgyi, A. H., Geary, J. G., Latham, D. W., et al. 2005, in AAS Meeting 207 (Washington, DC: AAS), 110.10
Teske, J., Xuesong Wang, S., Wolfgang, A., et al. 2020, ApJS, 256, 33
Tinetti, G., Drossart, P., Eccleston, P., et al. 2016, Proc. SPIE, 9904, 658
Twicken, J. D., Catanzarite, J. H., Clarke, B. D., et al. 2018, PASP, 130, 064502
Vanderburg, A., Huang, C. X., Rodriguez, J. E., et al. 2019, ApJL, 881, L19
Vanderburg, A., Plavchan, P., Johnson, J. A., et al. 2016, MNRAS, 459, 3565
Virtanen, P., Gommers, R., Oliphant, T. E., et al. 2020, NatMe, 17, 261
Wheatley, P. J., West, R. G., Goad, M. R., et al. 2018, MNRAS, 475, 4476
Wood, M. L., Mann, A. W., & Kraus, A. L. 2021, AJ, 162, 128
Wright, E. L., Eisenhardt, P. R. M., Mainzer, A. K., et al. 2010, AJ, 140, 1868
Wright, J. T., & Eastman, J. D. 2014, PASP, 126, 838
Zechmeister, M., Reiners, A., Amado, P. J., et al. 2018, A&A, 609, A12
Zeng, L., Jacobsen, S. B., Sasselov, D. D., et al. 2019, PNAS, 116, 9723
Ziegler, C., Tokovinin, A., Briceño, C., et al. 2019, AJ, 159, 19
Zink, J. K., Hardegree-Ullman, K. K., Christiansen, J. L., et al. 2020, AJ, 159, 154